

# Theoretical and numerical studies of the shallow water equations with a transmission boundary condition

メタデータ	言語: eng 出版者: 公開日: 2020-01-08 キーワード (Ja): キーワード (En): 作成者: メールアドレス: 所属:
URL	<a href="http://hdl.handle.net/2297/00056470">http://hdl.handle.net/2297/00056470</a>

This work is licensed under a Creative Commons Attribution-NonCommercial-ShareAlike 3.0 International License.



Dissertation

*Theoretical and numerical studies of the  
shallow water equations with a  
transmission boundary condition*



Graduate School of  
Natural Science & Technology  
Kanazawa University

Division of Mathematical and Physical Sciences

Student ID No.	: 1624012011
Name	: Murshed Md Masum
Chief Advisor	: Professor Masato Kimura
Date of Submission (Revised version)	: June 28, 2019



I would like to dedicate this thesis to my loving parents . . .



## **Acknowledgements**

I would like to express my deep sense of gratitude and thanks to my supervisor Professor Dr. Masato Kimura and my co-supervisor Associate Professor Dr. Hirofumi Notsu for their continuous guidance in this whole work. I would like to thank you both from my heart because without your help and support this work was impossible for me. I would also like to thank Mr. Kouta Futai for his help in coding LG-Scheme. I would like to thank Professor H. Kanayama for his kind help in this work. This work would not be possible without the support from Japanese government (Monbukagakusho: MEXT) scholarship. I would also like to thank to the committee members of my thesis. A special thanks to my family. I am grateful to my parents for all of the sacrifices that you've made on my behalf. Your prayer for me was what sustained me thus far. I would also like to thank to Sabana Begum my beloved wife. Thank you for supporting me for everything, and especially I can't thank you enough for encouraging me throughout this experience. To my beloved daughter Maria Murshed and sons Shahrier Murshed and Shams Murshed I would like to express my thanks for being such good children. Finally, I thank my Allah(God) for helping me to finish this work.



## Abstract

In this work, the stability of the shallow water equations (SWEs) with a transmission boundary condition is studied theoretically and numerically using a suitable energy. In the theoretical part, using a suitable energy, we begin with deriving an equality which implies an energy estimate of the SWEs with the Dirichlet and the slip boundary conditions.

For the SWEs with a transmission boundary condition, an inequality for the energy estimate is proved under some assumptions to be satisfied in practical computation. In the numerical part, based on the theoretical results, the energy estimate of the SWEs with a transmission boundary condition is confirmed numerically by a finite difference method (FDM) and Lagrange–Galerkin method (LGM). The choice of a positive constant  $c_0$  used in the transmission boundary condition is investigated additionally. Furthermore, we present numerical results by a LGM, which are similar to those by the FDM.

The computation of the SWEs with the transmission boundary condition are also made for the Bay of Bengal by a LGM with the triangular mesh. To see the performance of the LGM we have investigated the experimental order of convergence for the LGM with a suitable choice of exact solutions for five different cases of boundary setting for the norms  $l^\infty - L^2$ ,  $l^\infty - H_0^1$ ,  $l^\infty - H^1$ ,  $l^2 - L^2$ ,  $l^2 - H_0^1$  and  $l^2 - H^1$ . The experimental order of convergence of  $u_1$  and  $u_2$  is  $O(h)$  for all the six norms and experimental order of convergence of  $\eta$  is  $O(h)$  for the norms  $l^\infty - L^2$  and  $l^2 - L^2$  and for the other four norms experimental order of convergence is not  $O(h)$  but confirmed to be convergent.

In order to see whether the transmission boundary condition is independent of its position or not, simulations are made in the Bay of Bengal, setting the transmission boundary condition in two different places. We have computed the mass and  $L^2$ -norm of  $\eta$  and the results shows that the transmission boundary condition works well numerically it is almost independent of its position.

The theoretical results along with the numerical results strongly recommend that the transmission boundary condition is suitable for the boundaries in the open sea.

In this work, we have succeeded to give some theoretical results and this is the first step of mathematical foundation of the SWEs with the transmission boundary condition.

# Table of contents

<b>List of figures</b>	<b>xi</b>
<b>List of tables</b>	<b>xiii</b>
<b>1 General introduction</b>	<b>1</b>
<b>2 Derivation of the model equations</b>	<b>13</b>
2.1 SWEs . . . . .	13
2.2 Surface and bottom boundary conditions . . . . .	15
2.3 Vertically integrated equations . . . . .	15
<b>3 Theoretical results</b>	<b>25</b>
3.1 Statement of the problem . . . . .	25
3.2 Energy estimate . . . . .	27
<b>4 Numerical results by FDM</b>	<b>35</b>
4.1 Problem setting . . . . .	35
4.1.1 A finite difference scheme . . . . .	36
4.1.2 Numerical results for five cases of boundary settings . . . . .	36
4.1.3 Numerical study of energy estimate . . . . .	37
4.1.4 Choice of $c_0$ . . . . .	43

---

<b>5</b>	<b>Numerical results by LGM</b>	<b>45</b>
5.1	LG scheme . . . . .	45
5.1.1	Numerical results for five cases of boundary settings . . . . .	46
5.1.2	Numerical study of energy estimate . . . . .	48
5.1.3	The experimental order of convergence of the LG scheme . . . . .	52
5.2	Numerical results for the Bay of Bengal . . . . .	59
5.2.1	Computation of mass and $L^2$ norm for the Bay of Bengal . . . . .	64
<b>6</b>	<b>Instability on the transmission boundary and some future works</b>	<b>69</b>
6.1	Instability on the transmission boundary . . . . .	69
6.2	Some future works . . . . .	71
<b>7</b>	<b>Conclusion</b>	<b>73</b>
	<b>References</b>	<b>77</b>

# List of figures

1.1	The northern part of Bay of Bengal including the coast of Bangladesh, east coast of India and west coast of Myanmar . . . . .	2
1.2	Simulation of SWEs in the Bay of Bengal . . . . .	3
1.3	The northwest corner of Bay of Bengal, and track of several cyclones . . . . .	5
1.4	A triangular mesh for the Bay of Bengal . . . . .	9
2.1	Shallow water model domain . . . . .	14
4.1	Simulated results in a square domain by FDM . . . . .	38
4.2	Figure showing energy computed using FDM . . . . .	40
4.3	Figure showing derivative of energy computed using FDM . . . . .	41
4.4	Figure showing $I_1, I_2, I_3$ and $I_4$ computed using FDM . . . . .	42
5.1	Simulated results in a square domain by LGM . . . . .	47
5.2	Figure showing energy computed using LGM . . . . .	49
5.3	Figure showing derivative of energy computed using LGM . . . . .	50
5.4	Figure showing $I_1, I_2, I_3$ and $I_4$ computed using LGM . . . . .	51
5.5	Figure representing the experimental order of convergence by $l^\infty (L^2)$ norm . . . . .	53
5.6	Figure representing the experimental order of convergence by $l^\infty (H_0^1)$ norm . . . . .	54
5.7	Figure representing the experimental order of convergence by $l^\infty (H^1)$ norm . . . . .	55
5.8	Figure representing the experimental order of convergence by $l^2 (L^2)$ norm . . . . .	56

5.9	Figure representing the experimental order of convergence by $l^2 (H_0^1)$ norm	57
5.10	Figure representing the experimental order of convergence by $l^2 (H^1)$ norm	58
5.11	A figure of Bay of Bengal domain showing the boundary setting . . . . .	59
5.12	A figure of Bay of Bengal domain (extended) showing the boundary setting	60
5.13	Simulation in the Bay of Bengal at time $t = 0s, 2800s$ and $3120s$ . . . . .	62
5.14	Simulation in the Bay of Bengal at time $t = 3240s, 3740s, 3940s$ and $4660s$ .	63
5.15	Figure showing mass of $\eta$ . . . . .	64
5.16	Graph of $\eta$ on transmission boundary at time $t = 0s, 2800s$ and $3120s$ . . .	66
5.17	Graph of $\eta$ on transmission boundary at time $t = 3240s, 3740s, 3940s$ and 4660s . . . . .	67
5.18	Figure showing $L^2$ norm of $\eta$ . . . . .	68
6.1	Graph of $\eta$ on transmission boundary at time $t = 6500s$ . . . . .	70
6.2	$L^2$ norm of $\eta$ for the two cases of transmission boundary setting . . . . .	70

# List of tables

1.1	Table showing the number of deaths associated with several deadly disasters occurred in the Bay of Bengal region . . . . .	6
4.1	Table showing maximum and minimum values of $I_1, I_2, I_3$ and $I_4$ computed using FDM . . . . .	39
4.2	Table showing the values of $c_0$ and $\mathcal{S}_h(c_0)$ . . . . .	44



# Chapter 1

## General introduction

Most of the natural phenomena are expressed by partial differential equations or a system of partial differential equations. The Navier-Stokes equations are a system of partial differential equations which expresses a lot of real world phenomena related to fluid flow problems. According to [24], the equations (Navier-Stokes equations) cannot be solved analytically in most cases due to complicated geometries, initial conditions, boundary conditions or source terms. For this reason, numerical methods are applied, which can be very time consuming. But under the assumption of a hydro-static pressure distribution one space dimension of the Navier-Stokes equations can be eliminated without much loss of accuracy. This can be done if the fluid is at rest, but in many cases it is sufficient that the horizontal scales are much larger than the vertical scales. The resulting system of partial differential equations is called shallow water equations (SWEs). The reduction of one space dimension reduces the computational cost of numerical solutions greatly. It is pertinent to mention here that the SWEs were first formulated by the mathematician Adhémar Jean Claude Barré de Saint-Venant for one-dimensional unsteady open channel flows (see [46] ), and the 1D equations are therefore also known as the Saint-Venant system. After that a lot of developments of the SWEs are done by many researchers for various purpose. The derivation of one-layer viscous SWEs can be found in [21] and two-layers SWEs are derived in [20] for Tsunami simulation purpose. It is of interest to note here that the SWEs are used for the simulation

of Tsunami/storm surge in the bay, e.g., [7, 9–18, 20, 29–33, 35–37, 40–44, 47, 49, 50]. In such simulation there are some boundaries in the open sea (see Figure 1.1). In a real situation, if wave propagates towards such boundaries in the open sea, then there should not be any reflection on these boundaries. Therefore, in the simulation a special type of boundary condition should be imposed on these boundaries which has capability of removing the artificial reflection. In this study, following [20] a transmission boundary condition has been used on the boundaries in the open sea which is capable to remove these kinds of artificial reflection and on the closed boundaries (boundaries in the coast) zero Dirichlet boundary condition is used. Figure 1.2 gives an idea of wave propagation in the Bay of Bengal with the transmission and Dirichlet boundaries.



Fig. 1.1 The northern part of Bay of Bengal including the coast of Bangladesh, east coast of India and west coast of Myanmar.

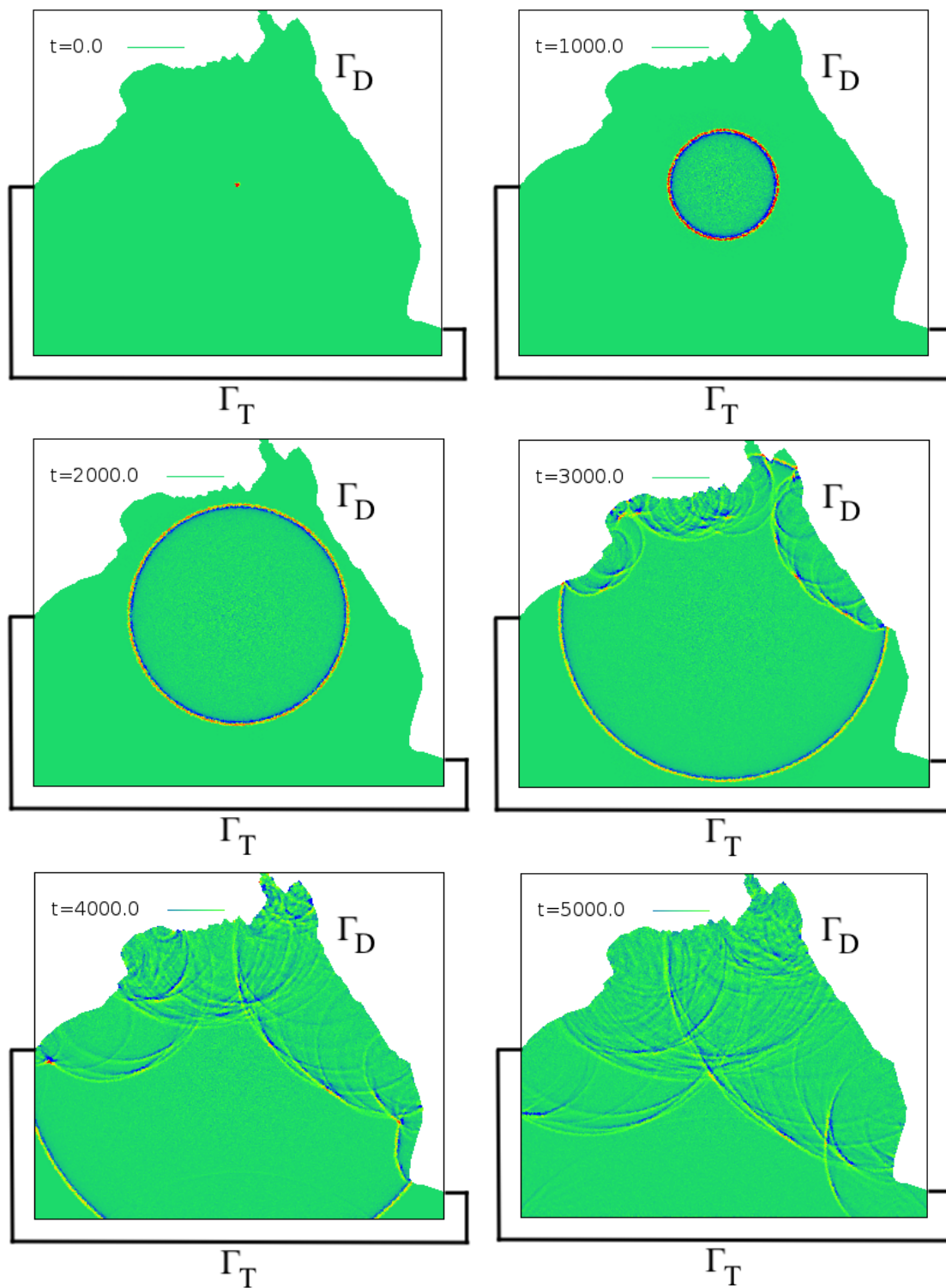


Fig. 1.2 Simulation of SWEs in the Bay of Bengal with transmission and Dirichlet boundary conditions, here  $\Gamma_T$  and  $\Gamma_D$  represent the transmission and the Dirichlet boundaries, respectively

It is of interest to note here that our final goal is to develop a storm surge prediction model for the Bay of Bengal region (see Figure 1.1). The reason of choosing this problem is discussed below.

The coast of Bangladesh is affected by various environmental hazards. Storm surge is one of them, which causes a tremendous loss of lives and properties every year. Table 1.1 lists the number of deaths associated with several deadly disasters occurred in the Bay of Bengal region. The track of different storm surges are presented in Fig. 1.3 for making understand of frequent visiting. As in [34], every year on an average 5–6 storms form in this region, which causes 80% of global casualties. The coastal region of Bangladesh is the most vulnerable because of the shallowness of the coastal water, high density of population in low-lying islands, high bending of the boundaries of the coasts and islands, discharge from river, high range of astronomical tide and favorable track of cyclones (see [8]). In addition, the rates of erosion and accretion are very high in this region. The discharge of sediment is the highest and the discharge of freshwater is the third highest from the river Meghna among all river systems in the world (see [26]). Bangladesh, is situated at the northern tip of the Bay of Bengal between  $20^{\circ}\text{N}$  to  $26^{\circ}\text{N}$  Latitudes and  $88^{\circ}\text{E}$  to  $92^{\circ}\text{E}$  Longitudes. It is bordered on the west, north and east by India, on the south-east by Myanmar, on the south by the Bay of Bengal. A proper warning system for the region can mitigate the sufferings of its people and live stocks resulting from these storm surges. Though, Bangladesh Meteorological Department (BMD) has a warning system which was bought from IIT, by which they can predict the information of landfall time, sea level rising in a certain accuracy as well as they can predict the storm track but not unique with actuality. Thus an effective storm surge prediction model is highly desirable for the coastal region of Bangladesh which can minimize the resulting damage from storm surges.

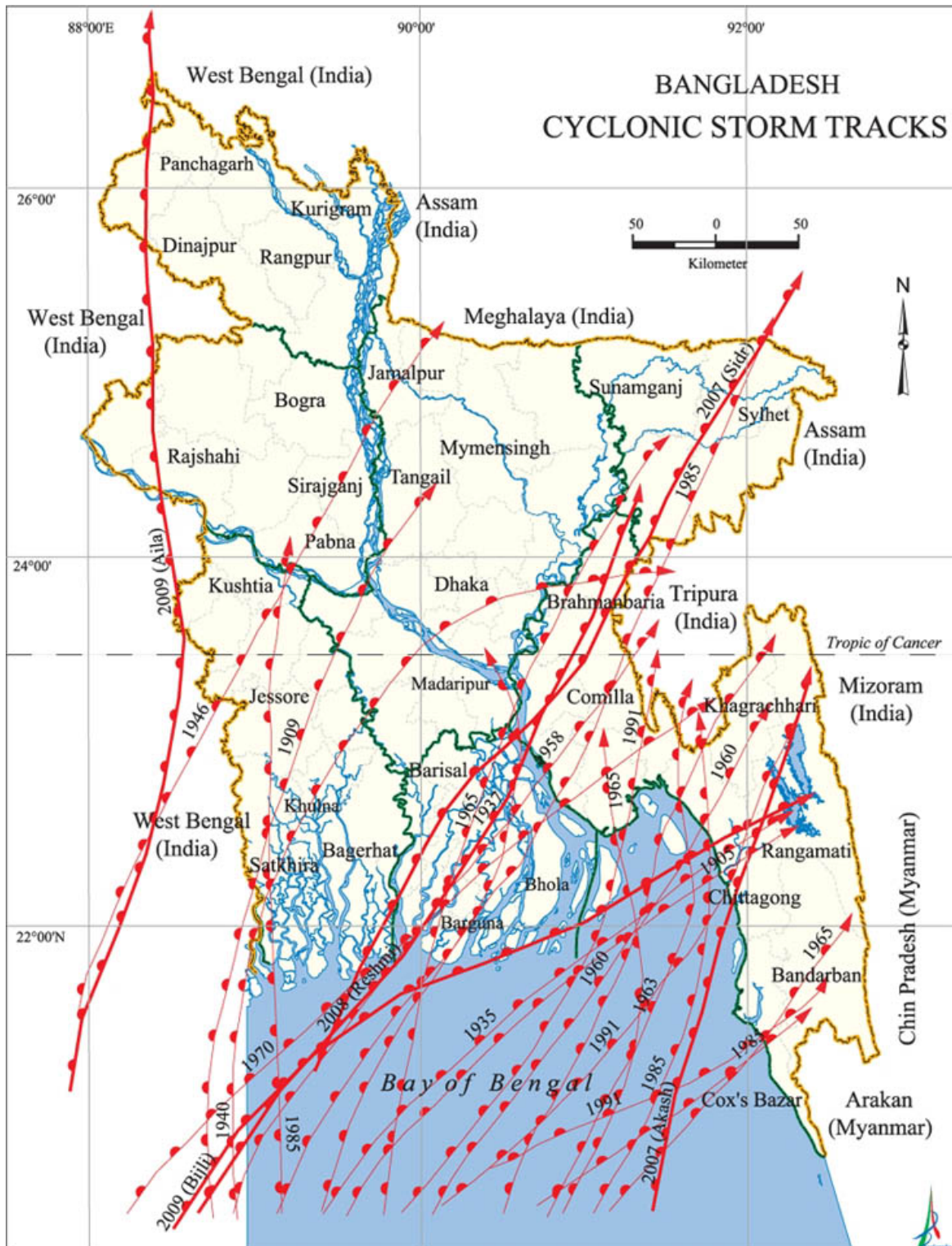


Fig. 1.3 The northwest corner of Bay of Bengal, and track of several cyclones (source: <http://en.banglapedia.org/index.php?title=Cyclone>).

Table 1.1 Storm surge locations and losses of life (data sources: [6, 8] and NASA website).

Year	Location	Death
1970	Bangladesh	500,000
1737	India	300,000
1897	Bangladesh	175,000
1991	Bangladesh	140,000
1876	Bangladesh	100,000
1864	India	50,000
1833	India	50,000
1822	Bangladesh	40,000
1839	India	20,000
1789	India	20,000
1965	Bangladesh	19,279
1963	Bangladesh	11,520
1961	Bangladesh	11,468
1977	India	10,000
1960	Bangladesh	5,149
2007	Bangladesh	3,376
2009	India	275
2016	Bangladesh	24
2017	Bangladesh	18

Many analyses have been made in prediction of water level during storm surges as well as in development of warning system on the basis of operational forecasting model all over the world, among them worth mentioning studies are [10–15, 47, 50].

A limited number of studies have been done over the Bay of Bengal region considering the west coast of India along with the coast of Bangladesh. Among them some worth mentioning studies are [7, 9, 16–18, 29–33, 35–37, 40–44, 49].

Almost all of the of the studies mentioned here have been conducted using radiation type boundary condition for the boundaries in the open sea, which is very similar to the transmission boundary condition (1.2). Also these studies are about the development of numerical computation without ensuring the stability of the model with this kind of boundaries mathematically. It is of interest to note here that for linearized SWEs, the existence and uniqueness of solutions are studied in [22] and the convergence of a finite element scheme

for that linearized SWEs is studied in [23]. As far as we know, there is no theoretical results for the existence, uniqueness or regularity for the SWEs with the transmission boundary condition. It is to be noted here that the energy estimate of the SWEs have been studied theoretically in [21] considering  $u \cdot n = 0$ . However, as far as we know, there is no theoretical results on the energy estimate of the SWEs with the transmission boundary condition. In this study, we have intended to investigate the stability of the SWEs with the transmission boundary condition both theoretically and numerically through suitable energy estimates.

The SWEs can be considered as a coupled system of a pure convection equation for the function  $\phi$  of total wave height and a simplified Navier–Stokes equation for the velocity  $u = (u_1, u_2)^T$  obtained by averaging function values in  $x_3$ -direction. Let  $\Omega \subset \mathbb{R}^2$  be a bounded domain and  $T$  a positive constant. We consider the problem : find  $(\phi, u) : \overline{\Omega} \times [0, T] \rightarrow \mathbb{R} \times \mathbb{R}^2$  such that

$$\begin{cases} \frac{\partial \phi}{\partial t} + \nabla \cdot (\phi u) = 0 & \text{in } \Omega \times (0, T), \\ \rho \phi \left[ \frac{\partial u}{\partial t} + (u \cdot \nabla) u \right] - 2\mu \nabla \cdot (\phi D(u)) + \rho g \phi \nabla \eta = 0 & \text{in } \Omega \times (0, T), \\ \phi = \eta + \zeta & \text{in } \Omega \times (0, T), \end{cases} \quad (1.1)$$

The explanation about  $u$ ,  $\phi$ ,  $\eta$  and  $\zeta$  can be found in Chapter 3 and in the Figure 2.1. It is known that a boundary data for  $\phi$  is necessary on the so-called inflow boundary, where  $u \cdot n < 0$  is satisfied for the outward unit normal vector  $n$ . We can easily know whether the Dirichlet data for  $\phi$  is required or not on the Dirichlet and the slip boundaries for  $u$ , since the sign of  $u \cdot n$  is known a priori. On the transmission boundary  $\Gamma_T$ , however, the boundary condition for  $u$  and  $\phi$  is mysterious and problematic from both computational and mathematical view points. The transmission boundary condition of the form

$$u = c \frac{\eta}{\phi} n \quad \text{on } \Gamma_T \times (0, T), \quad (1.2)$$

is often used on  $\Gamma_T$ , where  $c(x)$  is a given positive function and  $\eta(x, t) = \phi(x, t) - \zeta(x)$  is the elevation from the reference height for a given depth function  $\zeta$ . It is of interest to note here that including wind stress, bottom friction and Coriolis force in (1.1) a storm surge prediction model can be developed (see (2.11) and (2.12) in Chapter 2). For the theoretical study we set each of them as zero to make the problem simple.

Let  $\phi_h^k$  and  $u_h^k$  be the approximations of  $\phi^k: = \phi(\cdot, t^k)$  and  $u^k: = u(\cdot, t^k)$ , respectively, where  $t^k: = k\Delta t$  ( $k \in \mathbb{Z}$ ) for a time increment  $\Delta t$ . In our computation we get  $\phi_h^{k+1}$  by using  $u_h^k$ , and then  $u_h^{k+1}$  by using the condition (1.2) as the Dirichlet boundary condition for  $u$ . But at the same time we should consider (1.2) as the boundary data for  $\phi_h^{k+1}$  if the position is on inflow boundary, i.e.,  $u_h^{k+1} \cdot n < 0$ . In fact, if  $u_h^{k+1} \cdot n < 0$ , we need to give the value of  $\phi_h^{k+1}$  which is unknown.

It is known that the finite difference method (FDM) is suitable for a domain of rectangular or square shape, but the real domain is not usually of rectangular or a square shape. It is also known that the finite element method (FEM) is more appropriate for a domain of irregular shape. It is to be noted here that both rectangular and triangular mesh are used for FEM but triangular mesh is more suitable for a domain of complex shape. Considering this fact into account the computation of the SWEs with the transmission boundary condition are also made by a Lagrange–Galerkin method (LGM) with the triangular mesh (see Figure 1.4). The LGM is a FEM based on the time discretization of the material derivative,

$$\frac{\phi^{k+1}(x) - \phi^k(x - u^k(x)\Delta t)}{\Delta t}.$$

The LGM is a powerful numerical method for the Navier-Stokes equations in fluid flow problems. The study of LGM for the Navier-Stokes equations can be found in , e.g., [1–4, 27, 28, 38, 39, 48]. In this study we have used LGM for SWEs.

It is to be noted here that the position  $x - u^k(x)\Delta t$  is the so-called upwind point of  $x$  with respect to  $u^k$ . In the computation the “nearest” boundary value of  $\phi^k$  is used if the upwind

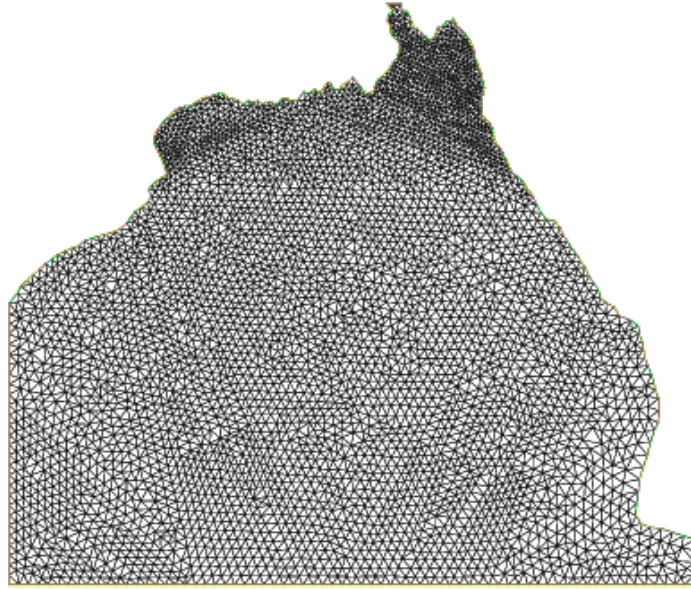


Fig. 1.4 A triangular mesh for the Bay of Bengal

point places outside the domain, and the LGM works without boundary data for  $\phi^{k+1}$  even if  $u^{k+1} \cdot n < 0$ . In the LG method the problem on the transmission boundary seems to be solved numerically, but it is still problematic mathematically.

In this work, in order to understand the transmission boundary condition mathematically, we study the stability of the SWEs in terms of a suitable energy, and confirm the stability numerically by both FDM and LGM. It is to be noted here that we can show a (successful) energy estimate of the SWEs, when only the Dirichlet and the slip boundary conditions are employed, cf. Corollary 3.2.3-(ii), where such discussions have been done under the periodic boundary condition, e.g., [5, 25].

The stability is considered theoretically with respect to the energy as follows. Introducing a suitable energy, we begin with deriving an equality that the time-derivative of the energy consists of four terms, where three terms are line integrals over the boundary and the other term is an integral over the whole domain which is always non-positive, cf. Theorem 3.2.1. Since the three line integrals vanish over the Dirichlet and the slip boundaries, as a result, we have the three line integrals over the transmission boundary and the integral over the domain,

cf. Corollary 3.2.3-(i). An energy estimate is obviously obtained if there is no transmission boundary, cf. Corollary 3.2.3-(ii). In addition, we obtain that a sum of two line integrals over the transmission boundary is non-positive under some conditions to be satisfied in real computations, cf. Theorem 3.2.4. Although, at present, the mathematical results do not derive the stability estimate of the SWEs with the transmission boundary condition directly, we have good information and can study the stability numerically by using the theoretical results.

Though our final goal is to develop a storm surge prediction model for the Bay of Bengal region, until now we are not succeeded, but we have some good results, which we believe can help to develop an appropriate storm surge prediction model for that region. We have a theoretical (successful) energy estimate of the SWEs, with the Dirichlet and the slip boundary conditions and a numerical (successful) energy estimate of the SWEs, with the Dirichlet and the transmission boundary conditions by both FDM and LGM. To see the performance of the LGM we have investigated the experimental order of convergence for the LGM with a suitable choice of exact solutions for five different boundary setting (see Section 4.1) for the norms  $l^\infty - L^2$ ,  $l^\infty - H_0^1$ ,  $l^\infty - H^1$ ,  $l^2 - L^2$ ,  $l^2 - H_0^1$  and  $l^2 - H^1$ . The experimental order of convergence of  $u_1$  and  $u_2$  is  $O(h)$  for all the six norms and experimental order of convergence of  $\eta$  is  $O(h)$  for the norms  $l^\infty - L^2$  and  $l^2 - L^2$  and for the other four norms experimental order of convergence is not  $O(h)$  but confirmed to be convergent. In order to see whether the transmission boundary condition is independent of its position or not, simulations are made in the Bay of Bengal, setting the transmission boundary condition in two different places. We have computed the mass and  $L^2$ -norm of  $\eta$  and the results shows that the transmission boundary condition is almost independent of its position.

As far as we know, there is not a single model using LGM, for the prediction of storm surge in the Bay of Bengal, therefore we strongly believe that our results will be helpful to

develop an appropriate storm surge prediction model using LGM for the Bay of Bengal in the near future.

The rest of the thesis is organized as follows:

Derivation of the model equations is presented in Chapter 2. Theoretical study of the energy estimates is presented in Chapter 3. Numerical results obtained by FDM is presented in chapter 4. Numerical results obtained by LGM is presented in chapter 5. In Chapter 6, Instability on the transmission boundary and some future works are given. In Chapter 7, conclusion is given. Finally, the total bibliography that has been needed for completing this thesis is presented.



# Chapter 2

## Derivation of the model equations

In this Chapter we have derived our model equations following [19] by considering one-layer viscous SWEs.

### 2.1 SWEs

For any atmospheric or oceanic phenomenon, if the horizontal length scale is much larger than the vertical scale, then the  $x_3$  component of the momentum equation may be approximated by the hydro-static equation. The water depth is considered very smaller than the horizontal length scale and there is the shallow-water low-frequency flow. First, we will derive the viscous SWEs. we consider orthogonal coordinates [m], where the directions in the horizontal plane are represented by  $x_1$  and  $x_2$ , respectively, and the vertical direction is represented by  $x_3$  ( see Fig. 2.1). Here  $t$  represents time [s]. We have formulated the system using the Navier-Stokes equations assuming hydro-static pressure and gravity in the  $x_3$  direction, and Coriolis forces occurring in the  $x_1$  and  $x_2$  directions.

$$\sum_{j=1}^3 \frac{\partial}{\partial x_j} u_j = 0, \quad (2.1)$$

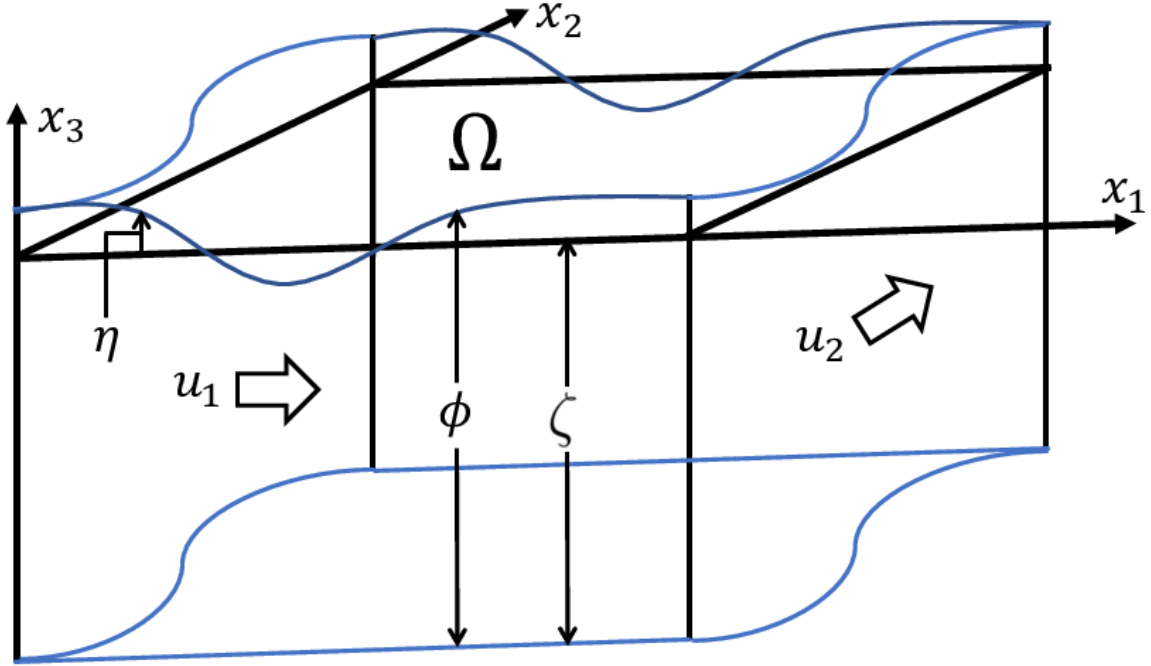


Fig. 2.1 Shallow water model domain

$$\frac{\partial u_1}{\partial t} + \sum_{j=1}^3 u_j \frac{\partial}{\partial x_j} u_1 = -\frac{1}{\rho} \frac{\partial p}{\partial x_1} + \frac{1}{\rho} \sum_{j=1}^3 \frac{\partial}{\partial x_j} \tau_{1j} + f u_2, \quad (2.2)$$

$$\frac{\partial u_2}{\partial t} + \sum_{j=1}^3 u_j \frac{\partial}{\partial x_j} u_2 = -\frac{1}{\rho} \frac{\partial p}{\partial x_2} + \frac{1}{\rho} \sum_{j=1}^3 \frac{\partial}{\partial x_j} \tau_{2j} - f u_1, \quad (2.3)$$

$$0 = -\rho g - \frac{\partial p}{\partial x_3}. \quad (2.4)$$

In the  $x_i$  ( $i = 1, 2, 3$ ) direction velocity [ $m/s$ ] is represented by  $u_i(x_1, x_2, x_3, t)$ , pressure [ $N/m^2$ ] is denoted by  $p(x_1, x_2, x_3, t)$ , density [ $kg/m^3$ ] is denoted by  $\rho$ , stress [ $N/m^2$ ] in the direction  $x_i$  acting on the  $x_j$  plane is denoted by  $\tau_{ij}(x_1, x_2, x_3, t)$ , the Coriolis coefficient [ $1/s$ ] is denoted by  $f$  and the acceleration [ $m/s^2$ ] due to gravity is denoted by  $g$ . In addition, the free surface elevation is denoted by  $\eta(x_1, x_2, t)$ , and  $-\zeta(x_1, x_2)$  represents the ordinate the bottom boundary surface of the water.

## 2.2 Surface and bottom boundary conditions

There is no velocity component in the normal direction on the water's free surface plane, and water bottom plane, and so the following conditions are used for  $u_3$ .

$$\begin{cases} u_3 = \frac{\partial \eta}{\partial t} + \sum_{j=1}^2 u_j \frac{\partial \eta}{\partial x_j}, & (x_3 = \eta(x_1, x_2, t)) \\ u_3 = - \sum_{j=1}^2 u_j \frac{\partial \zeta}{\partial x_j}, & (x_3 = -\zeta(x_1, x_2)). \end{cases} \quad (2.5)$$

## 2.3 Vertically integrated equations

We integrate each of the equations (2.1), (2.2) and (2.3) with respect to  $x_3$ , from the ocean floor  $-\zeta(x_1, x_2)$  to the water surface  $\eta(x_1, x_2, t)$ . Then, the viscous shallow water equations are derived that express averaged rates for the fluid layer. Thus, the velocity component in the  $x_i$  ( $i = 1, 2$ ) direction averaged over the fluid layer is taken as  $U_i(x_1, x_2, t)$ . The thickness of the fluid layer is denoted by  $\phi(x_1, x_2, t)$ . We consider fluids with the constant density represented by  $\rho$ .  $\phi$  and  $U_i$  are represented by the following equations;

$$\phi(x_1, x_2, t) = \eta(x_1, x_2, t) + \zeta(x_1, x_2),$$

$$U_i(x_1, x_2, t) = \frac{1}{\phi} \int_{x_3=-\zeta(x_1, x_2)}^{x_3=\eta(x_1, x_2, t)} u_i dx_3.$$

The integration of (2.1) from  $\zeta(x_1, x_2)$  to  $\eta(x_1, x_2, t)$  in the  $x_3$  direction yields

$$\begin{aligned} 0 &= \sum_{j=1}^3 \int_{x_3=-\zeta(x_1, x_2)}^{x_3=\eta(x_1, x_2, t)} \frac{\partial}{\partial x_j} u_j dx_3 \\ &= \sum_{j=1}^2 \int_{x_3=-\zeta(x_1, x_2)}^{x_3=\eta(x_1, x_2, t)} \frac{\partial}{\partial x_j} u_j dx_3 + \int_{x_3=-\zeta(x_1, x_2)}^{x_3=\eta(x_1, x_2, t)} \frac{\partial}{\partial x_3} u_3 dx_3 \end{aligned}$$

$$\begin{aligned}
&= \sum_{j=1}^2 \frac{\partial}{\partial x_j} \int_{x_3=-\zeta(x_1, x_2)}^{x_3=\eta(x_1, x_2, t)} u_j dx_3 - \sum_{j=1}^2 u_j(x_1, x_2, x_3, t)|_{x_3=\eta(x_1, x_2, t)} \frac{\partial}{\partial x_j} \eta(x_1, x_2, t) \\
&\quad + \sum_{j=1}^2 u_j(x_1, x_2, x_3, t)|_{x_3=-\zeta(x_1, x_2)} \frac{\partial}{\partial x_j} - \zeta(x_1, x_2) + u_3(x_1, x_2, x_3, t)|_{x_3=\eta(x_1, x_2, t)} \\
&\quad - u_3(x_1, x_2, x_3, t)|_{x_3=-\zeta(x_1, x_2)} \\
&= \sum_{j=1}^2 \frac{\partial}{\partial x_j} \int_{x_3=-\zeta(x_1, x_2)}^{x_3=\eta(x_1, x_2, t)} u_j dx_3 - \sum_{j=1}^2 u_j(x_1, x_2, x_3, t)|_{x_3=\eta(x_1, x_2, t)} \frac{\partial}{\partial x_j} \eta(x_1, x_2, t) \\
&\quad + \sum_{j=1}^2 u_j(x_1, x_2, x_3, t)|_{x_3=-\zeta(x_1, x_2)} \frac{\partial}{\partial x_j} \{-\zeta(x_1, x_2)\} + \frac{\partial}{\partial t} \eta(x_1, x_2, t) \\
&\quad + \sum_{j=1}^2 u_j(x_1, x_2, x_3, t)|_{x_3=\eta(x_1, x_2, t)} \frac{\partial}{\partial x_j} \eta(x_1, x_2, t) \\
&\quad - \sum_{j=1}^2 u_j(x_1, x_2, x_3, t)|_{x_3=-\zeta(x_1, x_2)} \frac{\partial}{\partial x_j} \{-\zeta(x_1, x_2)\} \\
&= \frac{\partial}{\partial t} \eta(x_1, x_2, t) + \sum_{j=1}^2 \frac{\partial}{\partial x_j} \{\phi U_j(x_1, x_2, t)\}
\end{aligned}$$

Thus we have

$$\frac{\partial}{\partial t} \eta(x_1, x_2, t) + \sum_{j=1}^2 \frac{\partial}{\partial x_j} \{\phi U_j(x_1, x_2, t)\} = 0 \quad (2.6)$$

Now, we integrate (2.4) in the  $x_3$  direction.

$$p(x_1, x_2, x_3, t) = p_a(x_1, x_2, t) + \rho g \{\eta(x_1, x_2, t) - x_3\}, \quad (2.7)$$

where  $p_a(x_1, x_2, t)$  is the atmospheric pressure.

The integration of (2.2) from  $-\zeta(x_1, x_2)$  to  $\eta(x_1, x_2, t)$  in the  $x_3$  direction yields

$$\begin{aligned}
& \int_{x_3=-\zeta(x_1,x_2)}^{x_3=\eta(x_1,x_2,t)} \frac{\partial u_1}{\partial t} dx_3 + \sum_{j=1}^3 \int_{x_3=-\zeta(x_1,x_2)}^{x_3=\eta(x_1,x_2,t)} u_j \frac{\partial}{\partial x_j} u_1 dx_3 \\
&= -\frac{1}{\rho} \int_{x_3=-\zeta(x_1,x_2)}^{x_3=\eta(x_1,x_2,t)} \frac{\partial p}{\partial x_1} dx_3 + \frac{1}{\rho} \sum_{j=1}^3 \int_{x_3=-\zeta(x_1,x_2)}^{x_3=\eta(x_1,x_2,t)} \frac{\partial}{\partial x_j} \tau_{1j} dx_3 + \int_{x_3=-\zeta(x_1,x_2)}^{x_3=\eta(x_1,x_2,t)} f u_2 dx_3,
\end{aligned}$$

The left hand side can be written as

$$\begin{aligned}
& \int_{x_3=-\zeta(x_1,x_2)}^{x_3=\eta(x_1,x_2,t)} \frac{\partial u_1}{\partial t} dx_3 + \sum_{j=1}^3 \int_{x_3=-\zeta(x_1,x_2)}^{x_3=\eta(x_1,x_2,t)} \left( u_j \frac{\partial}{\partial x_j} u_1 + u_1 \frac{\partial}{\partial x_j} u_j - u_1 \frac{\partial}{\partial x_j} u_j \right) dx_3 \\
&= \int_{x_3=-\zeta(x_1,x_2)}^{x_3=\eta(x_1,x_2,t)} \frac{\partial u_1}{\partial t} dx_3 + \sum_{j=1}^3 \int_{x_3=-\zeta(x_1,x_2)}^{x_3=\eta(x_1,x_2,t)} \frac{\partial}{\partial x_j} (u_1 u_j) dx_3 - \int_{x_3=-\zeta(x_1,x_2)}^{x_3=\eta(x_1,x_2,t)} u_1 \left( \sum_{j=1}^3 \frac{\partial}{\partial x_j} u_j \right) dx_3 \\
&= \frac{\partial}{\partial t} \int_{x_3=-\zeta(x_1,x_2)}^{x_3=\eta(x_1,x_2,t)} u_1 dx_3 - u_1(x_1, x_2, x_3, t) \Big|_{x_3=\eta(x_1,x_2,t)} \frac{\partial}{\partial t} \eta(x_1, x_2, t) \\
&\quad + u_1(x_1, x_2, x_3, t) \Big|_{x_3=-\zeta(x_1,x_2)} \frac{\partial}{\partial t} \{-\zeta(x_1, x_2)\} + \sum_{j=1}^2 \int_{x_3=-\zeta(x_1,x_2)}^{x_3=\eta(x_1,x_2,t)} \frac{\partial}{\partial x_j} (u_1 u_j) dx_3 \\
&\quad + \int_{x_3=-\zeta(x_1,x_2)}^{x_3=\eta(x_1,x_2,t)} \frac{\partial}{\partial x_3} (u_1 u_3) dx_3 \\
&= \frac{\partial}{\partial t} (\phi U_1) - u_1(x_1, x_2, x_3, t) \Big|_{x_3=\eta(x_1,x_2,t)} \frac{\partial}{\partial t} \eta(x_1, x_2, t) \\
&\quad + \sum_{j=1}^2 \frac{\partial}{\partial x_j} \int_{x_3=-\zeta(x_1,x_2)}^{x_3=\eta(x_1,x_2,t)} (u_1 u_j) dx_3 - \sum_{j=1}^2 (u_1 u_j) \Big|_{x_3=\eta(x_1,x_2,t)} \frac{\partial}{\partial x_j} \eta(x_1, x_2, t) \\
&\quad + \sum_{j=1}^2 (u_1 u_j) \Big|_{x_3=-\zeta(x_1,x_2)} \frac{\partial}{\partial x_j} - \zeta(x_1, x_2) + (u_1 u_3) \Big|_{x_3=\eta(x_1,x_2,t)} - (u_1 u_3) \Big|_{x_3=-\zeta(x_1,x_2)} \\
&= \frac{\partial}{\partial t} (\phi U_1) + \sum_{j=1}^2 \frac{\partial}{\partial x_j} \int_{x_3=-\zeta(x_1,x_2)}^{x_3=\eta(x_1,x_2,t)} (u_1 u_j) dx_3 \\
&\quad + u_1(x_1, x_2, x_3, t) \Big|_{x_3=\eta(x_1,x_2,t)} \left\{ \frac{\partial \eta}{\partial t} + \sum_{j=1}^2 (u_j) \Big|_{x_3=\eta(x_1,x_2,t)} \frac{\partial \eta}{\partial x_j} - (u_3) \Big|_{x_3=\eta(x_1,x_2,t)} \right\}
\end{aligned}$$

$$\begin{aligned}
& +u_1(x_1, x_2, x_3, t)|_{x_3=-\zeta(x_1, x_2)} \left\{ \sum_{j=1}^2 (u_j)|_{x_3=-\zeta(x_1, x_2)} \frac{\partial b}{\partial x_j} - (u_3)|_{x_3=-\zeta(x_1, x_2)} \right\} \\
& = \frac{\partial}{\partial t}(\phi U_1) + \sum_{j=1}^2 \frac{\partial}{\partial x_j} \int_{x_3=-\zeta(x_1, x_2)}^{x_3=\eta(x_1, x_2, t)} (u_1 u_j) dx_3 \\
& = \frac{\partial}{\partial t}(\phi U_1) + \frac{\partial}{\partial x_1} \int_{x_3=-\zeta(x_1, x_2)}^{x_3=\eta(x_1, x_2, t)} (u_1)^2 dx_3 + \frac{\partial}{\partial x_2} \int_{x_3=-\zeta(x_1, x_2)}^{x_3=\eta(x_1, x_2, t)} (u_1 u_2) dx_3 \\
& = \frac{\partial}{\partial t}(\phi U_1) + \frac{\partial}{\partial x_1} \int_{x_3=-\zeta(x_1, x_2)}^{x_3=\eta(x_1, x_2, t)} \{(u_1)^2 - 2u_1 U_1 + (U_1)^2\} dx_3 \\
& \quad + \frac{\partial}{\partial x_2} \int_{x_3=-\zeta(x_1, x_2)}^{x_3=\eta(x_1, x_2, t)} (u_1 u_2 - u_1 U_2 - U_1 u_2 + U_1 U_2) dx_3 \\
& \quad + \frac{\partial}{\partial x_1} \int_{x_3=-\zeta(x_1, x_2)}^{x_3=\eta(x_1, x_2, t)} \{2u_1 U_1 - (U_1)^2\} dx_3 + \frac{\partial}{\partial x_2} \int_{x_3=-\zeta(x_1, x_2)}^{x_3=\eta(x_1, x_2, t)} (u_1 U_2 + U_1 u_2 - U_1 U_2) dx_3 \\
& = \frac{\partial}{\partial t}(\phi U_1) + \frac{\partial}{\partial x_1} \int_{x_3=-\zeta(x_1, x_2)}^{x_3=\eta(x_1, x_2, t)} (u_1 - U_1)^2 dx_3 \\
& \quad + \frac{\partial}{\partial x_2} \int_{x_3=-\zeta(x_1, x_2)}^{x_3=\eta(x_1, x_2, t)} (u_1 - U_1)(u_2 - U_2) dx_3 \\
& \quad + \frac{\partial}{\partial x_1} \{\phi(U_1)^2\} + \frac{\partial}{\partial x_2} (\phi U_1 U_2) \\
& = \frac{\partial}{\partial t}(\phi U_1) + \frac{\partial}{\partial x_1} \{\phi(U_1)^2\} + \frac{\partial}{\partial x_2} (\phi U_1 U_2) \\
& \quad + \frac{\partial}{\partial x_1} \int_{x_3=-\zeta(x_1, x_2)}^{x_3=\eta(x_1, x_2, t)} (\tilde{u}_1)^2 dx_3 + \frac{\partial}{\partial x_2} \int_{x_3=-\zeta(x_1, x_2)}^{x_3=\eta(x_1, x_2, t)} \tilde{u}_1 \tilde{u}_2 dx_3,
\end{aligned}$$

where  $\tilde{u}_i = u_i - U_i$ . Now sending  $\frac{\partial}{\partial x_1} \int_{x_3=-\zeta(x_1, x_2)}^{x_3=\eta(x_1, x_2, t)} (\tilde{u}_1)^2 dx_3 + \frac{\partial}{\partial x_2} \int_{x_3=-\zeta(x_1, x_2)}^{x_3=\eta(x_1, x_2, t)} \tilde{u}_1 \tilde{u}_2 dx_3$  on the right hand side, we have

$$\begin{aligned}
& \frac{\partial}{\partial t}(\phi U_1) + \frac{\partial}{\partial x_1} \{ \phi (U_1)^2 \} + \frac{\partial}{\partial x_2} (\phi U_1 U_2) \\
&= -\frac{1}{\rho} \int_{x_3=-\zeta(x_1, x_2)}^{x_3=\eta(x_1, x_2, t)} \frac{\partial p}{\partial x_1} dx_3 + \frac{1}{\rho} \sum_{j=1}^3 \int_{x_3=-\zeta(x_1, x_2)}^{x_3=\eta(x_1, x_2, t)} \frac{\partial}{\partial x_j} \tau_{1j} dx_3 \\
& \quad + \int_{x_3=-\zeta(x_1, x_2)}^{x_3=\eta(x_1, x_2, t)} f u_2 dx_3 - \frac{\partial}{\partial x_1} \int_{x_3=-\zeta(x_1, x_2)}^{x_3=\eta(x_1, x_2, t)} (\tilde{u}_1)^2 dx_3 \\
& \quad - \frac{\partial}{\partial x_2} \int_{x_3=-\zeta(x_1, x_2)}^{x_3=\eta(x_1, x_2, t)} \tilde{u}_1 \tilde{u}_2 dx_3
\end{aligned} \tag{2.8}$$

Now, the left hand side of the (2.8) becomes

$$\begin{aligned}
& \frac{\partial}{\partial t}(\phi U_1) + \frac{\partial}{\partial x_1} \{ \phi (U_1)^2 \} + \frac{\partial}{\partial x_2} (\phi U_1 U_2) \\
&= \phi \frac{\partial}{\partial t}(U_1) + U_1 \frac{\partial}{\partial t}(\phi) + U_1 \frac{\partial}{\partial x_1}(\phi U_1) + \phi U_1 \frac{\partial}{\partial x_1}(U_1) \\
& \quad + U_1 \frac{\partial}{\partial x_2}(\phi U_2) + \phi U_2 \frac{\partial}{\partial x_2}(U_1) \\
&= \phi \left( \frac{\partial U_1}{\partial t} + U_1 \frac{\partial U_1}{\partial x_1} + U_2 \frac{\partial U_1}{\partial x_2} \right) + U_1 \left\{ \frac{\partial}{\partial t}(\eta - b) + \frac{\partial}{\partial x_1}(\phi U_1) + \frac{\partial}{\partial x_2}(\phi U_2) \right\} \\
&= \phi \left( \frac{\partial U_1}{\partial t} + \sum_{j=1}^2 U_j \frac{\partial U_1}{\partial x_j} \right) + U_1 \left\{ \frac{\partial}{\partial t}(\eta) + \frac{\partial}{\partial x_1}(\phi U_1) + \frac{\partial}{\partial x_2}(\phi U_2) \right\} \\
&= \phi \left( \frac{\partial U_1}{\partial t} + \sum_{j=1}^2 U_j \frac{\partial U_1}{\partial x_j} \right) \text{ (from (2.6))}
\end{aligned}$$

Now, we change the right hand side of (2.8). For the pressure term, since we have, by (2.7)

$$\begin{aligned}\frac{\partial p}{\partial x_1} &= \frac{\partial p_a}{\partial x_1} + \rho g \frac{\partial \eta}{\partial x_1} \\ \therefore -\frac{1}{\rho} \int_{x_3=-\zeta(x_1, x_2)}^{x_3=\eta(x_1, x_2, t)} \frac{\partial p}{\partial x_1} dx_3 &= -\frac{1}{\rho} \int_{x_3=-\zeta(x_1, x_2)}^{x_3=\eta(x_1, x_2, t)} \left( \frac{\partial p_a}{\partial x_1} + \rho g \frac{\partial \eta}{\partial x_1} \right) dx_3 \\ &= -\frac{1}{\rho} \phi \left( \frac{\partial p_a}{\partial x_1} + \rho g \frac{\partial \eta}{\partial x_1} \right)\end{aligned}$$

Also we have

$$\int_{x_3=-\zeta(x_1, x_2)}^{x_3=\eta(x_1, x_2, t)} f u_2 dx_3 = f \phi U_2$$

For the stress terms, it holds that

$$\begin{aligned}& \frac{1}{\rho} \sum_{j=1}^3 \int_{x_3=-\zeta(x_1, x_2)}^{x_3=\eta(x_1, x_2, t)} \frac{\partial}{\partial x_j} \tau_{1j} dx_3 - \frac{\partial}{\partial x_1} \int_{x_3=-\zeta(x_1, x_2)}^{x_3=\eta(x_1, x_2, t)} (\tilde{u}_1)^2 dx_3 \\ & - \frac{\partial}{\partial x_2} \int_{x_3=-\zeta(x_1, x_2)}^{x_3=\eta(x_1, x_2, t)} \tilde{u}_1 \tilde{u}_2 dx_3 \\ &= \frac{1}{\rho} \sum_{j=1}^2 \frac{\partial}{\partial x_j} \int_{x_3=-\zeta(x_1, x_2)}^{x_3=\eta(x_1, x_2, t)} \tau_{1j} dx_3 - \frac{1}{\rho} \sum_{j=1}^2 (\tau_{1j})|_{x_3=\eta(x_1, x_2, t)} \frac{\partial}{\partial x_j} \eta(x_1, x_2, t) \\ & + \frac{1}{\rho} \sum_{j=1}^2 (\tau_{1j})|_{x_3=-\zeta(x_1, x_2)} \frac{\partial}{\partial x_j} - \zeta(x_1, x_2) + \frac{1}{\rho} (\tau_{13})|_{x_3=\eta(x_1, x_2, t)} - \frac{1}{\rho} (\tau_{13})|_{x_3=-\zeta(x_1, x_2)} \\ & - \frac{\partial}{\partial x_1} \int_{x_3=-\zeta(x_1, x_2)}^{x_3=\eta(x_1, x_2, t)} (\tilde{u}_1)^2 dx_3 - \frac{\partial}{\partial x_2} \int_{x_3=-\zeta(x_1, x_2)}^{x_3=\eta(x_1, x_2, t)} \tilde{u}_1 \tilde{u}_2 dx_3\end{aligned}$$

$$\begin{aligned}
&= \frac{1}{\rho} \frac{\partial}{\partial x_1} \int_{x_3=-\zeta(x_1, x_2)}^{x_3=\eta(x_1, x_2, t)} \{ \tau_{11} - \rho(\tilde{u}_1)^2 \} dx_3 + \frac{1}{\rho} \frac{\partial}{\partial x_2} \int_{x_3=-\zeta(x_1, x_2)}^{x_3=\eta(x_1, x_2, t)} (\tau_{12} - \rho \tilde{u}_1 \tilde{u}_2) dx_3 \\
&+ \frac{1}{\rho} \left\{ (\tau_{13})|_{x_3=\eta(x_1, x_2, t)} - \sum_{j=1}^2 (\tau_{1j})|_{x_3=\eta(x_1, x_2, t)} \frac{\partial}{\partial x_j} \eta(x_1, x_2, t) \right\} \\
&- \frac{1}{\rho} \left\{ (\tau_{13})|_{x_3=-\zeta(x_1, x_2)} - \sum_{j=1}^2 (\tau_{1j})|_{x_3=-\zeta(x_1, x_2)} \frac{\partial}{\partial x_j} - \zeta(x_1, x_2) \right\}
\end{aligned}$$

Here, set

$$\tilde{\tau}_{11} = \frac{1}{\phi} \int_{x_3=-\zeta(x_1, x_2)}^{x_3=\eta(x_1, x_2, t)} \{ \tau_{11} - \rho(\tilde{u}_1)^2 \} dx_3$$

$$\tilde{\tau}_{12} = \frac{1}{\phi} \int_{x_3=-\zeta(x_1, x_2)}^{x_3=\eta(x_1, x_2, t)} (\tau_{12} - \rho \tilde{u}_1 \tilde{u}_2) dx_3$$

$$S_1 = \left\{ (\tau_{13})|_{x_3=\eta(x_1, x_2, t)} - \sum_{j=1}^2 (\tau_{1j})|_{x_3=\eta(x_1, x_2, t)} \frac{\partial}{\partial x_j} \eta(x_1, x_2, t) \right\}$$

$$B_1 = \left\{ (\tau_{13})|_{x_3=-\zeta(x_1, x_2)} - \sum_{j=1}^2 (\tau_{1j})|_{x_3=-\zeta(x_1, x_2)} \frac{\partial}{\partial x_j} - \zeta(x_1, x_2) \right\}$$

Hence, integrating (2.2) from  $-\zeta(x_1, x_2)$  to  $\eta(x_1, x_2, t)$  in the direction  $x_3$ , we have

$$\begin{aligned}
\phi \left( \frac{\partial U_1}{\partial t} + \sum_{j=1}^2 U_j \frac{\partial U_1}{\partial x_j} \right) &= -\frac{1}{\rho} \phi \left( \frac{\partial p_a}{\partial x_1} + \rho g \frac{\partial \eta}{\partial x_1} \right) \\
&+ \frac{1}{\rho} \left\{ \frac{\partial}{\partial x_1} (\phi \tilde{\tau}_{11}) + \frac{\partial}{\partial x_2} (\phi \tilde{\tau}_{12}) \right\} + \frac{1}{\rho} (S_1 - B_1) + f \phi U_2
\end{aligned} \tag{2.9}$$

Similarly, integrating (2.3) from  $-\zeta(x_1, x_2)$  to  $\eta(x_1, x_2, t)$  in the direction  $x_3$ , we have

$$\begin{aligned} \phi \left( \frac{\partial U_2}{\partial t} + \sum_{j=1}^2 U_j \frac{\partial U_2}{\partial x_j} \right) &= -\frac{1}{\rho} \phi \left( \frac{\partial p_a}{\partial x_2} + \rho g \frac{\partial \eta}{\partial x_2} \right) \\ &+ \frac{1}{\rho} \left\{ \frac{\partial}{\partial x_1} (\phi \tilde{\tau}_{21}) + \frac{\partial}{\partial x_2} (\phi \tilde{\tau}_{22}) \right\} + \frac{1}{\rho} (S_2 - B_2) - f \phi U_1 \end{aligned} \quad (2.10)$$

The equation system can be presented in the following way:

$$\frac{\partial}{\partial t} \eta(x_1, x_2, t) + \sum_{j=1}^2 \frac{\partial}{\partial x_j} \{ \phi U_j(x_1, x_2, t) \} = 0, \quad (2.11)$$

$$\begin{aligned} \phi \left( \frac{\partial U_i}{\partial t} + \sum_{j=1}^2 U_j \frac{\partial U_i}{\partial x_j} \right) &= -\frac{1}{\rho} \phi \left( \frac{\partial p_a}{\partial x_i} + \rho g \frac{\partial \eta}{\partial x_i} \right) \\ &+ \frac{1}{\rho} \sum_{j=1}^2 \frac{\partial}{\partial x_j} (\phi \tilde{\tau}_{ij}) + \frac{1}{\rho} (S_i - B_i) + (-1)^{i+1} f \phi U_{i+1}, \end{aligned} \quad (2.12)$$

Where

$$S_i = \theta \rho_a W_i \{ (W_1)^2 + (W_2)^2 \}^{\frac{1}{2}}$$

$$B_i = \frac{\rho g}{C^2} U_i \{ (U_1)^2 + (U_2)^2 \}^{\frac{1}{2}}$$

$$\tilde{\tau}_{ij} = \mu_H \left( \frac{\partial U_i}{\partial x_j} + \frac{\partial U_j}{\partial x_i} \right)$$

$$U_3 = U_1$$

Here,  $\tilde{\tau}_{ij}$  represents the stress in the  $x_i$  direction acting on the  $x_j$  surface,  $S_i$  represents the stress in the  $x_i$  direction acting on the top surface, and  $B_i$  represents the stress in the

---

$x_i$  direction acting on the bottom surface.  $\mu_H$  represents the horizontal viscosity constant [ $Ns/m^2$ ],  $\theta$  represents the wind effect constant,  $\rho_a$  represents the air density,  $W_i$  represents the wind speed in the  $x_i$  direction, and  $C$  represents the Chezy constant [ $m^{1/2}/s$ ].



# Chapter 3

## Theoretical results

In this Chapter theoretical results of the energy estimates for our model is presented. For simplicity, we set  $S_i = B_i = 0$ ,  $i = 1, 2$ ,  $U_i = u_i$ ,  $i = 1, 2$ , and neglect the Coriolis force. Taking all the essential parts we have considered the following mathematical problem which is to be considered in this work.

### 3.1 Statement of the problem

Let  $\Omega \subset \mathbb{R}^2$  be a bounded domain and  $T$  a positive constant. We consider the problem : find  $(\phi, u) : \overline{\Omega} \times [0, T] \rightarrow \mathbb{R} \times \mathbb{R}^2$  such that

$$\begin{cases} \frac{\partial \phi}{\partial t} + \nabla \cdot (\phi u) = 0 & \text{in } \Omega \times (0, T), \\ \rho \phi \left[ \frac{\partial u}{\partial t} + (u \cdot \nabla) u \right] - 2\mu \nabla \cdot (\phi D(u)) + \rho g \phi \nabla \eta = 0 & \text{in } \Omega \times (0, T), \\ \phi = \eta + \zeta & \text{in } \Omega \times (0, T), \end{cases} \quad (3.1)$$

with boundary conditions

$$u = 0 \quad \text{on } \Gamma_D \times (0, T), \quad (3.2)$$

$$(D(u)n) \times n = 0, \quad u \cdot n = 0 \quad \text{on } \Gamma_S \times (0, T), \quad (3.3)$$

$$u = c \frac{\eta}{\phi} n \quad \text{on } \Gamma_T \times (0, T), \quad (3.4)$$

and initial conditions

$$u = u^0, \quad \eta = \eta^0 \quad \text{in } \Omega, \text{ at } t = 0, \quad (3.5)$$

where  $\phi$  is the total height of wave,  $u = (u_1, u_2)^T$  is the velocity,  $\eta : \overline{\Omega} \times [0, T] \rightarrow \mathbb{R}$  is the water level from the reference height,  $\zeta(x) > 0$  ( $x \in \overline{\Omega}$ ) is the depth of water from the reference height, see Figure 2.1,  $D(u) := (\nabla u + (\nabla u)^T)/2$  is the strain-rate tensor,  $n$  is the unit outward normal vector to the boundary of  $\Omega$ ,  $\Gamma := \partial\Omega$  is the boundary of  $\Omega$ , we assume that  $\Gamma$  consists of non-overlapped three parts,  $\Gamma_D$ ,  $\Gamma_S$  and  $\Gamma_T$ , i.e.,  $\overline{\Gamma} = \overline{\Gamma}_D \cup \overline{\Gamma}_S \cup \overline{\Gamma}_T$ ,  $\Gamma_D \cap \Gamma_S = \emptyset$ ,  $\Gamma_S \cap \Gamma_T = \emptyset$ ,  $\Gamma_T \cap \Gamma_D = \emptyset$ , the subscripts “D”, “S”, and “T” mean Dirichlet, slip, and transmission boundaries, respectively,  $\rho > 0$  is a constant which represents the density of water,  $\mu > 0$  is a constant which represents the viscosity,  $g > 0$  is the acceleration due to gravity, and  $c(x) := c_0 \sqrt{g\zeta(x)}$  with a positive constant  $c_0$ . In the rest of paper, we assume  $\zeta \in C^1(\overline{\Omega})$ . It is of interest to note here that [22] studied about the existence, uniqueness and [23] studied about the convergence of a finite element scheme for linearized SWEs but there is no theoretical results, as far as we know, for the existence, uniqueness or regularity for the model (3.1)–(3.5) yet. Also it is pertinent to point out here that  $\phi(x, t) > 0$  for all  $x \in \Omega$  and  $t \in [0, T]$  can not be shown theoretically for (3.1)–(3.5), but for this problem with  $\Gamma_T = \emptyset$ , we have the following Remark.

**Remark 3.1.1.** *If  $\Gamma \in C^2$ ,  $u \cdot n \geq 0$  on  $\Gamma$ ,  $\phi(x, 0) > 0$  for all  $x \in \overline{\Omega}$ , then by the characteristic method it can be shown that  $\phi(x, t) > 0$  for all  $x \in \overline{\Omega}$  and  $t \in [0, T]$ .*

## 3.2 Energy estimate

In this section, we define the total energy and study the stability of solutions to the problem stated in Section 3.1 in terms of the energy. For a solution of (3.1) the total energy  $E(t)$  at time  $t \in [0, T]$  is defined by

$$E(t) := E_1(t) + E_2(t), \quad (3.6)$$

where  $E_1(t)$  and  $E_2(t)$  are the kinetic and the potential energies defined by

$$E_1(t) := \int_{\Omega} \frac{\rho}{2} \phi |u|^2 dx, \quad E_2(t) := \int_{\Omega} \frac{\rho g |\eta|^2}{2} dx.$$

Let symbols  $I_i(t; \Gamma)$ ,  $i = 1, \dots, 3$ , and  $I_4(t; \Omega)$ ,  $t \in [0, T]$ , be integrals defined by

$$\begin{aligned} I_1(t; \Gamma) &:= -\frac{\rho}{2} \int_{\Gamma} \phi |u|^2 u \cdot n ds, & I_2(t; \Gamma) &:= -\rho g \int_{\Gamma} \phi \eta u \cdot n ds, \\ I_3(t; \Gamma) &:= 2\mu \int_{\Gamma} \phi [D(u)n] \cdot u ds, & I_4(t; \Omega) &:= -2\mu \int_{\Omega} \phi |D(u)|^2 dx. \end{aligned}$$

These are used in the rest of this work. Let us assume

$$\phi \in C^1(\overline{\Omega} \times [0, T] : \mathbb{R}), \quad u \in C^1(\overline{\Omega} \times [0, T] : \mathbb{R}^2), \quad (3.7)$$

and

$$\partial_i \partial_j u \in C^1(\overline{\Omega} \times [0, T] : \mathbb{R}^2) \text{ for } i, j = 1, 2. \quad (3.8)$$

**Theorem 3.2.1.** *Suppose that a pair of functions  $(\phi, u) : \overline{\Omega} \times [0, T] \rightarrow \mathbb{R} \times \mathbb{R}^2$  satisfies (3.1) with (3.7) and (3.8). Then, we have*

$$\frac{d}{dt}E(t) = \sum_{i=1}^3 I_i(t; \Gamma) + I_4(t; \Omega). \quad (3.9)$$

We prove Theorem 3.2.1 after preparing a lemma.

**Lemma 3.2.2.** *For the functions  $\phi : \overline{\Omega} \times [0, T] \rightarrow \mathbb{R}$  and  $u : \overline{\Omega} \times [0, T] \rightarrow \mathbb{R}^2$  satisfying (3.7), we have the following.*

$$\begin{aligned} (i) \quad & \frac{\partial}{\partial t}(\phi u) + \nabla \cdot [(\phi u) \otimes u] = \left( \frac{\partial \phi}{\partial t} + \nabla \cdot (\phi u) \right) u + \phi \left( \frac{\partial u}{\partial t} + (u \cdot \nabla) u \right), \\ (ii) \quad & \int_{\Omega} (\nabla \cdot [(\phi u) \otimes u]) \cdot u dx = \frac{1}{2} \int_{\Gamma} \phi |u|^2 u \cdot n ds + \frac{1}{2} \int_{\Omega} [\nabla \cdot (\phi u)] |u|^2 dx. \end{aligned}$$

*Proof.* We prove (i). From the identity,

$$\nabla \cdot [(\phi u) \otimes u] = [\nabla \cdot (\phi u)] u + \phi [(u \cdot \nabla) u], \quad (3.10)$$

we have

$$\begin{aligned} \frac{\partial}{\partial t}(\phi u) + \nabla \cdot [(\phi u) \otimes u] &= \frac{\partial \phi}{\partial t} u + \phi \frac{\partial u}{\partial t} + [\nabla \cdot (\phi u)] u + \phi [(u \cdot \nabla) u] \\ &= \left( \frac{\partial \phi}{\partial t} + \nabla \cdot (\phi u) \right) u + \phi \left( \frac{\partial u}{\partial t} + (u \cdot \nabla) u \right), \end{aligned}$$

which completes the proof of (i).

We prove (ii). Denoting the left hand side of (ii) by  $J$  and using the integration by parts formula, we have

$$\begin{aligned} J &= \int_{\Gamma} [(\phi u) \otimes u] n \cdot u ds - \int_{\Omega} [(\phi u) \otimes u] : \nabla u dx \\ &= \int_{\Gamma} \phi |u|^2 u \cdot n ds - \int_{\Omega} \phi (u \cdot \nabla) u \cdot u dx, \end{aligned} \quad (3.11)$$

where  $A : B = \sum_{i,j=1}^2 A_{ij} B_{ij}$ . We, therefore, have

$$J = \int_{\Omega} [\nabla \cdot (\phi u) |u|^2 + (\phi (u \cdot \nabla) u) \cdot u] dx \quad (\text{from (3.10)})$$

$$= \int_{\Omega} [\nabla \cdot (\phi u)] |u|^2 dx + \int_{\Gamma} \phi |u|^2 u \cdot n ds - J \quad (\text{from (3.11)}),$$

which implies the desired result of (ii).  $\square$

*Proof of Theorem 3.2.1.* Differentiating (3.6) with respect to  $t$ , we get

$$\frac{d}{dt} E(t) = \frac{d}{dt} E_1(t) + \frac{d}{dt} E_2(t). \quad (3.12)$$

We compute  $\frac{d}{dt} E_1(t)$  and  $\frac{d}{dt} E_2(t)$  separately.

Firstly,  $\frac{d}{dt} E_1(t)$  is computed as follows. From Lemma 3.2.2-(i) and the first equation of (3.1), we have

$$\phi \left[ \frac{\partial u}{\partial t} + (u \cdot \nabla) u \right] = \frac{\partial}{\partial t} (\phi u) + \nabla \cdot [(\phi u) \otimes u],$$

which implies

$$\rho \left[ \frac{\partial}{\partial t} (\phi u) + \nabla \cdot [(\phi u) \otimes u] \right] - 2\mu \nabla \cdot [\phi D(u)] + \rho g \phi \nabla \eta = 0. \quad (3.13)$$

Multiplying (3.13) by  $u$  and integrating with respect to  $x$  over  $\Omega$ , we get

$$\begin{aligned} & \rho \int_{\Omega} \left[ \frac{\partial}{\partial t} (\phi u) \right] \cdot u dx + \rho \int_{\Omega} \left[ \nabla \cdot [(\phi u) \otimes u] \right] \cdot u dx - 2\mu \int_{\Omega} \left[ \nabla \cdot (\phi D(u)) \right] \cdot u dx \\ & + \rho g \int_{\Omega} \phi \nabla \eta \cdot u dx = 0. \end{aligned} \quad (3.14)$$

From the equation (3.14) above and the next two identities:

$$\begin{aligned}
& \rho \int_{\Omega} \left[ \frac{\partial}{\partial t} (\phi u) \right] \cdot u \, dx + \rho \int_{\Omega} \left[ \nabla \cdot [(\phi u) \otimes u] \right] \cdot u \, dx \\
&= \rho \int_{\Omega} \left( \frac{\partial \phi}{\partial t} |u|^2 + \phi \frac{\partial u}{\partial t} \cdot u \right) dx + \frac{\rho}{2} \int_{\Gamma} \phi |u|^2 u \cdot n \, ds + \frac{\rho}{2} \int_{\Omega} [\nabla \cdot (\phi u)] |u|^2 \, dx \\
& \hspace{20em} \text{(from Lemma 3.2.2-(ii))} \\
&= \rho \int_{\Omega} \left( \frac{1}{2} \frac{\partial \phi}{\partial t} |u|^2 + \phi u \cdot \frac{\partial u}{\partial t} \right) dx + \frac{\rho}{2} \int_{\Gamma} \phi |u|^2 u \cdot n \, ds \quad \text{(from the first eq. of (3.1))} \\
&= \frac{d}{dt} \left[ \frac{\rho}{2} \int_{\Omega} \phi |u|^2 \, dx \right] + \frac{\rho}{2} \int_{\Gamma} \phi |u|^2 u \cdot n \, ds = \frac{d}{dt} E_1(t) - I_1(t; \Gamma), \\
& \\
& -2\mu \int_{\Omega} \left[ \nabla \cdot (\phi D(u)) \right] \cdot u \, dx = -2\mu \int_{\Gamma} \phi [D(u)n] \cdot u \, ds + 2\mu \int_{\Omega} \phi |D(u)|^2 \, dx \\
& \hspace{10em} = -I_3(t; \Gamma) - I_4(t; \Omega),
\end{aligned}$$

we obtain

$$\frac{d}{dt} E_1(t) = I_1(t; \Gamma) + I_3(t; \Gamma) + I_4(t; \Omega) - \rho g \int_{\Omega} \nabla \eta \cdot (\phi u) \, dx. \quad (3.15)$$

Secondly,  $\frac{d}{dt} E_2(t)$  is computed as follows:

$$\begin{aligned}
\frac{d}{dt} E_2(t) &= \frac{d}{dt} \left[ \frac{\rho g}{2} \int_{\Omega} |\eta|^2 \, dx \right] \\
&= \rho g \int_{\Omega} \eta \frac{\partial \eta}{\partial t} \, dx \\
&= \rho g \int_{\Omega} \eta \frac{\partial \phi}{\partial t} \, dx && \text{(from the third eq. of (3.1))} \\
&= \rho g \int_{\Omega} \eta [-\nabla \cdot (\phi u)] \, dx && \text{(from the first eq. of (3.1))} \\
&= -\rho g \int_{\Omega} \nabla \cdot (\eta \phi u) \, dx + \rho g \int_{\Omega} \nabla \eta \cdot (\phi u) \, dx \\
&= I_2(t; \Gamma) + \rho g \int_{\Omega} \nabla \eta \cdot (\phi u) \, dx. \quad (3.16)
\end{aligned}$$

The result (3.9) follows by adding (3.15) and (3.16) and recalling (3.12).  $\square$

**Corollary 3.2.3.** (i) *Suppose that a pair of functions  $(\phi, u) : \overline{\Omega} \times [0, T] \rightarrow \mathbb{R} \times \mathbb{R}^2$  satisfies (3.1) with (3.2)-(3.4), (3.7) and (3.8). Then, we have*

$$\frac{d}{dt}E(t) = \sum_{i=1}^3 I_i(t; \Gamma_T) + I_4(t; \Omega). \quad (3.17)$$

(ii) *Furthermore, if  $\Gamma = \Gamma_D \cup \Gamma_S$  and  $\phi(x, t) > 0$  ( $(x, t) \in \overline{\Omega} \times [0, T]$ ), we have*

$$\frac{d}{dt}E(t) = I_4(t; \Omega) \leq 0. \quad (3.18)$$

*Proof.* On  $\Gamma_S$ , from the first equation of (3.3), there exists a scalar function  $w : \overline{\Omega} \times [0, T] \rightarrow \mathbb{R}$  such that  $D(u)n = w(x, t)n$ , which implies

$$[D(u)n] \cdot u = (wn) \cdot u = w(u \cdot n) = 0.$$

Hence, the result (3.17) is established from Theorem 3.2.1 with (3.2) and (3.3).

When  $\Gamma = \Gamma_D \cup \Gamma_S$ , i.e.,  $\Gamma_T = \emptyset$ , the identity (3.17) implies (3.18).  $\square$

It is to be noted here that the definition (3.6), Lemma 3.2.2-(ii) and Corollary 3.2.3-(ii) can also be found in [21], where  $u \cdot n = 0$  is assumed.

**Theorem 3.2.4.** *Suppose that a pair of functions  $(\phi, u) : \overline{\Omega} \times [0, T] \rightarrow \mathbb{R} \times \mathbb{R}^2$  satisfies (3.1) with (3.2)-(3.4), (3.7), (3.8) and an inequality*

$$\phi(x, t) > 0, \quad (x, t) \in \overline{\Gamma}_T \times [0, T], \quad (3.19)$$

and that there exists  $\alpha \in (0, 1)$  such that

$$\eta(x, t) \geq -\alpha \zeta(x), \quad x \in \bar{\Gamma}_T, \quad t \in [0, T], \quad (3.20)$$

$$0 < c_0 \leq \sqrt{\frac{2}{\alpha}}(1 - \alpha). \quad (3.21)$$

Then, we have the following estimates:

$$I_1(t; \Gamma_T) + I_2(t; \Gamma_T) \leq 0, \quad (3.22)$$

in particular,

$$\frac{d}{dt}E(t) \leq I_3(t; \Gamma_T). \quad (3.23)$$

*Proof.* We prove (3.22), then (3.17) and (3.22) imply (3.23), since  $I_4(t; \Omega)$  is always non-positive. We have

$$\begin{aligned} \sum_{i=1}^2 I_i(t; \Gamma_T) &= -\rho \int_{\Gamma_T} \phi(u \cdot n) \left[ g\eta + \frac{1}{2}|u|^2 \right] ds \\ &= -\rho \int_{\Gamma_T} \phi c \frac{\eta}{\phi} \left[ g\eta + \frac{1}{2}c_0^2 g \zeta \frac{\eta^2}{\phi^2} \right] ds \\ &= -\rho g \int_{\Gamma_T} c \eta^2 \left[ 1 + \frac{c_0^2}{2} \frac{\zeta \eta}{(\zeta + \eta)^2} \right] ds. \end{aligned}$$

Let  $f(r) := r/(1+r)^2$ . From  $f'(r) = (1-r)/(1+r)^3$ , it holds that  $f(r_1) \leq f(r_2)$  for  $-1 < r_1 \leq r_2 \leq 1$ . If  $\eta < 0$ , then since  $-1 \leq -\alpha \leq \eta/\zeta \leq 0$ , we obtain  $f(-\alpha) \leq f(\eta/\zeta)$ . Again if  $\eta \geq 0$  then we also have  $f(-\alpha) < 0 < f(\eta/\zeta)$ . In both cases we obtain  $f(-\alpha) \leq f(\eta/\zeta)$  i.e.,

$$-\frac{\alpha}{(1-\alpha)^2} \leq \frac{\eta \zeta}{(\zeta + \eta)^2},$$

which implies that

$$\sum_{i=1}^2 I_i(t; \Gamma_T) \leq -\rho g \int_{\Gamma_T} c \eta^2 \left\{ 1 - \frac{c_0^2 \alpha}{2(1-\alpha)^2} \right\} ds \leq 0$$

from the condition (3.21). □

**Remark 3.2.5.** We observe numerically that  $I_2(t; \Gamma)$  is dominant and  $\sum_{i=1}^3 I_i(t; \Gamma)$  is negative, while  $I_1(t; \Gamma)$  and  $I_3(t; \Gamma)$  may be positive, cf. Subsection 4.1.2. Although the sign of  $\frac{d}{dt}E(t)$  is as yet unknown due to  $I_3(t; \Gamma_T)$ , from the numerical results we can say that the transmission boundary condition (3.4) is reasonable under the conditions (3.19)-(3.21) to be satisfied in practical computation.

**Remark 3.2.6.** The condition (3.21) is not strict in the practical computation, where  $\alpha$  and  $c_0$  are chosen typically as, e.g.,  $\alpha = 0.01$  and  $c_0 = 0.9$  [20]. These satisfy (3.21), since  $\sqrt{2/\alpha}(1-\alpha) \approx 14$ .



# Chapter 4

## Numerical results by FDM

In this Chapter, we present numerical results by a finite difference scheme for problem (3.1)–(3.5). Considering five different cases of boundary setting, we have presented results for numerical simulation in a square domain. We have also presented results for energy, derivative of energy and  $I_{hi}^k$ ,  $i = 1, \dots, 4$  for that five cases. Two tables are also presented, the first one is for the maximum and minimum values of  $I_{hi}^k$ ,  $i = 1, \dots, 4$ , and the second one is for the choice of  $c_0$ .

### 4.1 Problem setting

For the numerical computation we set  $\Omega = (0, L)^2$  for a positive constant  $L$ ,  $T = 100$ ,  $\zeta = a > 0$ ,  $\mu = 1$ ,  $g = 9.8 \times 10^{-3}$ ,  $\rho = 10^{12}$ ,  $\eta^0 = c_1 \exp(-100|x - p|^2)$  ( $c_1 > 0$ ,  $p \in \Omega$ ). As the real domain is very large, we consider the length in km scale. So the above values are in km (length), kg (mass) and s (time). We set  $\Gamma_S = \emptyset$  for simplicity. We consider five cases of  $\Gamma_T$ :

$$\begin{aligned} (i) \Gamma_T &= \emptyset, & (ii) \Gamma_T &= \Gamma_{\text{top}}, & (iii) \Gamma_T &= \Gamma_{\text{top}} \cup \Gamma_{\text{right}} \cup \{(L, L)\}, \\ (iv) \Gamma_T &= \Gamma_{\text{top}} \cup \Gamma_{\text{right}} \cup \Gamma_{\text{left}} \cup \{(L, L)\} \cup \{(0, L)\}, & (v) \Gamma_T &= \Gamma, \end{aligned}$$

for  $\Gamma_{\text{top}} := \{(x_1, L); 0 < x_1 < L\}$ ,  $\Gamma_{\text{right}} := \{(L, x_2); 0 < x_2 < L\}$ ,  $\Gamma_{\text{left}} := \{(0, x_2); 0 < x_2 < L\}$ , and set  $\Gamma_D = \Gamma \setminus \Gamma_T$ . For the above cases (ii)-(v),  $c_0 = 0.9$  is taken following [20].

#### 4.1.1 A finite difference scheme

Let  $N \in \mathbb{N}$  and  $\Delta t > 0$  be given, and let  $h := L/N$  and  $N_T := \lfloor T/\Delta t \rfloor$ ,  $x_{i,j} := (ih, jh)^T \in \mathbb{R}^2$  ( $i, j \in \mathbb{Z}$ ),  $\Omega_h := \{x_{i,j} \in \Omega; i, j \in \mathbb{Z}\}$ ,  $\overline{\Omega}_h := \{x_{i,j} \in \overline{\Omega}; i, j \in \mathbb{Z}\}$ ,  $\Gamma_{hD} := \{x_{i,j} \in \overline{\Gamma}_D; i, j \in \mathbb{Z}\}$ ,  $\Gamma_{hT} := \{x_{i,j} \in \Gamma_T; i, j \in \mathbb{Z}\}$ . Let  $u_h^0 : \overline{\Omega}_h \rightarrow \mathbb{R}^2$  and  $\phi_h^0 : \overline{\Omega}_h \rightarrow \mathbb{R}$  be given approximate functions of  $u^0$  and  $\phi^0$ , respectively. Our finite difference scheme is to find  $\{(\phi_h^k, u_h^k)(x_{i,j}); x_{i,j} \in \overline{\Omega}_h, k = 1, \dots, N_T\}$  such that, for  $k = 0, \dots, N_T - 1$ ,

$$\left\{ \begin{array}{ll} \frac{\phi_h^{k+1} - \phi_h^k}{\Delta t} + (\nabla_h \cdot u_h^k) \phi_h^k + u_h^k \cdot \nabla_h^{up} \phi_h^k = 0 & \text{on } \overline{\Omega}_h, \\ \rho \phi_h^k \left( \frac{u_h^{k+1} - u_h^k}{\Delta t} + (u_h^k \cdot \nabla_h) u_h^k \right) \\ \quad - 2\mu \nabla_h \cdot (\phi_h^k D_h(u_h^k)) + \rho g \phi_h^k \nabla_h \eta_h^k = 0 & \text{on } \Omega_h, \\ \phi_h^k = \eta_h^k + \zeta & \text{on } \Omega_h, \\ u_h^{k+1} = u_D^{k+1} & \text{on } \Gamma_{hD}, \\ u_h^{k+1} = c \frac{\phi_h^{k+1} - \zeta}{\phi_h^{k+1}} n & \text{on } \Gamma_{hT}, \end{array} \right. \quad (4.1)$$

where  $\nabla_h = (\nabla_{h1}, \nabla_{h2})^T$  and  $\nabla_h^{up} = (\nabla_{h1}^{up}, \nabla_{h2}^{up})^T$  represent the (standard) central and upwind (with respect to  $u_h^k$ ) difference operators, respectively, and  $D_h(v_h) := [(\nabla_h v_h) + (\nabla_h v_h)^T]/2 : \overline{\Omega}_h \rightarrow \mathbb{R}_{\text{sym}}^{2 \times 2}$  for  $v_h : \overline{\Omega}_h \rightarrow \mathbb{R}^2$ . If the required points for the operators  $\nabla_h$  and  $\nabla_h^{up}$  are not in  $\overline{\Omega}_h$ , one sided difference is used.

#### 4.1.2 Numerical results for five cases of boundary settings

Numerical simulations are carried out by scheme (4.1) for  $L = 10$ ,  $a = 1$ ,  $u^0 = 0$ ,  $c_1 = 0.01$ ,  $p = (5, 5)^T$ ,  $N = 1,000$  and  $\Delta t = 0.05$  ( $N_T = 2,000$ ). Figure 4.1 shows color contours of  $\eta_h^k$

for  $k = 0, 500, 1,000, 1,500$  and  $2,000$ , which correspond to times  $t = 0, 25, 50, 75$  and  $100$ , respectively, where (i)-(v) represent simulated results for the cases (i)-(v) stated in the Section 4.1. It can be clearly found that the artificial reflection is almost removed on the transmission boundaries for the cases (ii)-(v).

### 4.1.3 Numerical study of energy estimate

In this subsection, we study the stability of solutions to the problem (3.1)-(3.5) numerically by scheme (4.1) in terms of the energy  $E(t)$  defined in (3.6). The values of  $E(t^k)$  and  $I_i(t^k; \Gamma)$ ,  $i = 1, 2, 3$ ,  $I_4(t^k; \Omega)$  are approximately computed by using solution  $\{(u_h^k, \phi_h^k)\}_{k=1}^{N_T}$  with  $\{\eta_h^k\}_{k=1}^{N_T}$  of scheme (4.1) as

$$\begin{aligned} E(t^k) &\approx E_h^k: = \frac{\rho}{2} h^2 \sum_{x_{i,j} \in \Omega_h} \phi_h^k(x_{i,j}) |u_h^k(x_{i,j})|^2 + \frac{\rho g}{2} h^2 \sum_{x_{i,j} \in \Omega_h} |\eta_h^k(x_{i,j})|^2, \\ I_1(t^k; \Gamma) &\approx I_{h1}^k: = -\frac{\rho}{2} \int_{\Gamma} (\Pi_h \phi_h^k) |\Pi_h u_h^k|^2 (\Pi_h u_h^k) \cdot n \, ds, \\ I_2(t^k; \Gamma) &\approx I_{h2}^k: = -\rho g \int_{\Gamma} (\Pi_h \phi_h^k) (\Pi_h \eta_h^k) (\Pi_h u_h^k) \cdot n \, ds, \\ I_3(t^k; \Gamma) &\approx I_{h3}^k: = 2\mu \sum_{m=1}^N \left( \int_{\ell_m^T} + \int_{\ell_m^B} + \int_{\ell_m^L} + \int_{\ell_m^R} \right) (\Pi_h \phi_h^k) (D(\Pi_h u_h^k) n) \cdot (\Pi_h u_h^k) \, ds, \\ I_4(t^k; \Omega) &\approx I_{h4}^k: = -2\mu h^2 \sum_{i,j=1}^N (\Pi_h \phi_h^k)(x_{i-1/2,j-1/2}) |D_h(u_h^k)(x_{i-1/2,j-1/2})|^2, \end{aligned}$$

where  $\Pi_h f_h \in C(\overline{\Omega}; \mathbb{R})$  is the bilinear interpolation of  $f_h: \overline{\Omega}_h \rightarrow \mathbb{R}$  for  $f_h = \phi_h, \eta_h$ ,  $\Pi_h u_h = (\Pi_h u_{h1}, \Pi_h u_{h2})^T \in C(\overline{\Omega}; \mathbb{R}^2)$ , the boundary is represented as  $\overline{\Gamma} = \bigcup_{m=1}^N (\overline{\ell}_m^T \cup \overline{\ell}_m^B \cup \overline{\ell}_m^L \cup \overline{\ell}_m^R)$  for line segments  $\ell_m^T, \ell_m^B, \ell_m^L, \ell_m^R$  defined by  $\ell_m^T: = \overline{x_{m-1,N} x_{m,N}}$ ,  $\ell_m^B: = \overline{x_{m-1,0} x_{m,0}}$ ,  $\ell_m^L: = \overline{x_{0,m-1} x_{0,m}}$ ,  $\ell_m^R: = \overline{x_{N,m-1} x_{N,m}}$ , and the domain is represented as  $\overline{\Omega} = \bigcup_{i,j=1}^N \overline{\omega}_{i-1/2,j-1/2}$  for  $\omega_{i-1/2,j-1/2}: = ((i-1)h, ih) \times ((j-1)h, jh) \subset \Omega$  with the area  $h^2$ .

Numerical simulations for the problem (3.1)-(3.5) with  $L = 1$ ,  $a = 0.1$ ,  $u^0 = 0$ ,  $c_1 = 0.001$ ,  $p = (0.5, 0.5)^T$  are carried out by scheme (4.1) with  $\Delta t = 2h$  for  $h = L/N = 1/N$ ,  $N = 400, 500, 800$  and  $1,000$ . The results are presented in Figure 4.2, where (i)-(v) in the figure

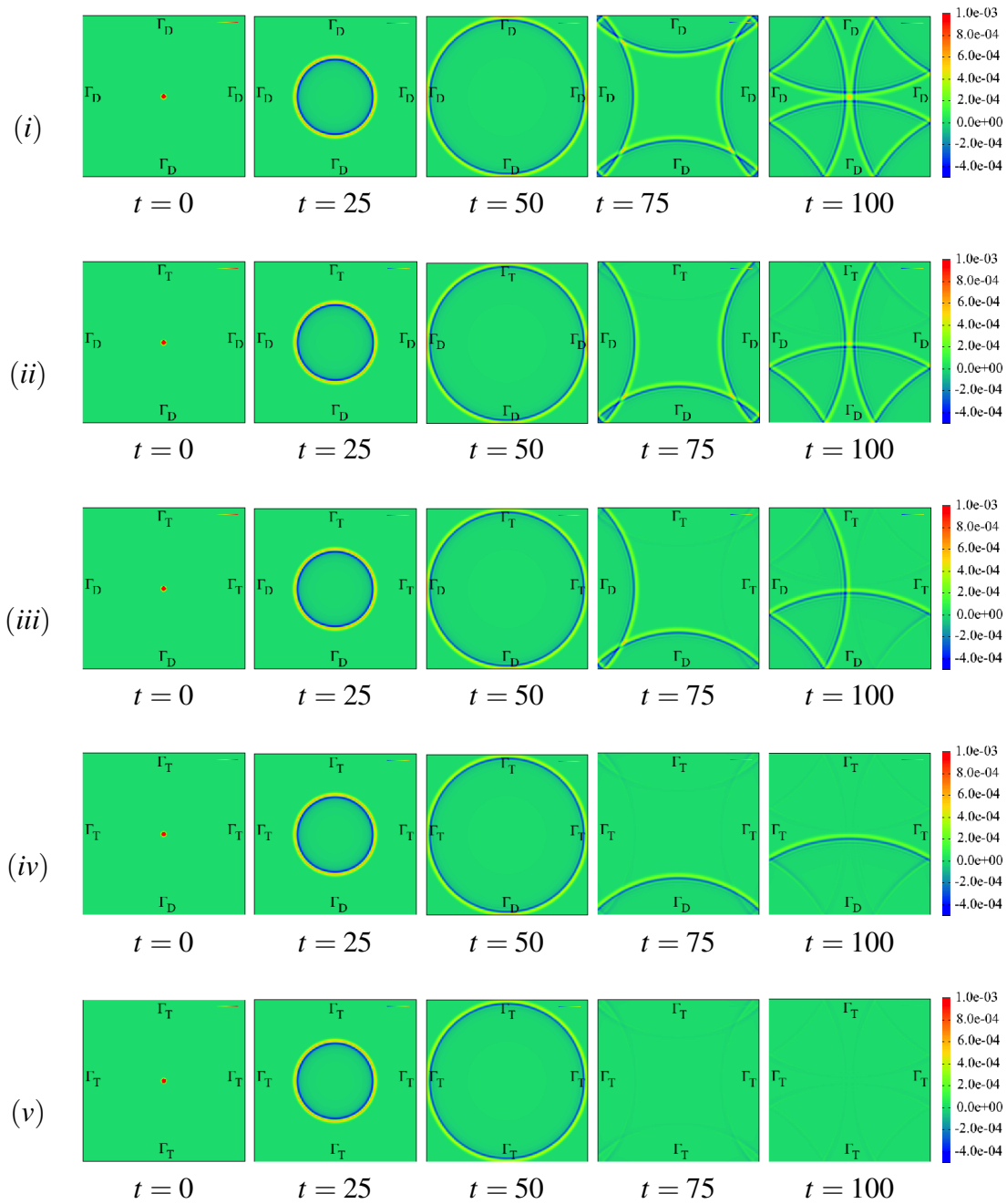


Fig. 4.1 Color contours of  $\eta_h^k$  by finite difference scheme (4.1) for the five cases (i)-(v) discussed in Subsection 4.1.2.

represent the cases (i)-(v) stated in the Section 4.1. The graphs of  $E_h^k$  and  $\sum_{i=1}^4 I_{hi}^k$  versus  $t = t^k$  ( $k \in \mathbb{N}$ ) are presented in the left and center figures, respectively. There are four lines in each figure, but the lines are almost overlapped in the cases of (ii)-(v). In the case of (i) the graphs are qualitatively similar. The right figures show the graphs of  $I_{hi}^k$ ,  $i = 1, \dots, 4$  versus  $t = t^k$  ( $k \in \mathbb{N}$ ) for  $dt = 0.002$  and  $dx = 0.001$ . The maximum and minimum values of  $I_{hi}^k$ ,  $i = 1, \dots, 4$ , on the time interval  $(0, T)$  are presented in Table 4.1 for  $dt = 0.002$  and  $dx = 0.001$ .

From the numerical results presented in Figure 4.2, it can be found that the total energy is mainly decreasing with respect to time. In the case of (i), i.e.,  $\Gamma = \Gamma_D$ , we can see that at the early period the graphs are increasing, while the values are small. From the Figure 4.3, it can be clearly seen that the sum  $\sum_{i=1}^4 I_{hi}^k$  corresponding to the derivative of the total energy is always non-positive, which confirms the stability of solutions to the model numerically. From Figure 4.4 and Table 4.1, it can be observed that the value of  $I_{h2}$  is dominating negatively over  $I_{h1}$  and  $I_{h3}$  so that the sum  $\sum_{i=1}^4 I_{hi}$  becomes non-positive always.

Table 4.1 Maximum and minimum values of  $I_{hi}^k$ ,  $i = 1, \dots, 4$ , with respect to the number of transmission boundaries

$\Gamma_T$	$\Gamma_D$		$I_{h1}$	$I_{h2}$	$I_{h3}$	$I_{h4}$
0	4	Max	0.00	0.00	0.00	0.00
		Min	0.00	0.00	0.00	$-8.63 \times 10^{-7}$
1	3	Max	$1.10 \times 10^{-4}$	0.00	$1.44 \times 10^{-9}$	0.00
		Min	$-2.59 \times 10^{-3}$	-3.37	$-1.25 \times 10^{-9}$	$-3.76 \times 10^{-7}$
2	2	Max	$1.86 \times 10^{-4}$	0.00	$1.72 \times 10^{-9}$	0.00
		Min	$-3.38 \times 10^{-3}$	-6.27	$-2.50 \times 10^{-9}$	$-2.31 \times 10^{-7}$
3	1	Max	$1.43 \times 10^{-4}$	0.00	$2.58 \times 10^{-9}$	0.00
		Min	$-5.06 \times 10^{-3}$	-9.40	$-3.75 \times 10^{-9}$	$-1.74 \times 10^{-7}$
4	0	Max	$2.87 \times 10^{-4}$	0.00	$3.47 \times 10^{-9}$	0.00
		Min	$-6.75 \times 10^{-3}$	-12.54	$-5.01 \times 10^{-9}$	$-1.14 \times 10^{-7}$

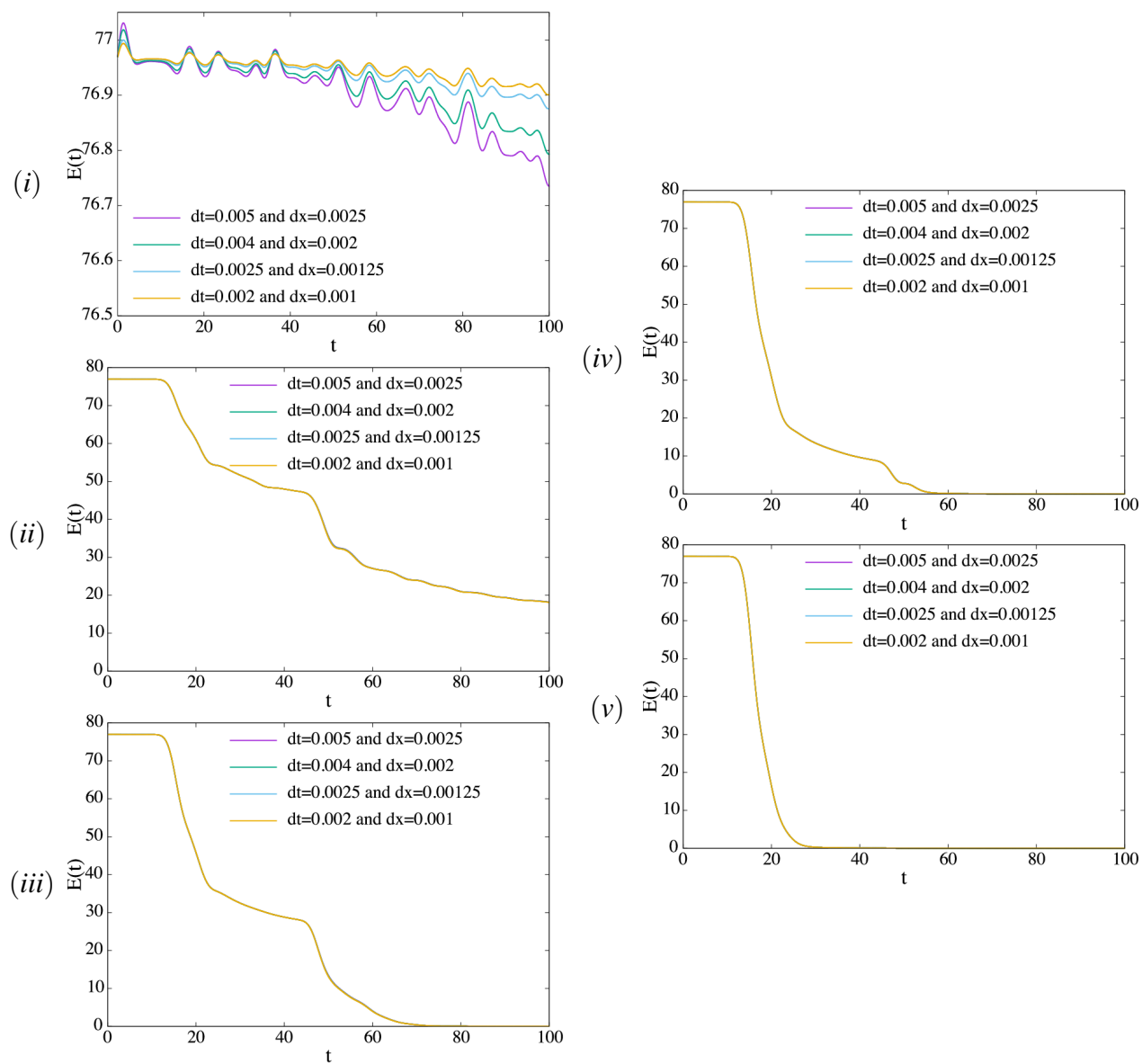


Fig. 4.2 Graphs of  $E_h^k$  versus  $t = t^k (\geq 0, k \in \mathbb{Z})$  for the five cases (i)-(v).

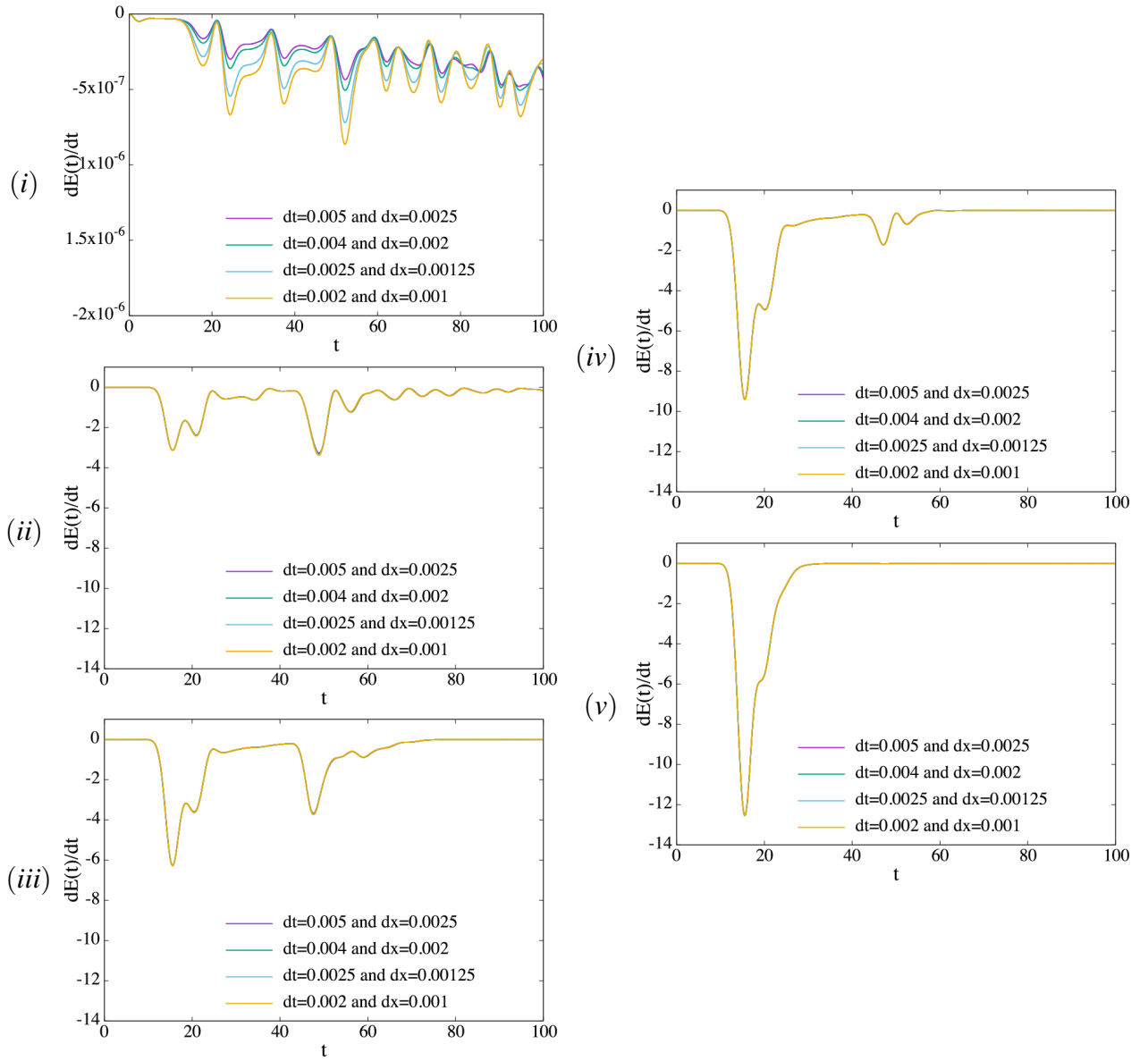


Fig. 4.3 Graphs of  $\sum_{i=1}^4 I_{hi}^k \approx \frac{d}{dt} E(t)$  versus  $t = t^k (\geq 0, k \in \mathbb{Z})$  for the five cases (i)-(v).

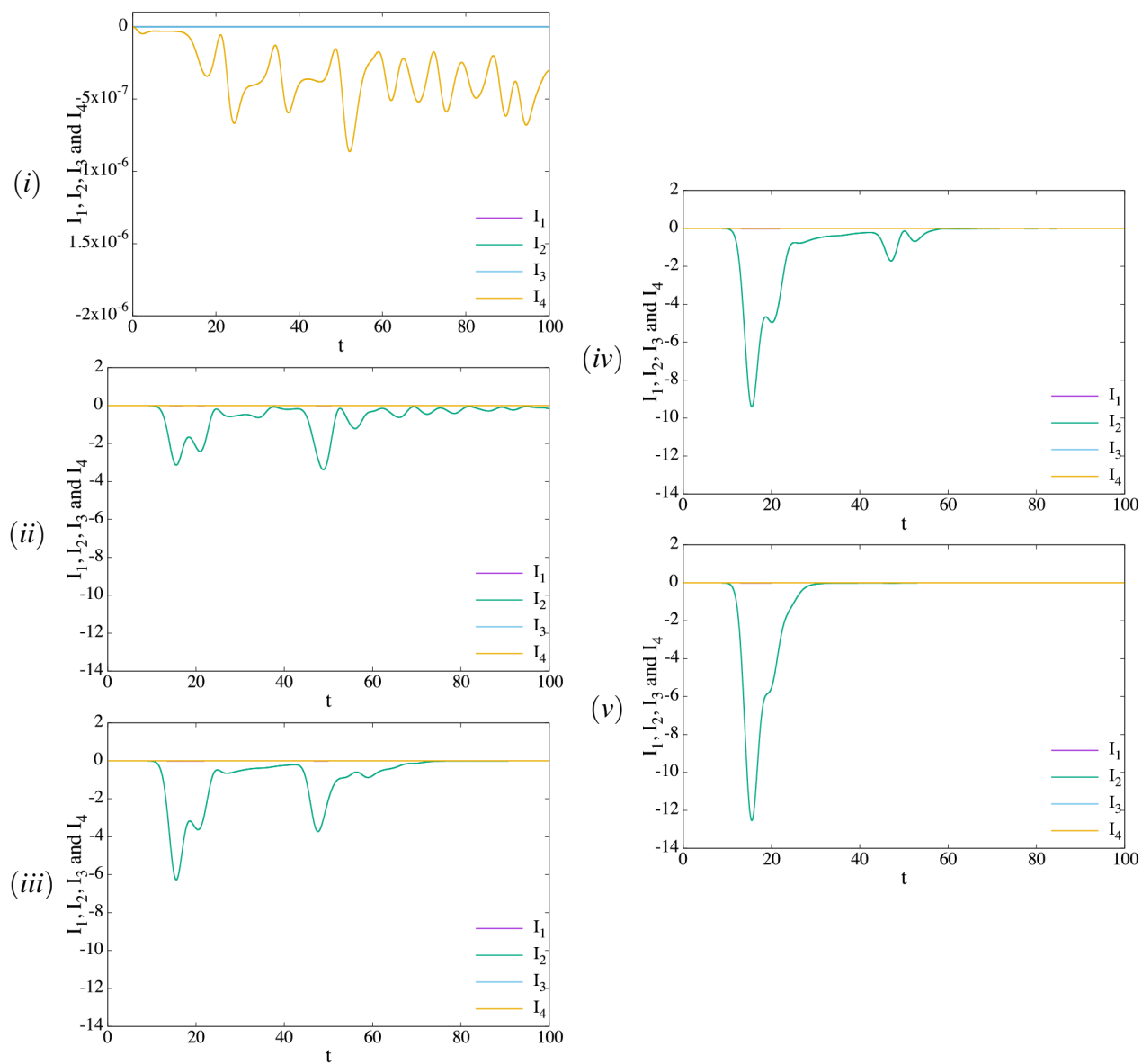


Fig. 4.4 Graphs of  $I_{hi}^k, i = 1, \dots, 4$  versus  $t = t^k (\geq 0, k \in \mathbb{Z})$  for the five cases (i)-(v).

#### 4.1.4 Choice of $c_0$

In this subsection, we study the value of  $c_0$  by solving the problem with  $L = 1$ ,  $a = 0.1$ ,  $p = (0.5, 0.5)^T$  and  $c_0 = 0.1, 0.2, \dots, 1.2$  and  $1.5$  by scheme (4.1) with  $N = 400$ ,  $\Delta t = 0.005$  ( $N_T = 20,000$ ), and by computing

$$S_h^k(c_0) := \left\{ h^2 \sum_{x_{i,j} \in \overline{\Omega}_h} \eta_h^k(x_{i,j})^2 \right\}^{\frac{1}{2}} \approx S(t^k; c_0) := \left\{ \int_{\Omega} |\eta^k(x)|^2 dx \right\}^{\frac{1}{2}} = \|\eta^k\|_{L^2(\Omega)},$$

$$\mathcal{S}_h(c_0) := \left\{ \Delta t \sum_{k=0}^{N_T} S_h^k(c_0)^2 \right\}^{\frac{1}{2}} \approx \mathcal{S}(c_0) := \left\{ \int_0^T |S(t^k; c_0)|^2 dt \right\}^{\frac{1}{2}} = \|\eta\|_{L^2(0,T;L^2(\Omega))}.$$

We set six different cases for the initial values of  $\eta^0$  and  $u^0$  as follows.

Case I:	$\eta^0 = c_1 \exp(-100  x - (0.5, 0.5) ^2),$	$u^0 = 0,$
Case II:	$\eta^0 = c_1 \exp(-200  x - (0.5, 0.5) ^2),$	$u^0 = 0,$
Case III:	$\eta^0 = c_1 \exp(-100  x - (0, 0.5) ^2),$	$u^0 = 0,$
Case IV:	$\eta^0 = c_1 \exp(-100  x ^2),$	$u^0 = 0,$
Case V:	$\eta^0 = c_1 \exp(-100  x - (0.5, 0.5) ^2),$	$u^0 = 10^{-4} (1, 1)^T,$
Case VI:	$\eta^0 = c_1 \exp(-100  x - (0.5, 0.5) ^2),$	$u^0 = 10^{-4} (1, -1)^T,$

where  $c_1 = 10^{-3}$ .

Since the artificial reflection should be removed after the time the wave touches the transmission boundary, we find a value of  $c_0$  which provides the minimum of  $\mathcal{S}_h(c_0)$ . The results are presented in Table 4.2, from where it can be concluded that for the case of zero initial velocity the suitable value of  $c_0$  lies in  $[0.7, 1.0]$  and for the case of nonzero initial velocity we cannot say anything yet.

Table 4.2  $c_0$  and  $\mathcal{S}_h(c_0)$ 

$c_0$	$\mathcal{S}_h(c_0)$					
	Case I	Case II	Case III	Case IV	Case V	Case VI
0.1	12.17	8.53	8.14	5.47	44.48	44.49
0.2	9.89	6.97	6.35	4.04	34.36	34.37
0.3	8.84	6.24	5.52	3.35	28.74	28.75
0.4	8.27	5.85	5.08	2.98	25.23	25.24
0.5	7.93	5.61	4.84	2.79	22.82	22.83
0.6	7.71	5.46	4.71	2.69	21.05	21.06
0.7	7.58	5.37	4.65	<u>2.66</u>	19.69	19.69
0.8	7.51	5.32	<u>4.63</u>	2.67	18.60	18.61
0.9	<u>7.4805</u>	<u>5.2969</u>	4.64	2.70	17.71	17.72
1.0	<u>7.4807</u>	<u>5.2977</u>	4.68	2.76	16.98	16.98
1.1	7.50	5.32	4.73	2.82	16.36	16.36
1.2	7.55	5.35	4.79	2.89	15.83	15.84
1.5	7.75	5.49	5.02	3.12	14.66	14.66

# Chapter 5

## Numerical results by LGM

In this Chapter, firstly, we have presented a LG scheme for the problem described in Section 3.1. Secondly, we have presented results for numerical simulation in a square domain for the five cases of boundary setting described in the Section 4.1. Thirdly, results for energy, derivative of energy and  $I_{ii}^k, i = 1, \dots, 4$  for that five cases are also presented. After that results for the experimental order of convergence of the LG scheme are also presented for several norms. Then simulated results in the Bay of Bengal for two different cases of boundary setting are presented. Finally, graphs of  $\eta$  on the transmission boundary, graphs of mass and graphs of  $L^2$  norm are shown for that two cases.

### 5.1 LG scheme

Let  $\mathcal{T}_h = \{K\}$  be a triangulation of  $\Omega$ , and  $M_h$  the so-called P1 (piecewise linear) finite element space. We set  $\Psi_h := M_h$  for the water level  $\eta$ , and

$$V_h(\Psi_h) := \left\{ \begin{array}{l} v_h \in M_h^2; \\ v_h(P) = c(P) \frac{\Psi_h(P) - \zeta(P)}{\Psi_h(P)} n(P), \quad \forall P : \text{node on } \Gamma_T, \\ v_h(Q) = 0, \quad \forall Q : \text{node on } \Gamma_D \end{array} \right\}$$

for the velocity  $u$ . The LG scheme is to find  $\{(\phi_h^k, u_h^k)\}_{k=1}^{N_T} \subset \Psi_h \times V_h$  such that, for  $k = 1, \dots, N_T$ ,

$$\left\{ \begin{array}{l} \int_{\Omega} \frac{\phi_h^k - \tilde{\phi}_h^{k-1} \circ X_{1h}^{k-1} \gamma_h^{k-1}}{\Delta t} \psi_h dx = 0, \quad \forall \psi_h \in \Psi_h, \\ \rho \int_{\Omega} \phi_h^k \frac{u_h^k - \tilde{u}_h^{k-1} \circ X_{1h}^{k-1}}{\Delta t} \cdot v_h dx + 2\mu \int_{\Omega} \phi_h^k D(u_h^k) : D(v_h) dx \\ \quad + \rho g \int_{\Omega} \phi_h^k \nabla \eta_h^k \cdot v_h dx = 0, \quad \forall v_h \in V_h, \\ \phi_h^k = \eta_h^k + \Pi_h^{\text{FEM}} \zeta, \end{array} \right. \quad (5.1)$$

where  $X_{1h}^k(x) := x - u_h^k(x) \Delta t$ ,  $\gamma_h^k : \Omega \rightarrow \mathbb{R}$  is defined by

$$\gamma_h^k(x) := \det\left(\frac{\partial X_{1h}^k(x)}{\partial x}\right),$$

the symbol “ $\circ$ ” represents the composition of functions, i.e.,  $[v_h \circ X_{1h}^k](x) := v_h(X_{1h}^k(x))$ ,  $\Pi_h^{\text{FEM}} : C(\overline{\Omega}) \rightarrow M_h$  is the Lagrange interpolation operator, and

$$\tilde{\psi}_h(x) = \begin{cases} \psi_h(x), & x \in \overline{\Omega}, \\ \psi_h(P_x), & x \in \mathbb{R}^2 \setminus \overline{\Omega}, \end{cases}$$

where  $P_x \in \Gamma$  is the “nearest” nodal point from  $x$ . In each step, firstly,  $\phi_h^k \in \Psi_h$  is obtained from the first equation of scheme (5.1). Secondly,  $u_h^k \in V_h$  is obtained by using  $\phi_h^k$  from the second equation. In the first equation of (5.1), the idea of mass conservative Lagrange–Galerkin scheme [45] is employed.

### 5.1.1 Numerical results for five cases of boundary settings

A numerical simulation is carried out by LG scheme (5.1) with the same setting described in Subsection 4.1.2 except  $\Delta t$ , where it is set as  $\Delta t = 0.0625$ . The results are shown in

Figure 5.1. The figures are similar to the ones in Figure 4.1 obtained by finite difference scheme (4.1) and support the results in Figure 4.1.

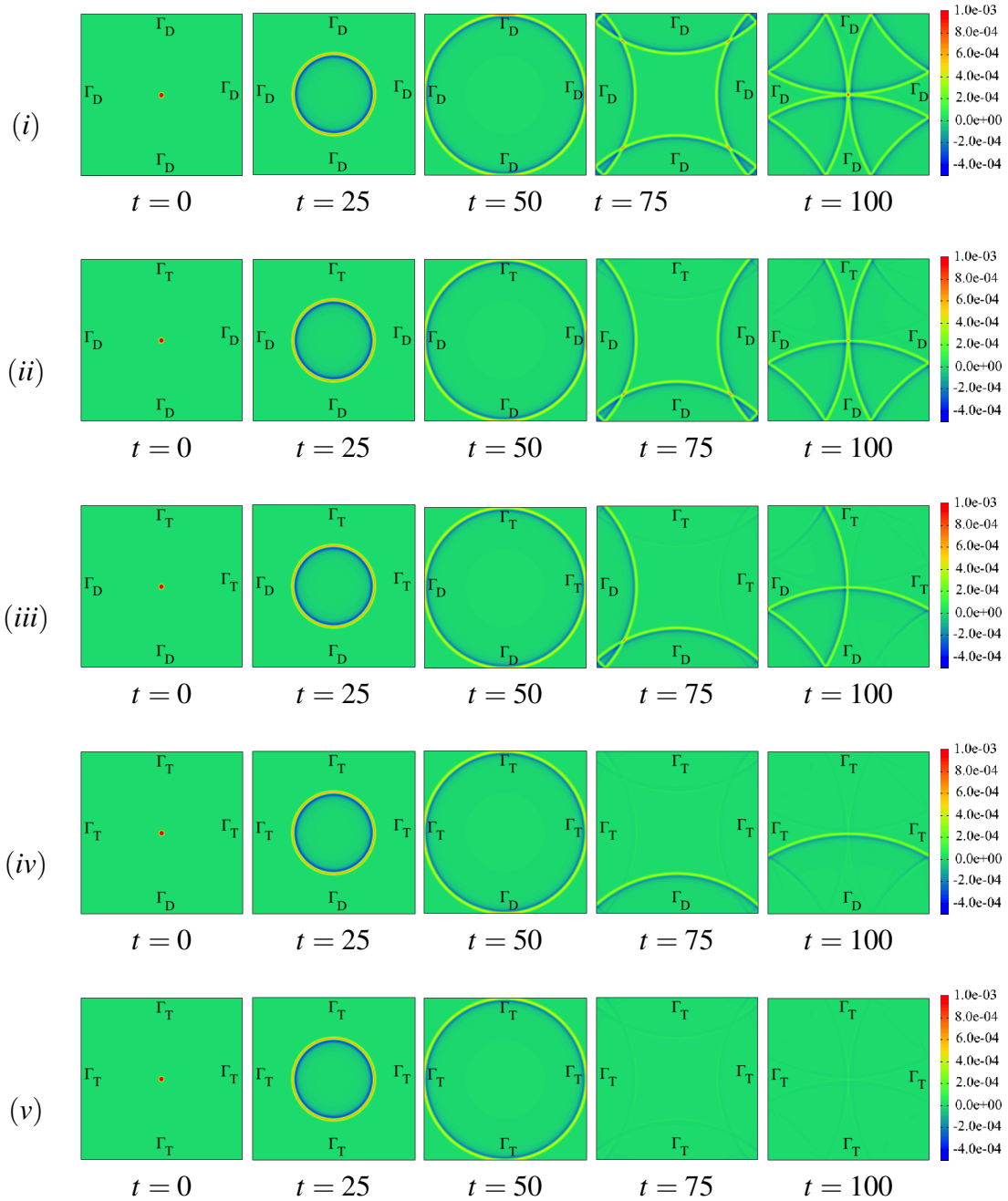


Fig. 5.1 Color contours of  $\eta_h^k$  by LG scheme (4.1) for the five cases (i)-(v) discussed in Section 4.1.

### 5.1.2 Numerical study of energy estimate

In this subsection, we study the stability of solutions to the problem (3.1)-(3.5) numerically by scheme (5.1) in terms of the energy  $E(t)$  defined in (3.6). The values of  $E(t^k)$  and  $I_i(t^k; \Gamma)$ ,  $i = 1, 2, 3$ ,  $I_4(t^k; \Omega)$  are approximately computed by using solution  $\{(u_h^k, \phi_h^k)\}_{k=1}^{N_T}$  with  $\{\eta_h^k\}_{k=1}^{N_T}$  of scheme (5.1) as

$$\begin{aligned} E(t^k) &\approx E_h^k : = \int_{\Omega} \frac{\rho}{2} (\phi_h^k) |u_h^k|^2 dx + \int_{\Omega} \frac{\rho g}{2} |\eta_h^k|^2 dx, \\ I_1(t^k; \Gamma) &\approx I_{h1}^k : = -\frac{\rho}{2} \int_{\Gamma} (\phi_h^k) |u_h^k|^2 (u_h^k) \cdot n ds, \\ I_2(t^k; \Gamma) &\approx I_{h2}^k : = -\rho g \int_{\Gamma} (\phi_h^k) (\eta_h^k) (u_h^k) \cdot n ds, \\ I_3(t^k; \Gamma) &\approx I_{h3}^k : = 2\mu \int_{\Gamma} (\phi_h^k) (D(u_h^k) n) \cdot (u_h^k) ds, \\ I_4(t^k; \Omega) &\approx I_{h4}^k : = -2\mu \int_{\Omega} (\phi_h^k) |D(u_h^k)|^2 dx. \end{aligned}$$

Numerical simulations for the problem (3.1)-(3.5) with the same setting described in Subsection 4.1.3 except  $\Delta t$ . Here we set  $\Delta t = 2h$ ,  $h = 0.007, 0.0047, 0.0035$  and  $0.0028$ , where  $h$  is the maximum edge length of the triangle element. The results are presented in Figures 5.2, 5.3 and 5.4, where (i)-(v) in the figures represent the cases (i)-(v) described at the beginning of this section 4.1. The graphs of  $E_h^k$  and  $\sum_{i=1}^4 I_{hi}^k$  versus  $t = t^k$  ( $k \in \mathbb{N}$ ) are presented in the Figure 5.2 and Figure 5.3, respectively. There are four lines in each figure, but the lines are almost overlapped in the cases of (ii)-(v). In the case of (i) the graphs are qualitatively similar. The Figure 5.4 show the graphs of  $I_{hi}^k$ ,  $i = 1, \dots, 4$  versus  $t = t^k$  ( $k \in \mathbb{N}$ ) for  $dt = 0.0056$  and  $dx = 0.0028$ .

From the numerical results presented in Figure 5.2, it can be found that the total energy is mainly decreasing with respect to time. In the case of (i), i.e.,  $\Gamma = \Gamma_D$ , we can see that the graphs are increasing in the Figure 5.2, while the values are small. We think this is because of numerical truncation error. But it can be seen that as the number of points in

computation increases, the results seem to converge to a stable state. From the Figure 5.3 it can be clearly seen that the sum  $\sum_{i=1}^4 I_{hi}^k$  corresponding to the derivative of the total energy is always non-positive, which confirms the stability of solutions to the model numerically.

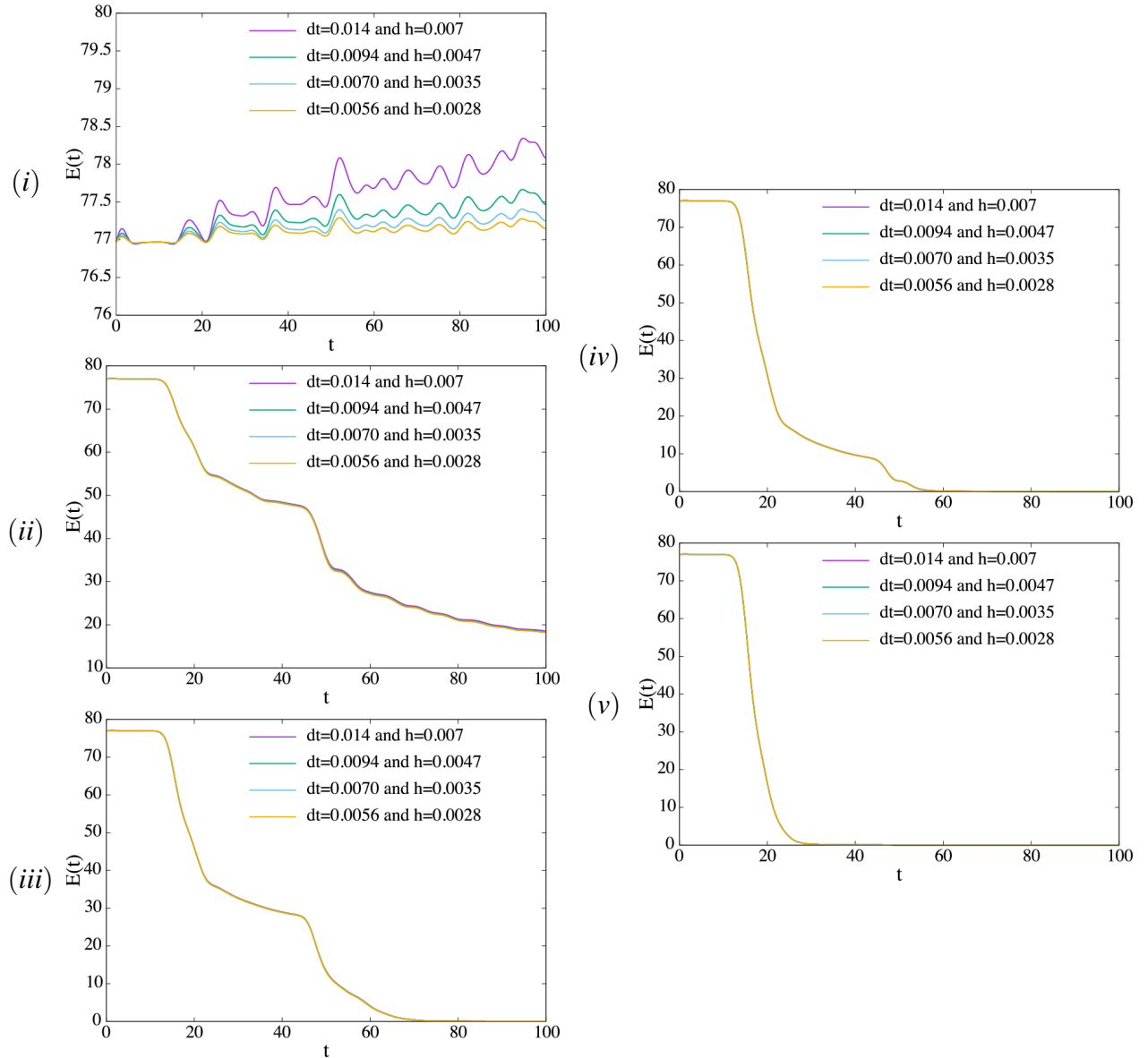


Fig. 5.2 Graphs of  $E_h^k$  versus  $t = t^k$  ( $\geq 0, k \in \mathbb{Z}$ ) for the five cases (i)-(v).

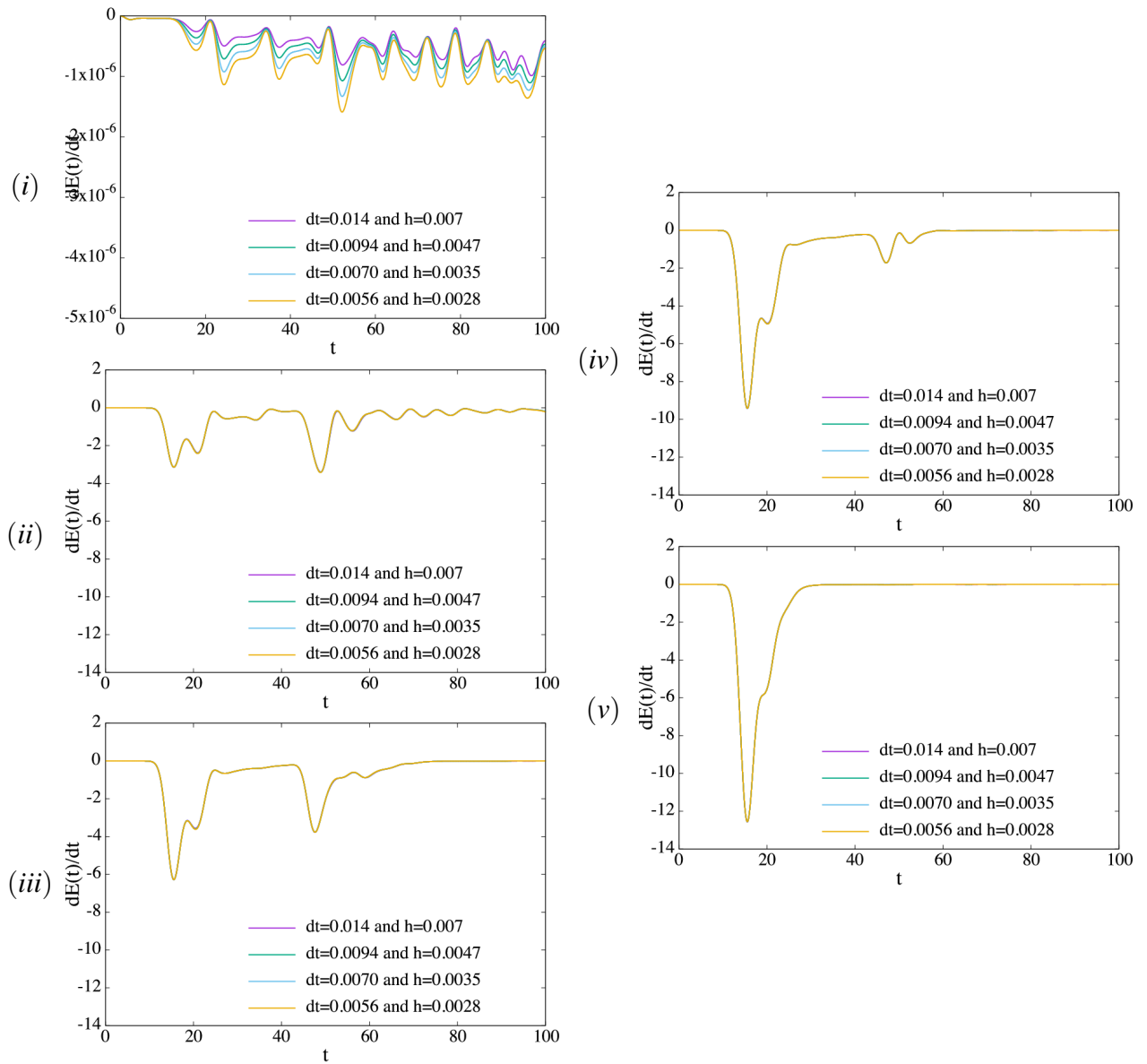


Fig. 5.3 Graphs of  $\sum_{i=1}^4 I_{hi}^k \approx \frac{d}{dt} E(t)$  versus  $t = t^k (\geq 0, k \in \mathbb{Z})$  for the five cases (i)-(v).

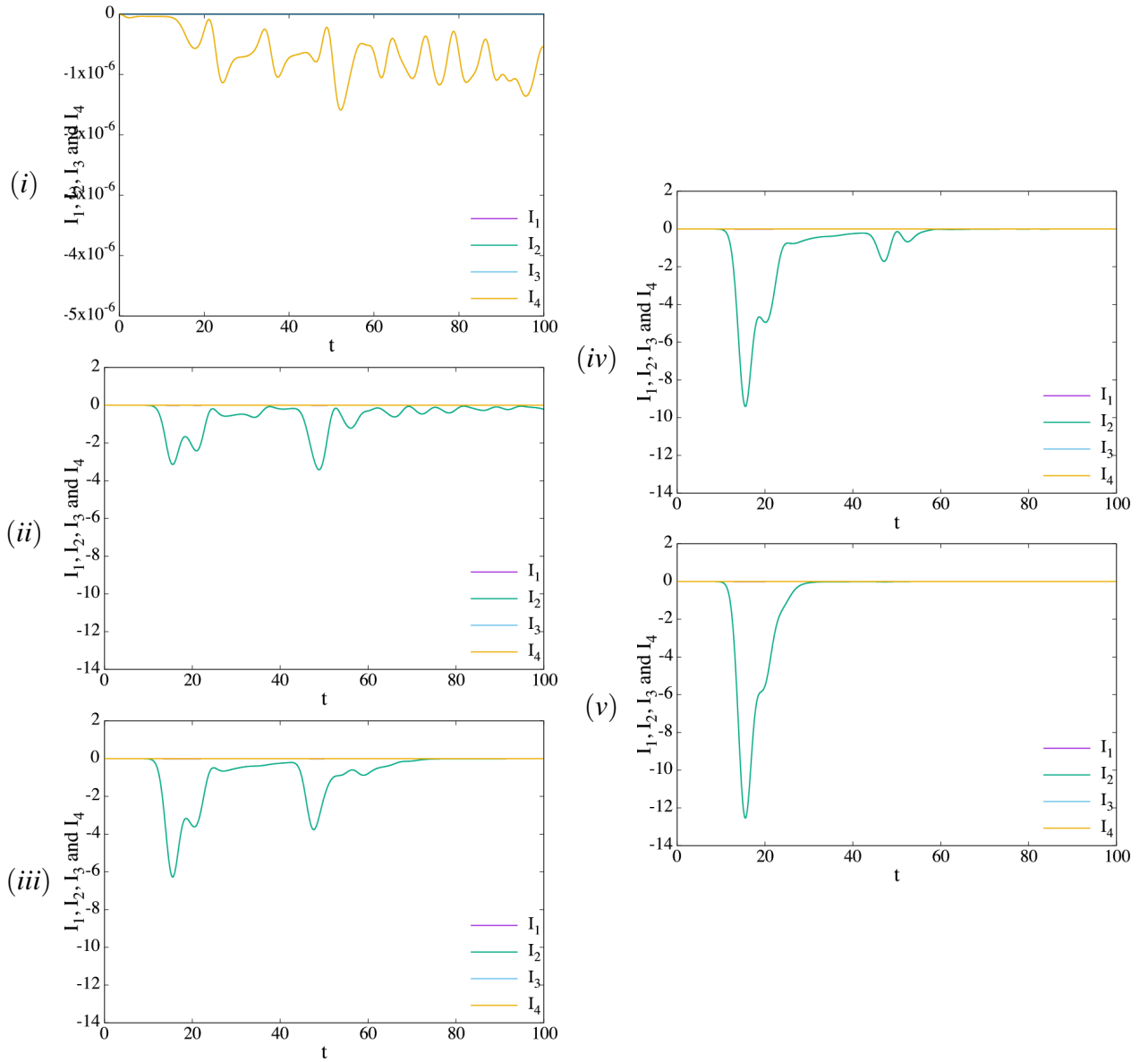


Fig. 5.4 Graphs of  $I_{hi}^k, i = 1, \dots, 4$  versus  $t = t^k (\geq 0, k \in \mathbb{Z})$  for the five cases (i)-(v).

### 5.1.3 The experimental order of convergence of the LG scheme

In this section, the experimental order of convergence of the LG scheme for the five cases (i)-(v) are investigated with several norms. For this purpose, we set  $\Omega = (0, 1)^2$ ,  $g = \mu = \rho = \zeta = 1$ . The exact solutions are considered as follows:

$$\phi = 1 + \sin \pi x_1 \sin \pi x_2 (2 + \sin \pi t) / 8,$$

$$\mathbf{u} = \begin{bmatrix} 1 \\ 1 \end{bmatrix} \sin \pi x_1 \sin \pi x_2 (2 + \sin \pi t) / 3.$$

$N (= 32, 64, 128, 256, 512)$  is considered as the number of divisions on each side of the boundary of the square domain  $\Omega$ .  $T = 1$  is considered.  $\Delta t = h/2$  is taken for all cases. The relative errors  $\frac{\|M_h - \Pi_h M\|_X}{\|\Pi_h M\|_X}$  were calculated for  $M = \phi, \mathbf{u}$ , where  $X = l^\infty(L^2), l^\infty(H_0^1), l^\infty(H^1), l^2(L^2), l^2(H_0^1)$  and  $l^2(H^1)$ . Also  $\|M_h^n\|_{l^\infty(Y)} = \max_{1 \leq n \leq N_T} \|M_h^n\|_Y$  and  $\|M_h^n\|_{l^2(Y)} = \sqrt{\Delta t \sum_{n=1}^{N_T} \|M_h^n\|_Y^2}$  ( $Y = L^2, H_0^1, H^1$ ). Here  $\Pi_h$  is a Lagrange interpolation operator and  $h$  is the maximum edge length of the triangle element. The results for the experimental order of convergence of the LG scheme are presented in the Figures 5.5– 5.10. The results show that the experimental order of convergence of  $u_1$  and  $u_2$  is  $O(h)$  for all the six norms and experimental order of convergence of  $\eta$  is  $O(h)$  for the norms  $l^\infty - L^2$  and  $l^2 - L^2$  and for the other four norms experimental order of convergence is not  $O(h)$  but confirmed to be convergent.

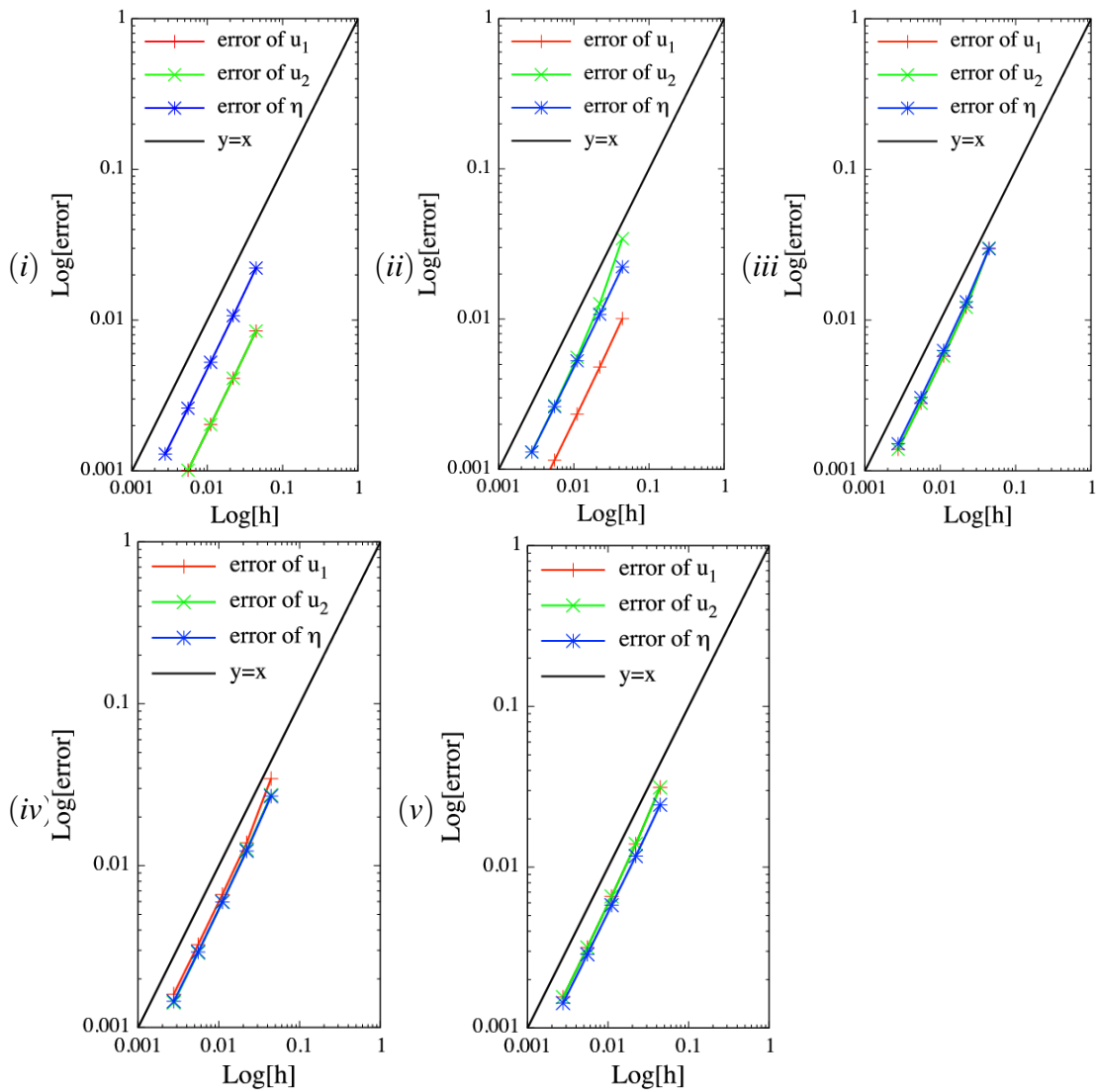


Fig. 5.5 Graphs of experimental relative errors in log scale with the norm  $l^\infty (L^2)$  for the five cases (i)-(v).

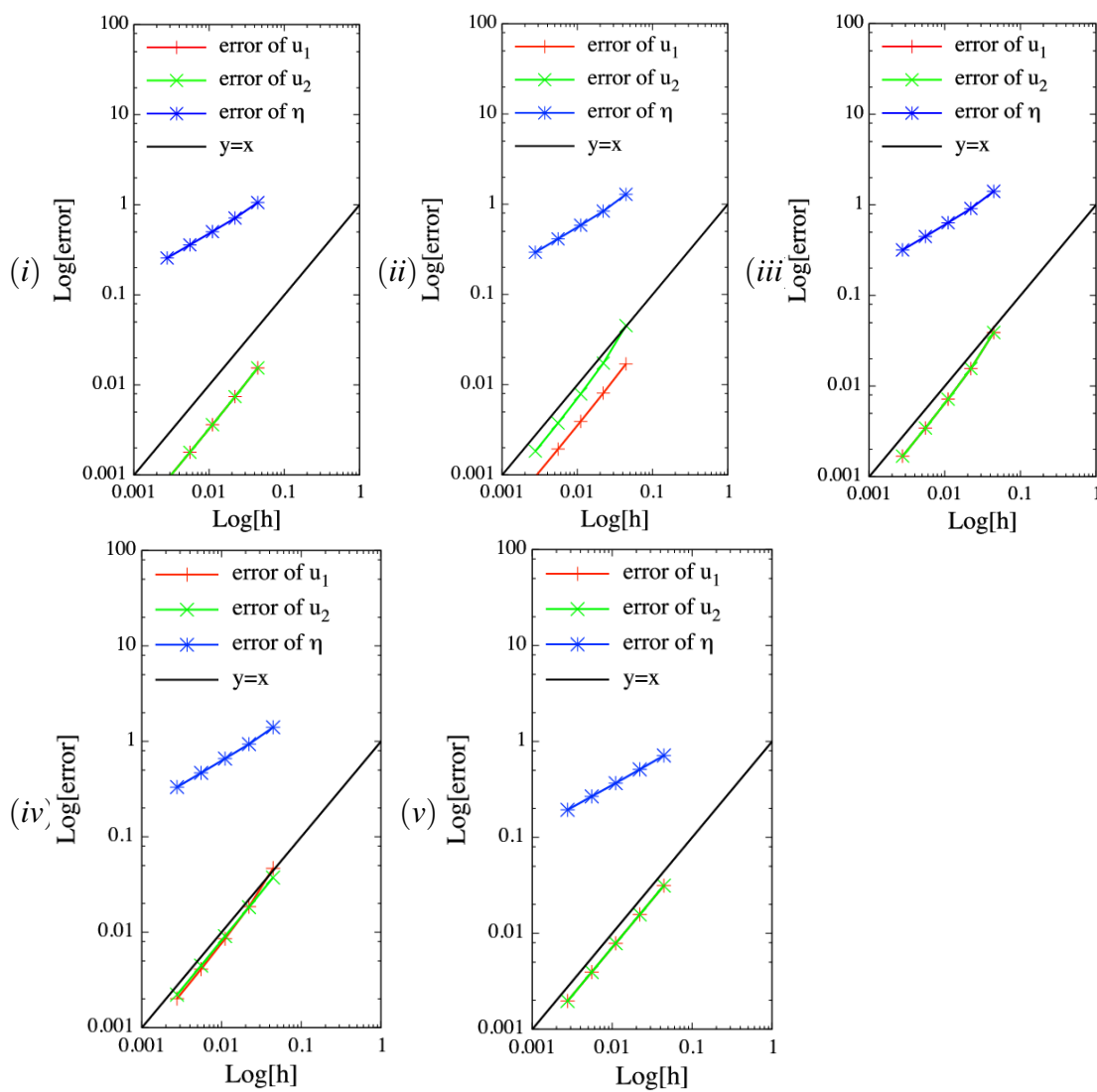


Fig. 5.6 Graphs of experimental relative errors in log scale with the norm  $l^\infty(H_0^1)$  for the five cases (i)-(v).

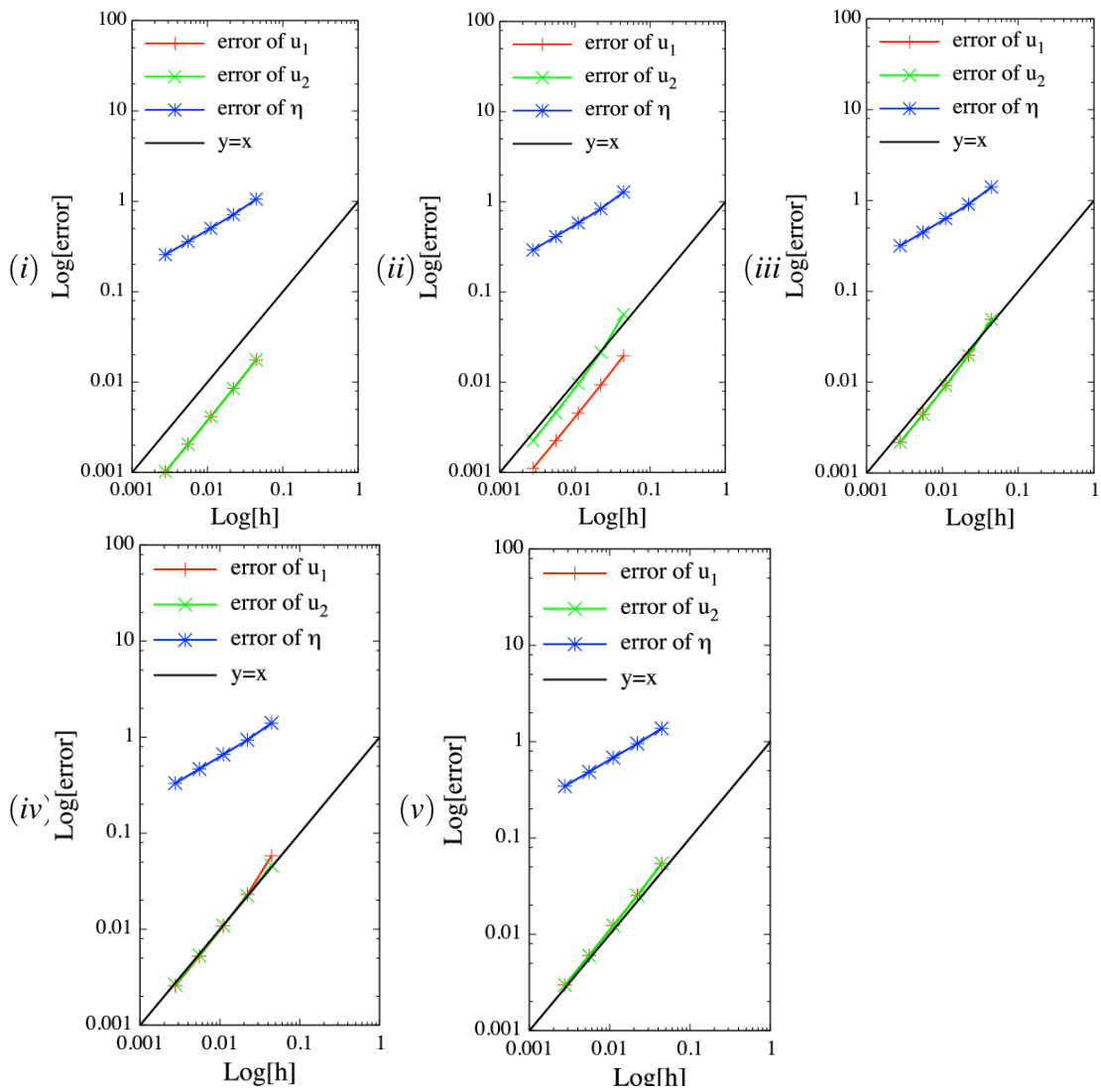


Fig. 5.7 Graphs of experimental relative errors in log scale with the norm  $l^\infty(H^1)$  for the five cases (i)-(v).

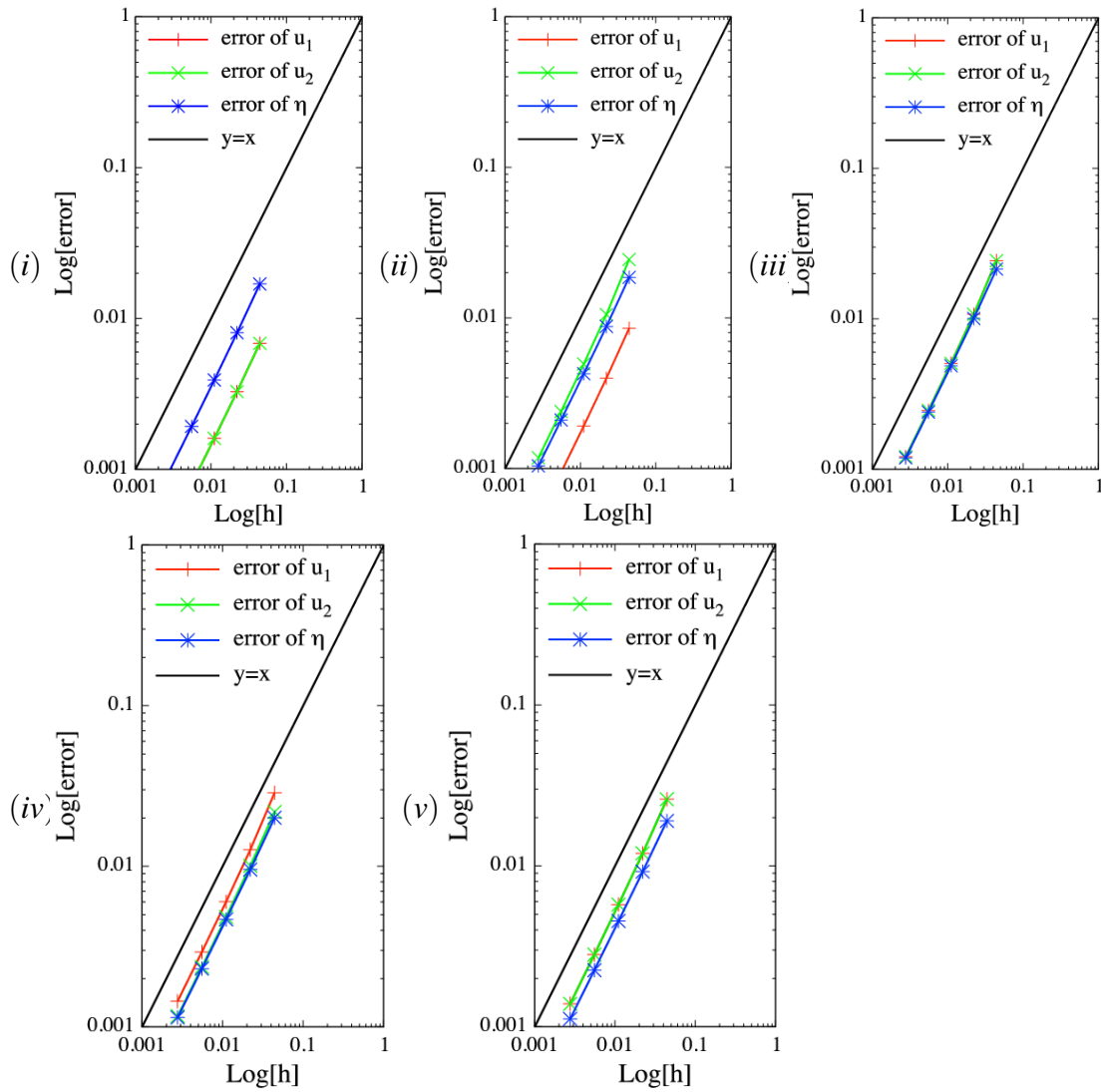


Fig. 5.8 Graphs of experimental relative errors in log scale with the norm  $l^2(L^2)$  for the five cases (i)-(v).

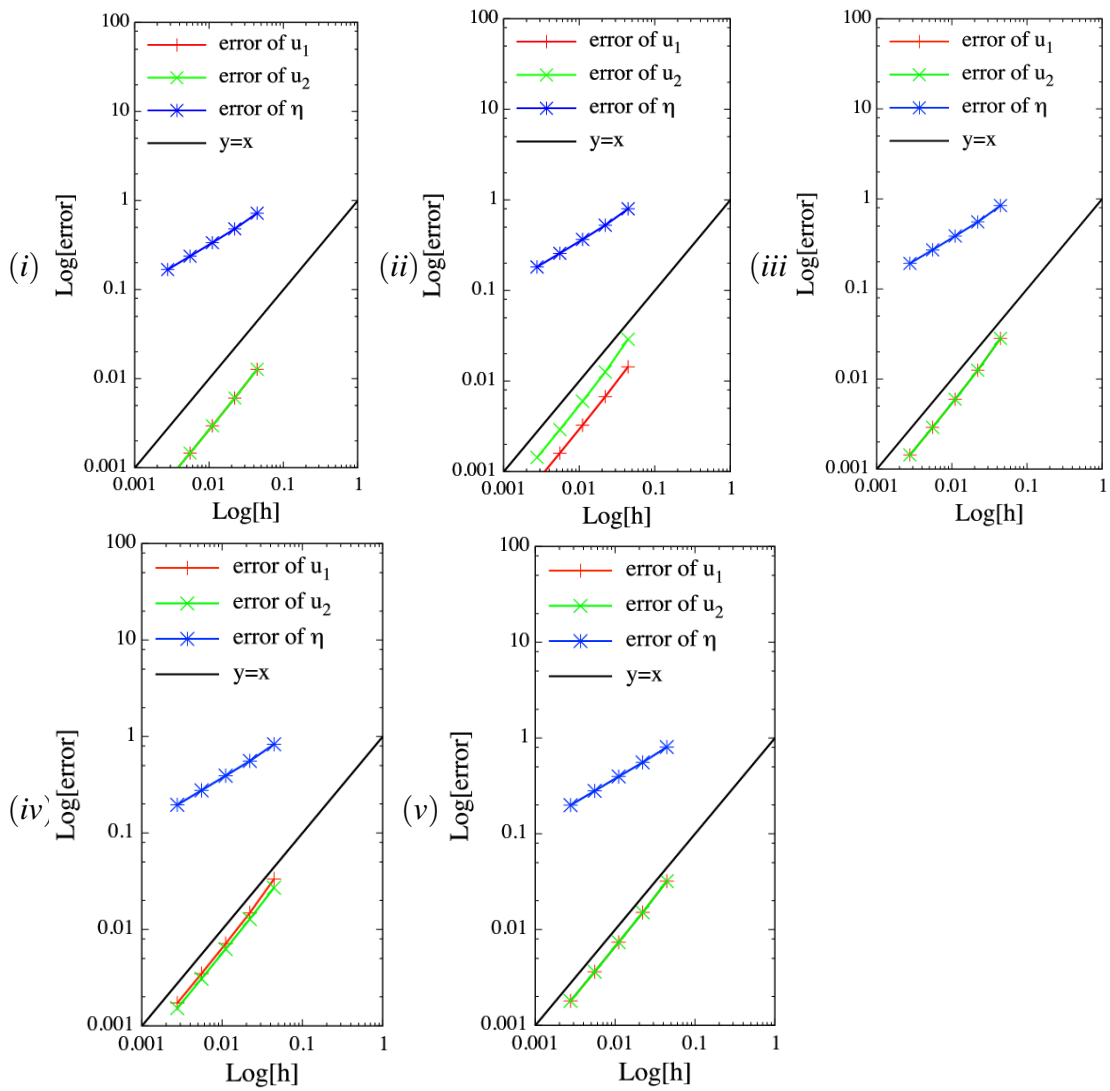


Fig. 5.9 Graphs of experimental relative errors in log scale with the norm  $l^2(H_0^1)$  for the five cases (i)-(v).

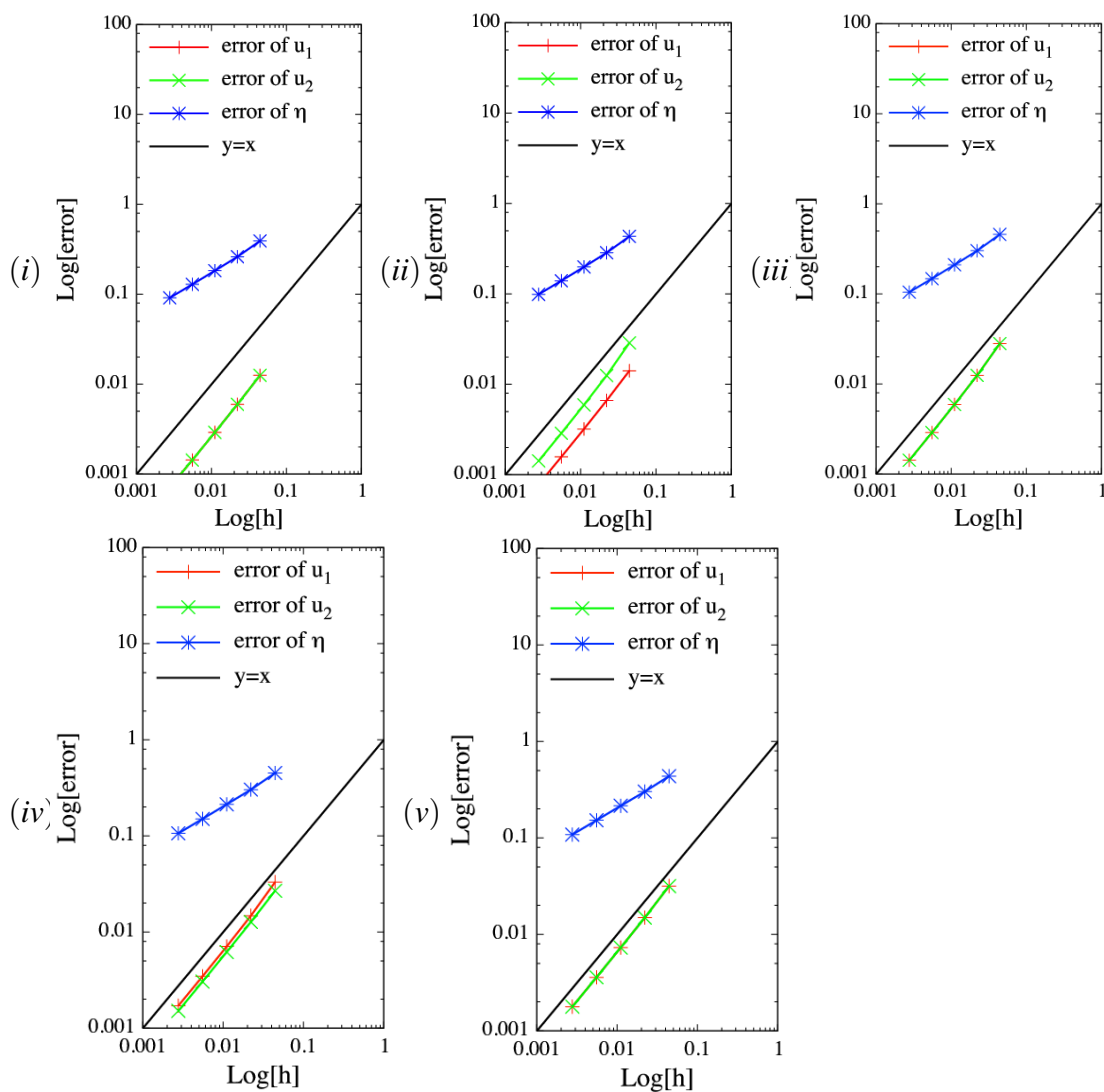


Fig. 5.10 Graphs of experimental relative errors in log scale with the norm  $l^2(H^1)$  for the five cases (i)-(v).

## 5.2 Numerical results for the Bay of Bengal

In this section, for more realistic simulation, we have shown results for the numerical simulation in the Bay of Bengal by the LG scheme presented in the Section 5.1. For the numerical treatment, firstly we have simplified the domain presented in the Figure 1.1 and prepare triangular mesh as in Figure 1.4 by using FreeFem++. Figure 5.11 gives an idea of our simulation setting. Let the domain presented in the Figure 5.11 be  $\Omega$ . It is to be noted here that in the horizontal direction, the domain is extended from 0 km to 1051.4 km and in the vertical direction, it is extended from 0 km to 889.59 km. We have imposed two types of boundary conditions, the zero Dirichlet boundary condition on  $\Gamma_D$  and the transmission boundary condition on  $\Gamma_T$  (See Figure 5.11).  $\Gamma_D$  is set on the coast and  $\Gamma_T$  is set artificially

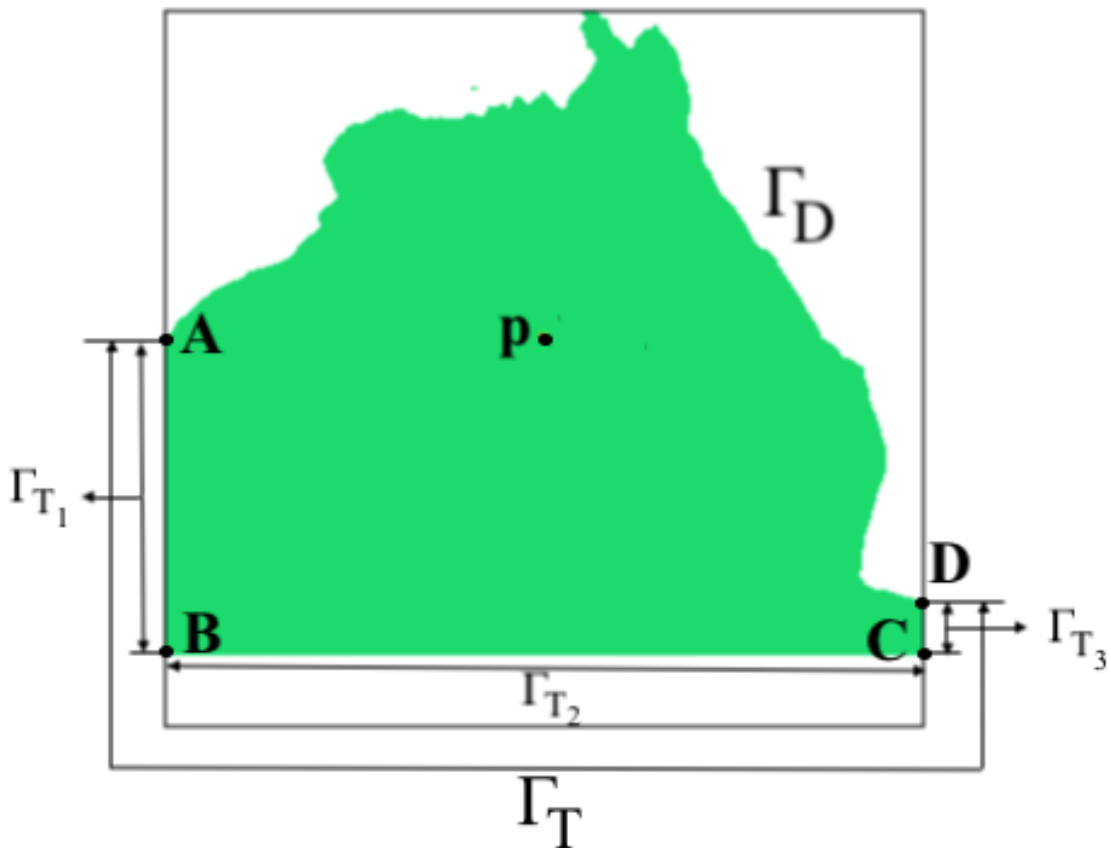


Fig. 5.11 A figure of Bay of Bengal domain showing the setting of the transmission and the Dirichlet boundaries.

in the water. It can be seen from the Figure 5.11 that  $\Gamma_T$  consists of three parts  $AB = \Gamma_{T_1}$ ,  $BC = \Gamma_{T_2}$  and  $CD = \Gamma_{T_3}$ . We set an initial elevation  $\eta^0 = 0.05 \exp(-0.1|x - p|^2)$  at the point  $p$ , where  $p$  is the nearest nodal point from  $(525, 440)$ . Then a numerical simulation is done considering  $\zeta = 2.0$ ,  $\mu = 1$ ,  $g = 9.8 \times 10^{-3}$ ,  $\rho = 10^{12}$ ,  $h = 1.408044$  until  $T = 5000$ . The results at  $t = 0s$ ,  $2800s$ ,  $3120s$ ,  $3240s$ ,  $3740s$ ,  $3940s$  and  $4660s$  are presented in the left figures of the Figures 5.13 and 5.14. From the left figures of the Figures 5.13 and 5.14 it can be seen that a circular wave is created at around the centre which propagates towards the boundary with respect to time. A reflection is found when the wave touches  $\Gamma_D$  but no remarkable reflection is found when the wave touches  $\Gamma_T$ . It seems that the wave passes through  $\Gamma_T$ .

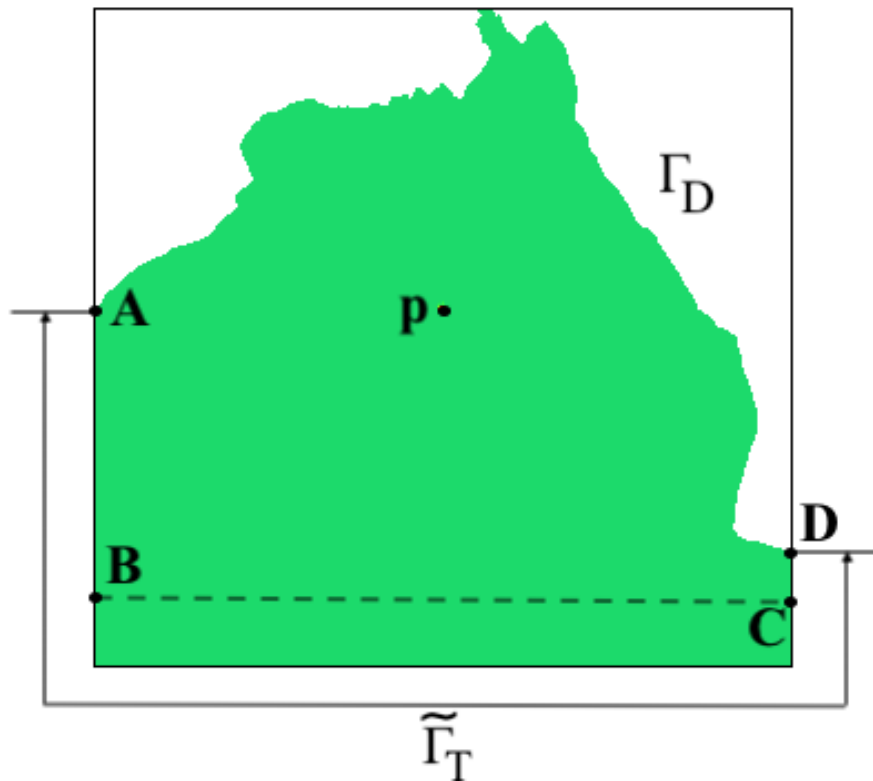


Fig. 5.12 A figure of extended domain showing the setting of the transmission and the Dirichlet boundaries.

We are also interested to see what happens if we slightly change the position of the transmission boundary. For this purpose, we have prepared another domain say  $\tilde{\Omega}$  extending

$\Omega$  by 100 km in the negative vertical direction ( see Figure 5.12). Thus in the horizontal direction, the domain  $\tilde{\Omega}$  is extended from 0 km to 1051.4 km and in the vertical direction, it is extended from  $-100$  km to 889.59 km. Here  $\Omega \subset \tilde{\Omega}$  and the Dirichlet boundary  $\Gamma_D$  is the same for both  $\Omega$  and  $\tilde{\Omega}$ . Let the transmission boundary for  $\tilde{\Omega}$  be  $\tilde{\Gamma}_T$ . A numerical simulation is done in  $\tilde{\Omega}$  considering the same values of parameters used for the domain  $\Omega$ . The results at  $t = 0s, 2800s, 3120s, 3240s, 3740s, 3940s$  and  $4660s$  are presented in the right figures of the Figures 5.13 and 5.14, which show similar results as in  $\Omega$ . From the both left and right figures of the Figures 5.13 and 5.14, it can be seen that the transmission boundary condition works well numerically.

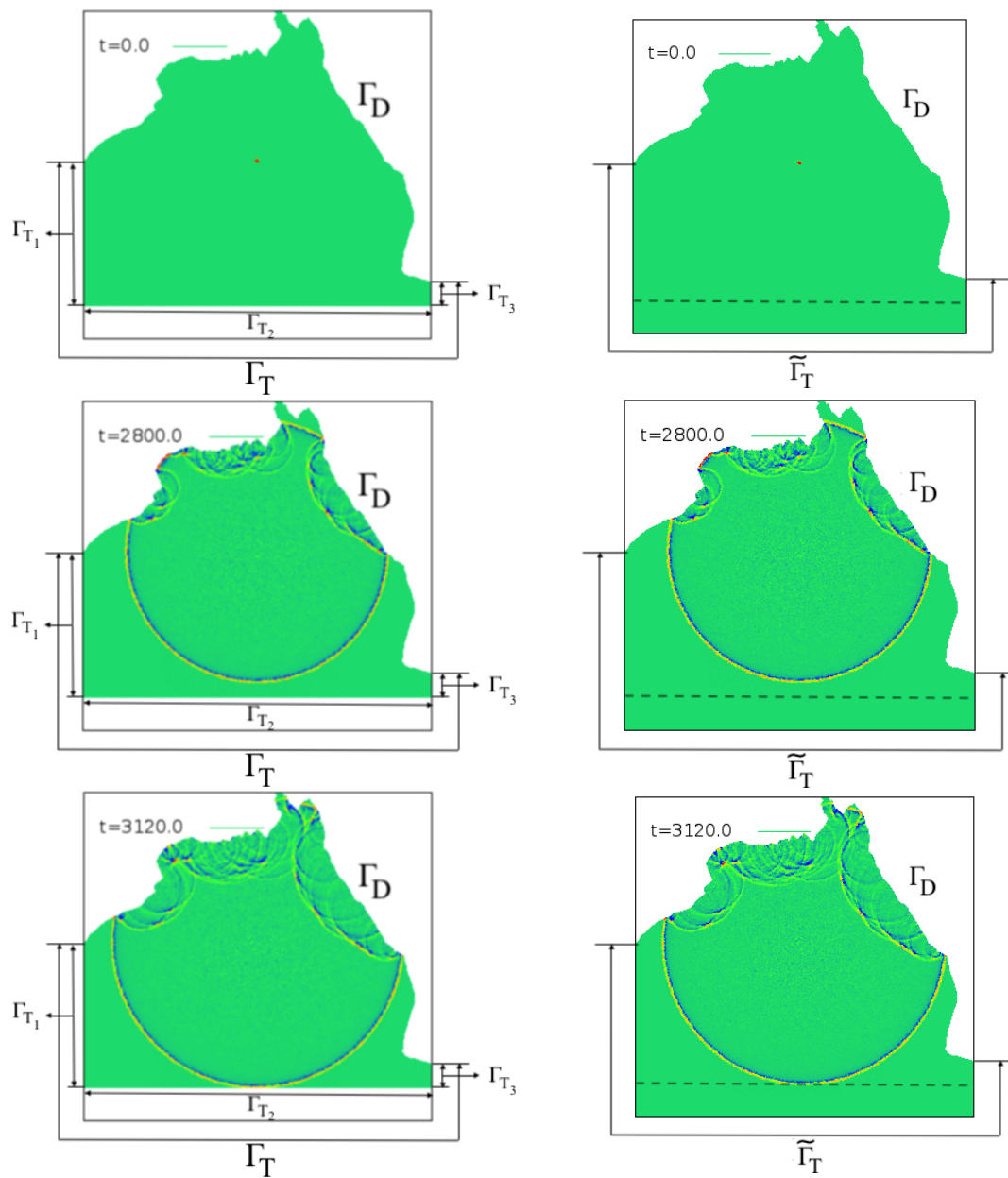
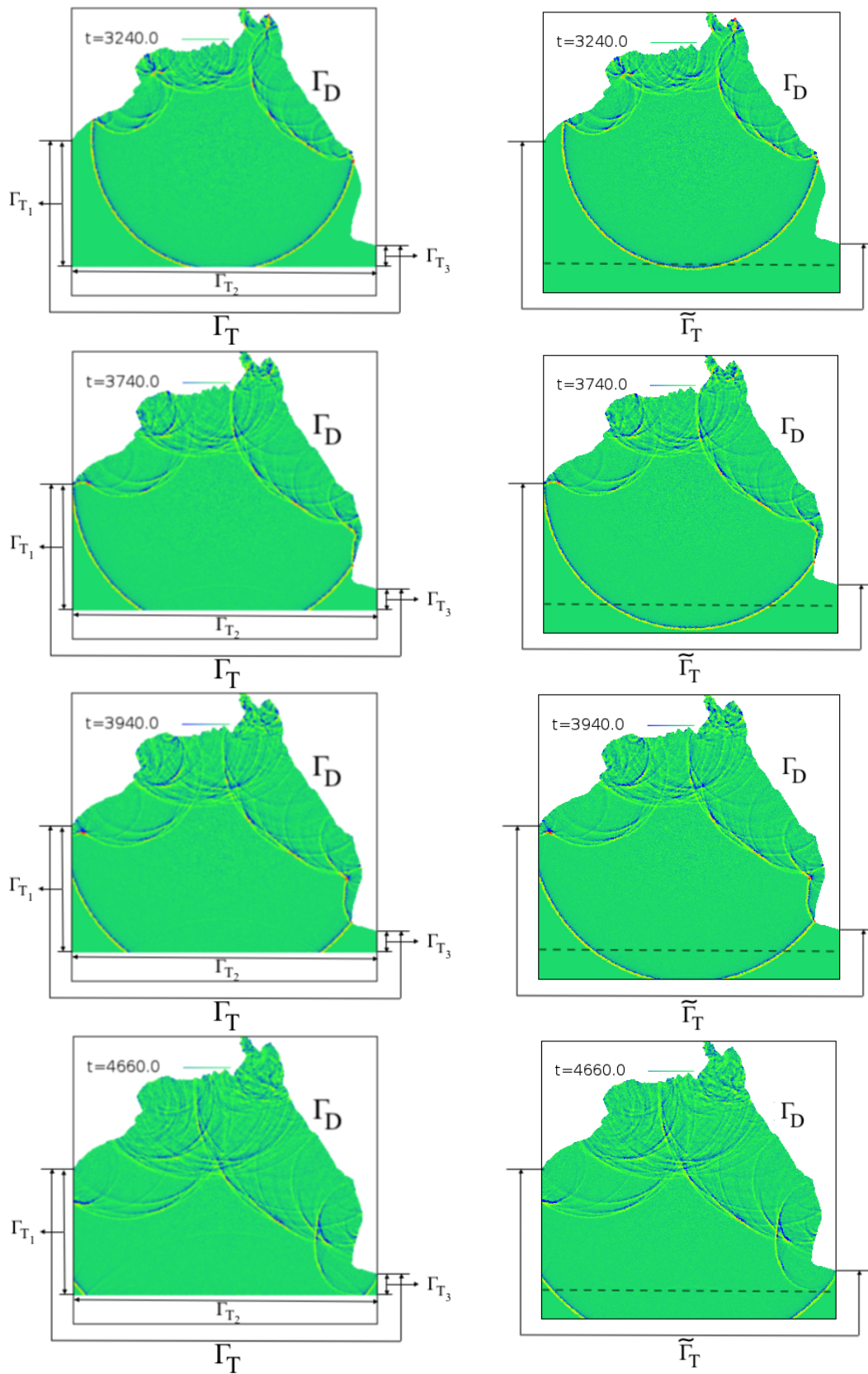


Fig. 5.13 Simulation in the Bay of Bengal at time  $t = 0s$ ,  $2800s$  and  $3120s$ .

Fig. 5.14 Simulation in the Bay of Bengal at time  $t = 3240s$ ,  $3740s$ ,  $3940s$  and  $4660s$ .

### 5.2.1 Computation of mass and $L^2$ norm for the Bay of Bengal

We have computed the mass

$$M(t) := \int_{\Omega} \eta(x,t) dx \approx \int_{\Omega} (\Pi \eta_h^k) dx =: M_h^k$$

at  $t = t^k$  ( $\geq 0, k \in \mathbb{Z}$ ) for common part of  $\Omega$  and  $\tilde{\Omega}$ . It is to be noted here that  $AB$ ,  $BC$  and  $CD$  are transmission boundaries for the the domain  $\Omega$  but  $BC$  lies inside the domain  $\tilde{\Omega}$  (see Figures 5.11 and 5.12). The results are shown in the Figure 5.15.

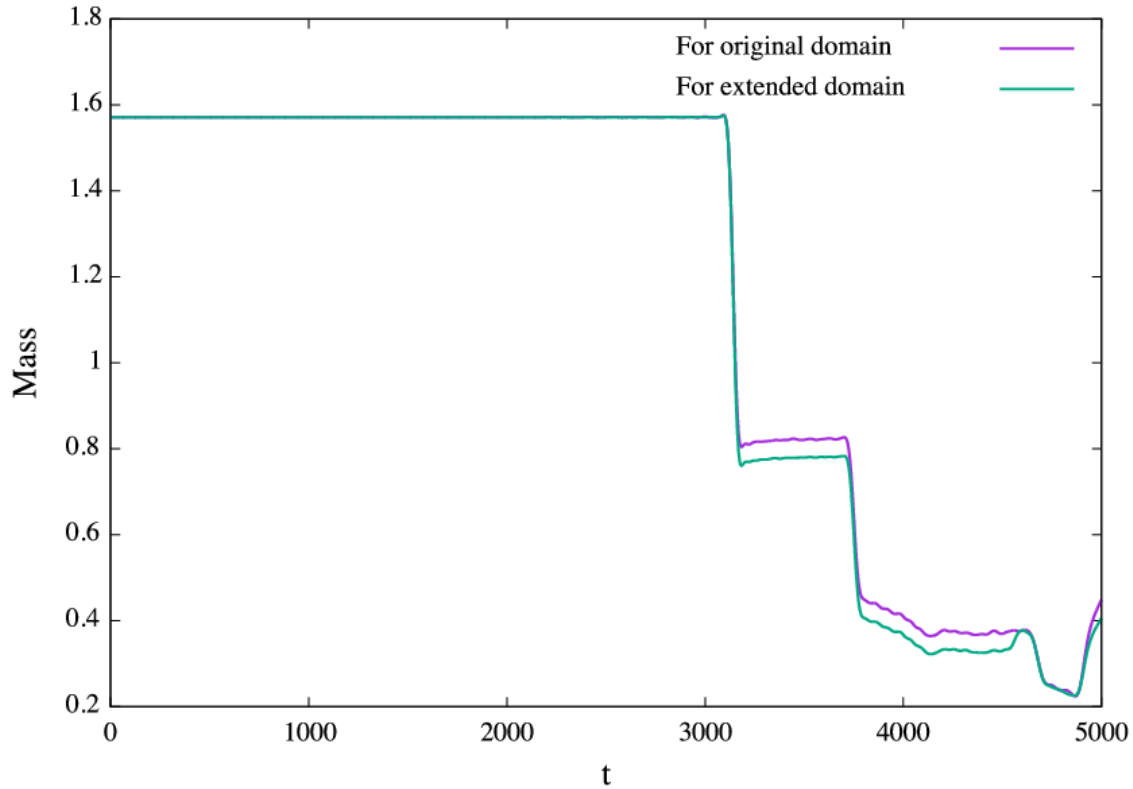


Fig. 5.15 Graphs of  $M_h^k$  versus  $t = t^k$  ( $\geq 0, k \in \mathbb{Z}$ ) for the common part of the domains  $\Omega$  and  $\tilde{\Omega}$ .

The derivative of mass can be computes as follows.

$$\begin{aligned}
M'(t) &= \int_{\Omega} \frac{\partial \eta}{\partial t}(x,t) dx \\
&= \int_{\Omega} \frac{\partial \phi}{\partial t}(x,t) dx \text{ (from the third equation of (3.1) and } \zeta = \text{constant)} \\
&= - \int_{\Omega} \nabla \cdot (\phi u) dx \text{ (from the first equation of (3.1))} \\
&= - \int_{\partial \Omega} (u \cdot n) \phi ds = - \int_{\Gamma_D \cup \Gamma_S \cup \Gamma_T} (u \cdot n) \phi ds = - \int_{\Gamma_T} (u \cdot n) \phi ds \\
&= - \int_{\Gamma_T} c \eta ds \text{ (from the equation (3.4), here } c \text{ is a constant)}.
\end{aligned}$$

Therefore the behaviour of the graph of mass is dependent on the sign of  $\eta$  on  $\Gamma_T$ . It is clear that if  $\eta > 0$  on  $\Gamma_T$  then we have decay of mass, on the other hand if  $\eta < 0$  on  $\Gamma_T$  then mass will increase. Thus we have presented the graph of  $\eta$  on  $AB$ ,  $BC$  and  $CD$  for both the domains  $\Omega$  and  $\tilde{\Omega}$  in the Figures 5.16 and 5.17 to have a clear understanding of the behaviour of the graphs of mass presented in the Figure 5.15. In the Figures 5.13, 5.14, and 5.16, 5.17, the results are presented at  $t = 0s, 2800s, 3120s, 3240s, 3740s, 3940s$  and  $4660s$ . From the Figure 5.15, until around  $3100s$  there is no decay of mass, after that there is a drastic decay of mass, this is because the wave touches the transmission boundary  $\Gamma_{T_2}$  (see Figures 5.13 for  $t = 3120s$ ). From the the Figure 5.16, it can be seen that the sign of  $\eta$  is positive on  $\Gamma_T$  at  $t = 3120s$ . Around  $t = 3200s-3700s$  mass remains a kind of stable, this is because of the cancellation of the values of  $\eta$  on  $\Gamma_T$  (see Figures 5.17 for  $t = 3240s$ ). After  $t = 3700s$  there is another drastic decay of mass, this is because the wave touches the transmission boundary  $\Gamma_{T_1}$  (see Figures 5.14 for  $t = 3740s$ ). From the the Figure 5.17, it can be seen that the sign of  $\eta$  is positive on  $\Gamma_T$  at  $t = 3740s$ . Around  $t = 3800s-4650s$  mass has slow decay, because the sign of  $\eta$  is positive on  $\Gamma_T$  in this time (see Figure 5.17 at  $t = 3940s$ ). After  $t = 4650s$  there is another drastic decay of mass, this is because the wave touches the

transmission boundary  $\Gamma_T$  (see Figures 5.14 for  $t = 4660s$ ). From the the Figure 5.17, it can be seen that the sign of  $\eta$  is positive on  $\Gamma_T$  at  $t = 4660s$ . It is to be noted here that in our computation, there is still a little bit artificial reflection on the transmission boundary. For this reason, the difference of mass can be found in Figure 5.15 for the two different cases.

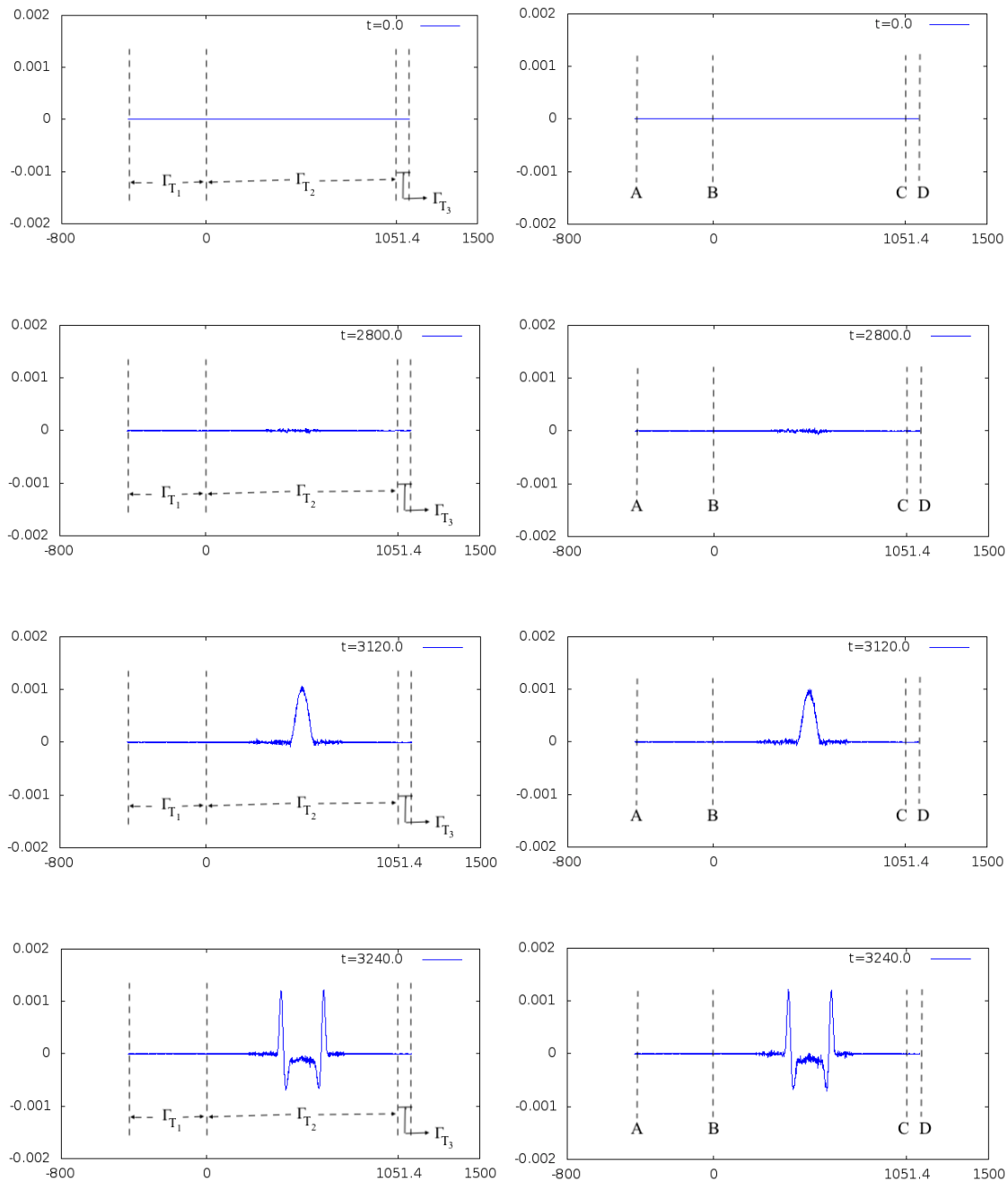


Fig. 5.16 Graph of  $\eta$  on  $AB, BC$  and  $CD$  for both  $\Omega$  and  $\tilde{\Omega}$  at time  $t = 0s, 2800s$  and  $3120s$ .

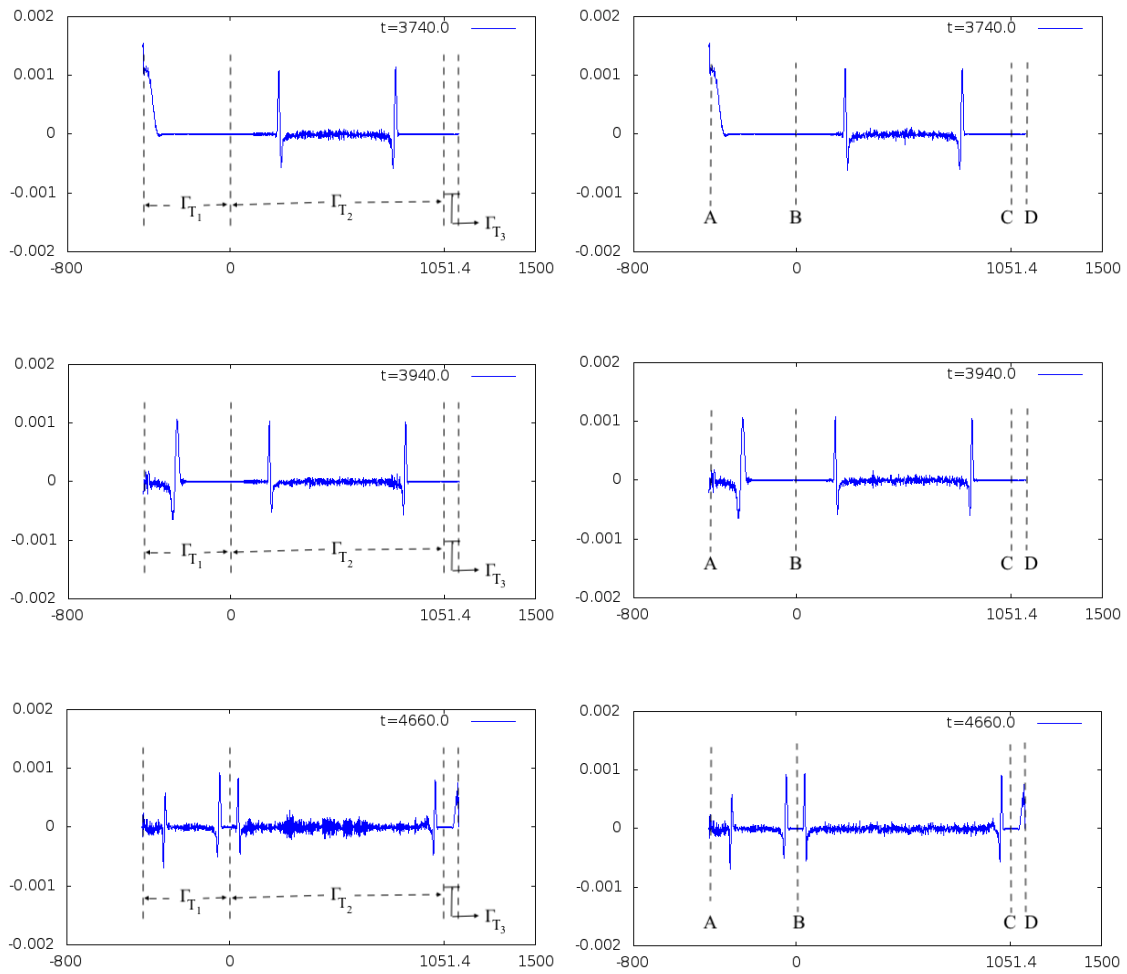


Fig. 5.17 Graph of  $\eta$  on  $AB$ ,  $BC$  and  $CD$  for both  $\Omega$  and  $\tilde{\Omega}$  at time  $t = 3240s$ ,  $3740s$ ,  $3940s$  and  $4660s$ .

We have also computed the  $L^2$  norm of  $\eta$

$$\|\eta(t)\|_{L^2} := \sqrt{\int_{\Omega} |\eta(x,t)|^2 dx} \approx \sqrt{\int_{\Omega} |\Pi\eta_h^k|^2 dx} =: \|\eta_h^k\|_{L^2}$$

at  $t = t^k$  ( $\geq 0, k \in \mathbb{Z}$ ) for common part of  $\Omega$  and  $\tilde{\Omega}$ . The results are presented in the Figure 5.18, which show that the norms are almost same for both the cases.

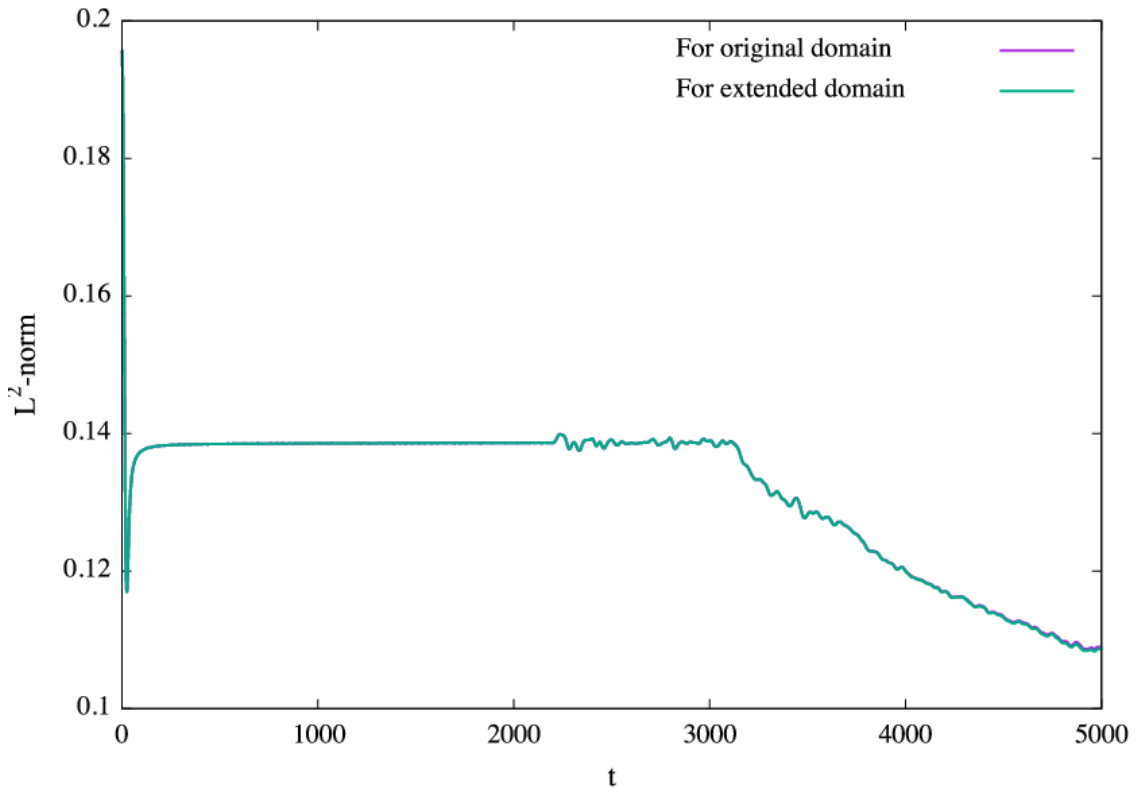


Fig. 5.18  $\|\eta_h^k\|_{L^2}$  versus  $t = t^k$  ( $\geq 0, k \in \mathbb{Z}$ ) for the common part of the domains  $\Omega$  and  $\tilde{\Omega}$ .

From the Figures 5.13, 5.14, 5.15, 5.16, 5.17 and 5.18, we can conclude that the transmission boundary condition works well numerically. If the transmission boundary shifted slightly, the results remains almost the same and the error may be around 5% in the simulation presented in this chapter.

# Chapter 6

## Instability on the transmission boundary and some future works

### 6.1 Instability on the transmission boundary

For long time simulation in the Bay of Bengal for the case  $\Omega$  (see 5.2) we have some instability (see Figures 6.1 and 6.2 ). To resolve this instability is a future work. It is to be noted here that a boundary data for  $\phi$  is necessary on the so-called inflow boundary, where  $u \cdot n < 0$  is satisfied for the outward unit normal vector  $n$ . On the transmission boundary  $\Gamma_T$ , the boundary condition for  $\phi$  is required for the case of inflow. In such case we have used one sided difference for the computation in FDM. It is to be noted here that the position  $x - u^k(x)\Delta t$  is the so-called upwind point of  $x$  with respect to  $u^k$ . For the computation in LGM, the “nearest” boundary value of  $\phi^k$  is used if the upwind point places outside the domain. So there is a hidden boundary condition for  $\phi$  in the case of inflow. We think the instability occurred due to this hidden boundary condition.

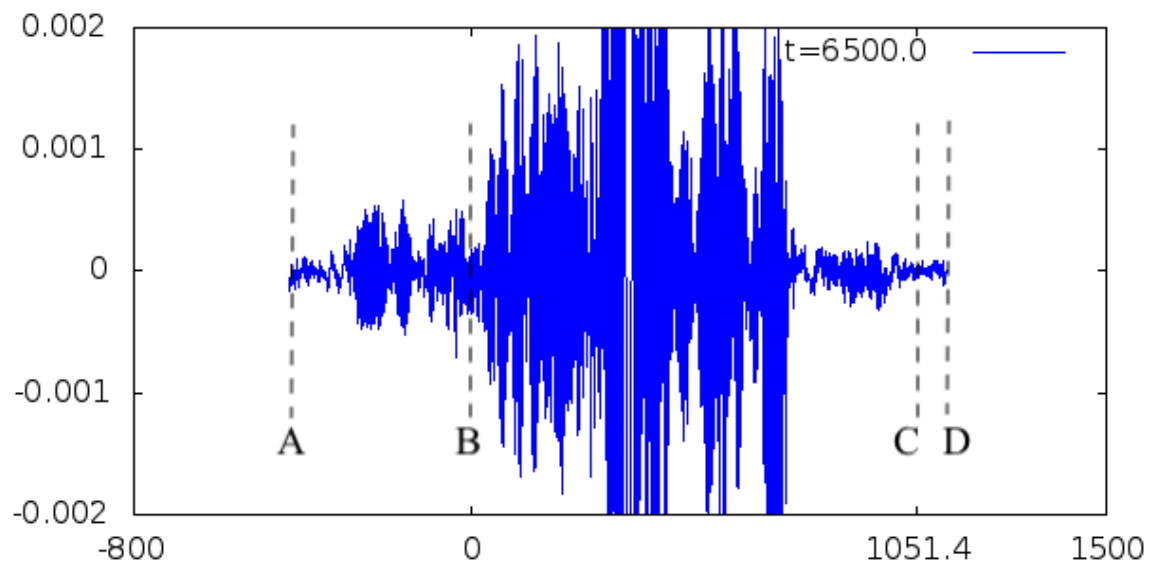


Fig. 6.1 Graph of  $\eta$  on  $AB$ ,  $BC$  and  $CD$  for both  $\Omega$  and  $\tilde{\Omega}$  at time  $t = 6500s$ .

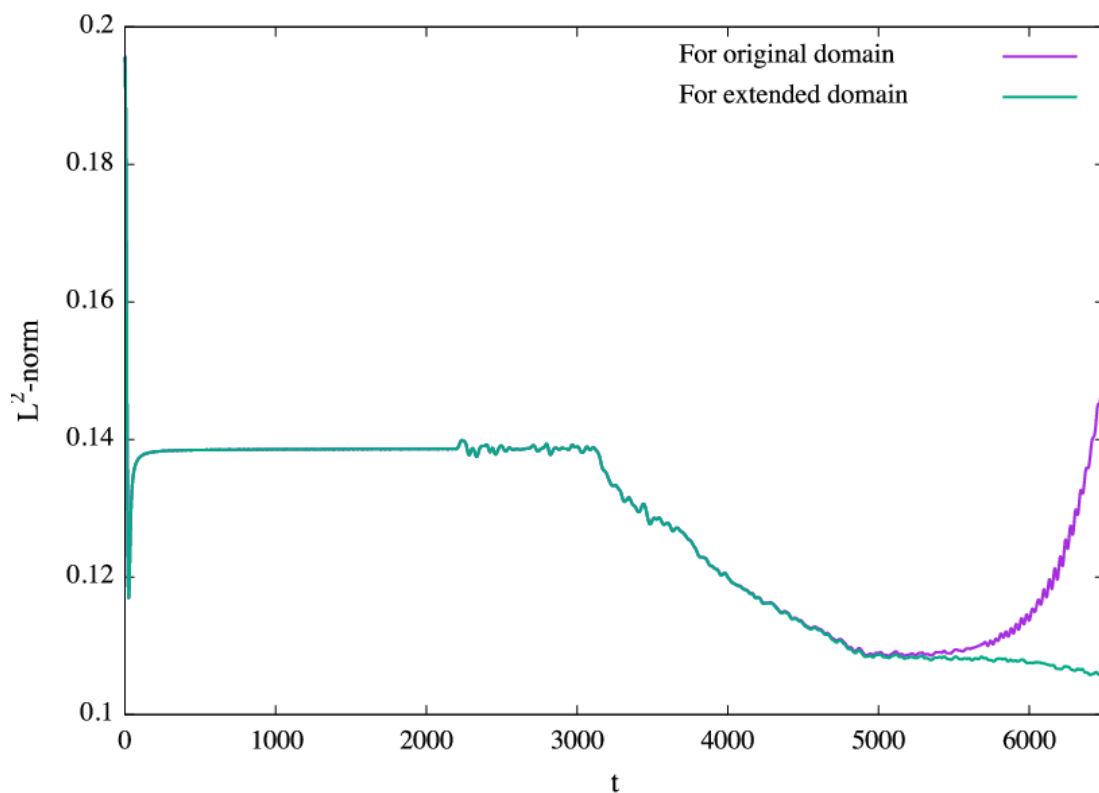


Fig. 6.2  $L^2$  norm of  $\eta$  for the two cases of transmission boundary setting described in the Section 5.2

## **6.2 Some future works**

1. Study of the existence, uniqueness and stability of the solutions of the SWEs with a transmission boundary condition.
2. Study of searching the hidden boundary condition in the case of inflow on the transmission boundary.
3. Inclusion of wind stress, bottom friction, Coriolis force, bathymetry, islands and river dynamics for developing a storm surge prediction model for the Bay of Bengal.



# Chapter 7

## Conclusion

The stability of SWEs with a transmission boundary condition has been studied theoretically and numerically using a suitable energy. For a suitable energy, we have obtained an equality that the time-derivative of the energy is equal to a sum of three line integrals and a domain integral in Theorem 3.2.1. The theorem implies a (successful) energy estimate of the SWEs with the Dirichlet and the slip boundary conditions, cf. Corollary 3.2.3-(ii). After that, an inequality for the energy estimate of the SWEs with the transmission boundary condition has been proved in Theorem 3.2.4. In the proof, it has been shown that a sum of two line integrals over the transmission boundary is non-positive under some conditions to be satisfied in practical computation.

Based on the theoretical results, the energy estimate of SWEs with the transmission boundary condition has been confirmed numerically by both FDM and LGM.

From the numerical results presented in Figure 4.2, it can be found that the total energy is mainly decreasing with respect to time. In the case of (i), i.e.,  $\Gamma = \Gamma_D$ , we can see that at the early period the graphs are increasing, while the values are small. From the Figure 4.3, it can be clearly seen that the sum  $\sum_{i=1}^4 I_{hi}^k$  corresponding to the derivative of the total energy is always non-positive, which confirms the stability of solutions to the model numerically. From Figure 4.4 and Table 4.1, it can be observed that the value of  $I_{h2}$  is dominating negatively over  $I_{h1}$  and  $I_{h3}$  so that the sum  $\sum_{i=1}^4 I_{hi}$  becomes non-positive always. It is found that the

transmission boundary condition works well numerically and that the transmission boundary condition reduces the energy drastically via the term  $I_{h2}^k$ .

The choice of a positive constant  $c_0$  used in the transmission boundary condition has been investigated additionally by a FDM. Since the artificial reflection should be removed after the time the wave touches the transmission boundary, we find a value of  $c_0$  which provides the minimum of  $\mathcal{S}_h(c_0)$ . The results are presented in Table 4.2, from where it can be concluded that for the case of zero initial velocity the suitable value of  $c_0$  lies in  $[0.7, 1.0]$  and for the case of nonzero initial velocity we cannot say anything yet.

Then we have presented numerical results by a LGM, which are similar to those by the FDM. The results show that the wave can pass through the transmission boundary ( see Figure 5.1).

The experimental order of convergence for the LGM with a suitable choice of exact solutions for five different cases of boundary setting (see Section 4.1) for the norms  $l^\infty - L^2$ ,  $l^\infty - H_0^1$ ,  $l^\infty - H^1$ ,  $l^2 - L^2$ ,  $l^2 - H_0^1$  and  $l^2 - H^1$  are also presented in the Figures 5.5–5.10. The experimental order of convergence of  $u_1$  and  $u_2$  is  $O(h)$  for all the six norms and experimental order of convergence of  $\eta$  is  $O(h)$  for the norms  $l^\infty - L^2$  and  $l^2 - L^2$  and for the other four norms experimental order of convergence is not  $O(h)$  but confirmed to be convergent (see Figures 5.5–5.10).

Furthermore, for more realistic simulation, we have shown results for the numerical simulation in the Bay of Bengal by the LG scheme presented in the Section 5.1 for two different cases of boundary setting (see Figures 5.13–5.14). From the Figures 5.13 and 5.14 it can be seen that a circular wave is created at around the centre which propagates towards the boundary with respect to time. A reflection is found when the wave touches  $\Gamma_D$  but no remarkable reflection is found when the wave touches  $\Gamma_T$ . It seems that the wave passes through  $\Gamma_T$ . We have computed the mass of  $\eta$  for that two cases and the results show that the transmission boundary condition works well numerically and there is a decay of mass

due to the transmission boundary condition(see Figure 5.15). The  $L^2$  norms of  $\eta$  for two different setting described in the Section 5.2 are presented in Figure 5.18. The result shows the transmission boundary condition is almost independent of its position.

From the Figures 5.13, 5.14, 5.15, 5.16, 5.17 and 5.18, we can conclude that the transmission boundary condition works well numerically and if the transmission boundary shifted slightly, the results remains almost the same.

We believe that the theoretical results presented in this work will be helpful to derive theoretical results of energy estimates of the SWEs with the transmission boundary condition including the terms Coriolis force, surface stress and bottom stress. As far as we know, there is not a single model using LGM for the prediction of storm surge in the Bay of Bengal, therefore we strongly believe that our results will be helpful to develop an appropriate storm surge prediction model using LGM for the Bay of Bengal in the near future.



# References

- [1] Y. Achdou and J. L. Guermond. Convergence analysis of a finite element projection/Lagrange–Galerkin method for the incompressible Navier–Stokes equations. *SIAM Journal on numerical analysis*, 37(3):799–826, 2000.
- [2] R. Bermejo, P. G. del Sastre, and L. Saavedra. A second order in time modified Lagrange–Galerkin finite element method for the incompressible Navier–Stokes equations. *SIAM Journal on numerical analysis*, 50(6):3084–3109, 2012.
- [3] R. Bermejo and L. Saavedra. Modified Lagrange–Galerkin methods to integrate time dependent incompressible Navier–Stokes equations. *SIAM Journal on Scientific Computing*, 37(6):B779–B803, 2015.
- [4] K. Boukir, Y. Maday, B. Métivet, and E. Razafindrakoto. A high-order characteristics/finite element method for the incompressible Navier–Stokes equations. *International Journal for Numerical Methods in Fluids*, 25(12):1421–1454, 1997.
- [5] D. Bresch and B. Desjardins. On the construction of approximate solutions for the 2d viscous shallow water model and for compressible Navier–Stokes models. *Journal de Mathématiques Pures et Appliquées*, 86:362–368, 2006.
- [6] S. A. Choudhury. Country report of Bangladesh on effective tropical cyclone warning in Bangladesh. *JMA/WMO WORKSHOP ON EFFECTIVE TROPICAL CYCLONE WARNING IN SOUTHEAST ASIA*, Tokyo:Japan, 11-14 March 2014.
- [7] P. K. Das. Prediction model for storm surges in the Bay of Bengal. *Nature*, 239:211–213, 1972.
- [8] S. K. Debsarma. Simulations of storm surges in the Bay of Bengal. *Mar Geod*, 32:178–198, 2009.
- [9] S. K. Dube, P. C. Singh, and G. D. Roy. The numerical simulation of storm surges along the Bangladesh coast. *Dynam. Atmos. Oceans*, 9:121–133, 1985.
- [10] R. A. Flather. A numerical model investigation of the storm surge of 31 January and 1 February 1953 in the North Sea. *Quart.J. R. Met. Soc.*, 110:591–612, 1984.
- [11] R. A. Flather. Estimates of extreme conditions of tide and surge using a numerical model of the northwest European continental shelf. *Estuarine Coast Shelf Science*, 24:69–93, 1987.

- [12] R. A. Flather. A storm surge prediction model for the northern Bay of Bengal with application to the cyclone disaster in April 1991. *Jr. Phys. Oceanogr.*, 24:172–190, 1994.
- [13] R. A. Flather and A. M. Davies. Note on preliminary scheme for storm surge prediction using numerical models. *Quart. J. Roy. Meteorol. Soc.*, 102:123–132, 1976.
- [14] N. S. Heaps. *Development Storm Surge Models at Bidston*. ISO Report No. 53, Institute of Oceanographic Science, Bidston Observatory, UK, 1977.
- [15] N. S. Heaps and J. E. Jones. Three-dimensional model for tides and surges with vertical eddy viscosity prescribed in two layers-II Irish Sea with bed friction layer. *Geophys. J. R. Astr. Soc.*, 64:303–320, 1981.
- [16] B. Johns and A. Ali. The numerical modeling of storm surges in the Bay of Bengal. *Quart. J. Roy. Meteor. Soc.*, 106:1–18, 1980.
- [17] B. Johns, S. K. Dube, U. C. Mohanti, and S. K. Sinha. Numerical simulation of the surge generated by the 1977 Andhra cyclone. *Quart. J. Roy. Meteor. Soc.*, 107:919–934, 1981.
- [18] B. Johns, A. D. Rao, S. K. Dube, and S. K. Sinha. Numerical modeling of tide-surges interaction in the Bay of Bengal. *Phil. Trans. R. Soc. of London*, A313:507–535, 1985.
- [19] H. Kanayama and H. Dan. A finite element scheme for two-layer viscous shallow water equations. *Japan Journal of Industrial and Applied Mathematics*, 23(2):163–191, 2006.
- [20] H. Kanayama and H. Dan. Tsunami propagation from the open sea to the coast. *Tsunami, Chapter 4, IntechOpen*, pages 61–72, 2016.
- [21] H. Kanayama and T. Ushijima. On the viscous shallow-water equations I—derivation and conservation laws. *Memoirs of Numerical Mathematics*, 8/9:39–64, 1981/1982.
- [22] H. Kanayama and T. Ushijima. On the viscous shallow-water equations II—a linearized system. *Bulletin of University of Electro-Communications*, 1(2):347–355, 1988.
- [23] H. Kanayama and T. Ushijima. On the viscous shallow-water equations III—a finite element scheme. *Bulletin of University of Electro-Communications*, 2(1):47–62, 1989.
- [24] P. Kopp. *Implementation of the Characteristic Based Split algorithm for the Shallow Water Equations in a high order finite element framework*. Bachelor’s thesis for the Bachelor of Science program Environmental Engineering, Technische Universität München, 2014.
- [25] C. Lucas. Cosine effect on shallow water equations and mathematical properties. *Quarterly of Applied Mathematics, American Mathematical Society*, 67:283–310, 2009.
- [26] J. D. Milliman. Flux and fate of fluvial sediment and water in coastal seas. *Ocean Margin Processes in Global Ghange (R. F. C. Mantoura, J. M. Martin and R. Wollast, Eds.)*, John Wiley & Sons, Ltd, Chichester, pages 69–89, 1991.

- [27] H. Notsu and M. Tabata. A single-step characteristic-curve finite element scheme of second order in time for the incompressible Navier-Stokes equations. *Journal of Scientific Computing*, 38(1):1–14, 2009.
- [28] H. Notsu and M. Tabata. Error estimates of a stabilized Lagrange-Galerkin scheme for the Navier-Stokes equations. *ESAIM: Mathematical Modelling and Numerical Analysis*, 50(2):361–380, 2016.
- [29] G. C. Paul and A. I. M. Ismail. Numerical modeling of storm surges with air bubble effects along the coast of Bangladesh. *Ocean Eng.*, 42:188–198, 2012a.
- [30] G. C. Paul and A. I. M. Ismail. Tide-surge interaction model influencing air bubble effects for the coast of Bangladesh. *J. Frankl. Inst.*, 349:2530–2546, 2012b.
- [31] G. C. Paul and A. I. M. Ismail. Contribution of offshore islands in prediction of water levels due to tide surge interaction for the coastal region of Bangladesh. *Nat. Hazards.*, 65, 2013.
- [32] G. C. Paul, A. I. M. Ismail, and M.F. Karim. Implementation of method of lines to predict water levels due to a storm along the coastal region of Bangladesh. *J. Oceanogr.*, 65:13–25, 2014.
- [33] G. C. Paul, A. I. M. Ismail, A. Rahman, M. F. Karim, and A. Hoque. Development of tide surge interaction model for the coastal region of Bangladesh. *Estuaries and Coasts*, 2016.
- [34] G. C. Paul and A. M. I. Ismail. Numerical modeling of storm surges with air bubble effects along the coast of Bangladesh. *Ocean Engineering*, 42:188–194, 2012.
- [35] G. C. Paul, M. M. Murshed, M. R. Haque, M. M. Rahman, and A. Hoque. Development of a cylindrical polar coordinates shallow water storm surge model for the coast of Bangladesh. *Journal of Coastal Conservation*, 21(6):951–966, 2017.
- [36] G. C. Paul, S. Senthilkumar, and R. Pria. An efficient approach to forecast water levels owing to the interaction of tide and surge associated with a storm along the coast of Bangladesh. *Ocean Engineering*, 148:516–529, 2018.
- [37] G. C. Paul, S. Senthilkumar, and R. Pria. Storm surge simulation along the Meghna estuarine area: an alternative approach. *Acta Oceanologica Sinica*, 37(1):40–49, 2018.
- [38] O. Pironneau. On the transport-diffusion algorithm and its applications to the Navier-Stokes equations. *Numerische Mathematik*, 38(3):309–332, 1982.
- [39] A. Priestley. Exact projections and the Lagrange-Galerkin method: a realistic alternative to quadrature. *Journal of Computational Physics*, 112(2):316–333, 1994.
- [40] M. M. Rahman, G. C. Paul, and A. Hoque. Nested numerical scheme in a polar coordinate shallow water model for the coast of Bangladesh. *J. Coast Conserv.*, 2012.
- [41] G. D. Roy. Estimation of expected maximum possible water level along the Meghna estuary using a tide and surge interaction model. *Environment International*, 21(5):671–677, 1995.

- 
- [42] G. D. Roy. Sensitivity of water level associated with tropical storm along the Meghna estuary in Bangladesh. *Environment International*, 25:109–116, 1999.
- [43] G. D. Roy. Sensitivity of water level associated with tropical storms along the Meghna estuary in Bangladesh. *Environ. Int.*, 25(1):109–116, 1999b.
- [44] G. D. Roy, A. B. Humayun Kabir, M. M. Mandal, and M. Z. Haque. Polar coordinate shallow water storm surge model for the coast of Bangladesh. *Dynam.Atmos. Oceans*, 29:397–413, 1999c.
- [45] H. Rui and M. Tabata. A mass-conservative characteristic finite element scheme for convection-diffusion problems. *Journal of Scientific Computing*, 43:416–432, 2010.
- [46] A. Saint-Venant. Theorie du mouvement non permanent des eaux, avec application aux crues des rivieres et a l'introduction de marees dans leurs lits. *Comptes-Rendus l'Académie des Sciences*, 73:147–273, 1871.
- [47] P. C. Sinha, S. K. Dube, and G. D. Roy. Polar coordinate shallow water storm surge model for the coast of Bangladesh. *J. Numer. Methods in Fluids*, 6:305–311, 1986.
- [48] E. Süli. Convergence and nonlinear stability of the Lagrange-Galerkin method for the Navier-Stokes equations. *Numerische Mathematik*, 53(4):459–483, 1988.
- [49] J. Talukder, G. D. Roy, and M. Ahmed. *Living with Cyclone: Study on Storm Surge Prediction and Disaster Preparedness*. Community Development Library, Dhaka, 1992.
- [50] Y. Tang and R. Grimshaw. Radiation boundary conditions in barotropic coastal ocean numerical models. *J. Comput. Phys.*, 123:96–110, 1996.